

Robust Inorganic Hole Transport Materials for Organic and Perovskite Solar Cells: Insights into Materials Electronic Properties and Device Performance

Azhar Fakharuddin,* Maria Vasilopoulou,* Anastasia Soultati,
Muhammad Irfan Haider, Joe Briscoe, Vasileios Fotopoulos, Diego Di Girolamo,
Dimitris Davazoglou, Alexander Chroneos, Abd. Rashid bin Mohd Yusoff,
Antonio Abate,* Lukas Schmidt-Mende, and Mohammad Khaja Nazeeruddin*

Interfaces in perovskite and organic solar cells play a central role in advancing efficiency and prolong device durability. They improve charge transport/transfer from the absorber layer to the collecting electrodes, while also blocking the opposite charge carriers, minimize voltage losses by suppressing charge recombination, and may act as buffer/protective layers and nanomorphology regulators for the absorber layer. One such interface is formed by the hole transport layer (HTL) and the organic/perovskite absorber. These HTLs typically consist of organic semiconductors, which, although are solution processable at low temperatures and allow perfect energy-level alignment with the absorber layer and therefore efficient charge collection, are prone to degradation in ambient conditions and under continuous light exposure. In a quest for robust alternatives, inorganic materials such as metal oxides, graphene oxide, bronzes, copper thiocyanate, and transition metal dichalcogenides are actively investigated. However, their hole extraction capability is inferior compared with organic semiconductors as they possess specific energetics leading to significant charge extraction barriers and moderate charge collection. To achieve further advancements in their hole transporting capabilities, strongly interconnecting knowledge of their synthesis, electronic properties, and device performance metrics is required.


1. Introduction

Solar cells which convert sunlight directly into electricity via the photovoltaic (PV) effect represent cost-effective and environmentally friendly alternatives to fast depleting fossil fuels. Among the various types of solar cells being developed, those based on Earth-abundant silicon (Si) and crystalline thin films (amorphous silicon, cadmium indium gallium selenide [CIGS], cadmium telluride (CdTe), etc.) are commercially available. These types of solar cells exhibit power conversion efficiencies (PCEs) of over 26% and an average lifetime of about 25 years.^[1–5] However, as Si or thin-film solar cells request large energy consumption for their fabrication, it was recently discussed what types of solar cells can replace them from their increasingly entrenched position.^[1] Future solar cell technologies should outperform established PVs to enter

Dr. A. Fakharuddin, Dr. L. Schmidt-Mende
Department of Physics
University of Konstanz
78457 Konstanz, Germany
E-mail: azhar-fakhar.uddin@uni-konstanz.de

Dr. M. Vasilopoulou, Dr. A. Soultati, D. Davazoglou
Institute of Nanoscience and Nanotechnology
National Center for Scientific Research “Demokritos”
15341 Agia Paraskevi, Attica, Greece
E-mail: m.vasilopoulou@inn.demokritos.gr

M. I. Haider
Department of Chemistry
Quaid-i-Azam University
Islamabad 45320, Pakistan

 The ORCID identification number(s) for the author(s) of this article can be found under <https://doi.org/10.1002/solr.202000555>.

© 2020 The Authors. Solar RRL published by Wiley-VCH GmbH. This is an open access article under the terms of the Creative Commons Attribution License, which permits use, distribution and reproduction in any medium, provided the original work is properly cited.

DOI: 10.1002/solr.202000555

M. I. Haider
Department of Chemistry
University of Wah
47040 Wah, Pakistan

Dr. J. Briscoe, V. Fotopoulos
School of Engineering and Materials Research Institute
Queen Mary University of London
Mile End Road, London E1 4NS, UK

Dr. D. Di Girolamo, Dr. A. Abate
Helmholtz-Zentrum Berlin für Materialien und Energie
Kekuléstraße 5, 12489 Berlin, Germany
E-mail: antonio.abate@helmholtz-berlin.de

Prof. A. Chroneos
Faculty of Engineering, Environment and Computing
Coventry University
Priory Street, Coventry CV1 5FB, UK

Dr. A. R. M. Yusoff
Department of Physics
Swansea University
Vivian Tower, Singleton Park, SA2 8PP Swansea, UK

the commercial market. This brings into account future generation solar cells, such as organic solar cells (OSCs), quantum dots, and perovskite solar cell (PSCs).

These future generation PVs offer a comparable PCE to Si and thin-film counterparts delivering a certified PCE of 25.2% and 17.3% for PSCs and OSCs, respectively (Figure 1). In addition, their low-temperature compatible solution processing brings in added functionalities that silicon and thin-film solar cells may not offer. For example, their manufacturing on flexible substrates enables energy harvesting from diverse areas such as automobiles, indoor electronics, lightweight portable applications, and so on. It also enables roll-to-roll processing of their large-area modules, which is compatible to massive throughputs.^[2–4] Furthermore, these future-generation solar cells, unlike silicon and thin-film inorganic counterparts, also show high performance in diffused or dim lights.^[5] Extensive research activities to improve their lifetime also demonstrated a lifetime beyond 1000 h for these solar cells, although they still require significant improvement before they enter the market.

The improvements in the performance and stability of both the PSCs and OSCs have been also due to the novel device architecture and materials. Generally, organic thin layers used to extract electrons and holes from the absorber layer despite large efficiencies achieved have led to inferior operational stability and increased device processing costs as well. As an example, 2,2',7,7'-tetrakis[*N,N*-di(4-methoxyphenyl)amino]-9,9'-spirobifluorene (Spiro-OMeTAD) and poly[bis(4-phenyl)(2,4,6-trimethylphenyl)amine] (PTAA), which are the two most successful hole transport layers (HTLs) in PSCs, are among the most expensive materials in a PSC stack.^[6–8] Robust inorganic materials such as metal oxides, copper dichalcogenides, graphene oxide, etc. have successfully replaced organic rivals and improved operational stability in both OSCs and PSCs. Another interesting aspect is the comparison of the charge extraction capabilities of organic versus inorganic transport/extraction layers and their interfaces formed with an absorber (organic materials or perovskites). These interfaces govern barrier properties such as energetics and voltage loss, transport within the device which is determined by their selectivity and conductivity, and also dictate nonradiative recombination at the heterointerfaces.^[9–21] The electronic properties of these charge transport interlayers either in the bulk or at the interface play a key role in enabling interfacial charge transport and suppressing recombination losses. However, they are generally overlooked instead of serving as guidance for the development of effective charge transport materials.

In the present Review, we discuss the recent progress made using various cost-effective and robust HTLs for OSCs and PSCs. Emphasis is given on the widely applied class of transition metal oxides (TMOs) and the recently emerged graphene oxide (GO), transition metal dichalcogenides (TMDs), and more. First, we describe the working principle of PSCs and OSCs and role of

interfacial layers in them. Then, for each class of the inorganic materials used as HTLs in the aforementioned PV devices, we provide theoretical details and factors that influence the structure and electronic properties relevant to the hole transporting functionality such as deposition methods, doping, etc., while also listing down key examples on their application in PSCs and OSCs, respectively. An improvement in the operational stability of both PSCs and OSCs due to these HTLs is subsequently detailed. Finally, we provide a detailed outlook for future research directions to improve the HTL/absorber interface to enable higher efficiencies combined with exceptional lifetimes of these types of solar cells.

2. Working Principle of Perovskite and OSCs: The Role of Interfacial Layers

2.1. Perovskite Solar Cells—Configuration and Operation

Organometallic hybrid halide perovskites are materials with a general formula of ABX₃. A range of elements can be substituted at A, B, and X sites that lead to perovskite materials with different dimensionalities at the molecular level (3D, 2D, 1D, 0D).^[22] The typical examples for A-site substitution are methylammonium (CH₃NH₃⁺, MA) and formamidinium (CH(NH₂)₂⁺, FA) or an inorganic cation such as cesium (Cs) and rubidium (Rb); for B-site occupation, a heavy metal such as lead (Pb), tin (Sn), and germanium (Ge) can generally provide stable perovskite structures while X is a halogen anion (i.e., Cl, Br, I). The initial reports on the first solid-state PSCs demonstrated a PCE between 6% and 10%,^[23–25] which was doubled within a few subsequent years only. Immense research to improve device performance by combining novel perovskite materials and their processing techniques has led to a remarkable certified PCE of 25.2%.^[26]

In a typical device architecture, a thin layer of the perovskite absorber layer (300–500 nm) is used between the electron and HTL/extraction layer (ETL/EEL and HTL/HEL, respectively), which guides photogenerated charges toward their respective electrode.^[27] A range of materials are used as ETLs and HTLs; the most commonly used are TiO₂ and spiro-OMeTAD, respectively. The unique photophysical properties and ambipolar charge transport in halide perovskites suggest that various device configurations for a PV device are possible; however, the most successful among these are planar and mesoporous PSCs.^[28,29] In planar PSCs, a compact thin ETL (HTL) in the range of several tens of nanometers (nm) is deposited on a transparent conducting oxide (TCO) substrate (such as fluorinated tin oxide, FTO, or indium tin oxide, ITO), followed by the deposition of the perovskite absorber layer, HTL (ETL), and a metal back contact (usually silver, Ag, or gold, Au).^[30–35] This thin layer can be electron or hole selective, which determines the types of PSCs to be n–i–p or p–i–n, respectively (Figure 2a,c). These

Dr. A. Abate
Department of Chemical, Materials and Production Engineering
University of Naples Federico II
Piazzale Tecchio 80, 80125 Fuorigrotta, Italy

Dr. A. Abate
State Key Laboratory of Photocatalysis on Energy and Environment
Institute of Advanced Energy Materials

Fuzhou University
Fuzhou, Fujian 350002, China

Prof. M. K. Nazeeruddin
Institute of Chemical Sciences and Engineering
École Polytechnique Fédérale de Lausanne (EPFL)
Rue de l'Industrie 17, CH-1951 Sion, Switzerland
E-mail: MdKhaja.Nazeeruddin@epfl.ch

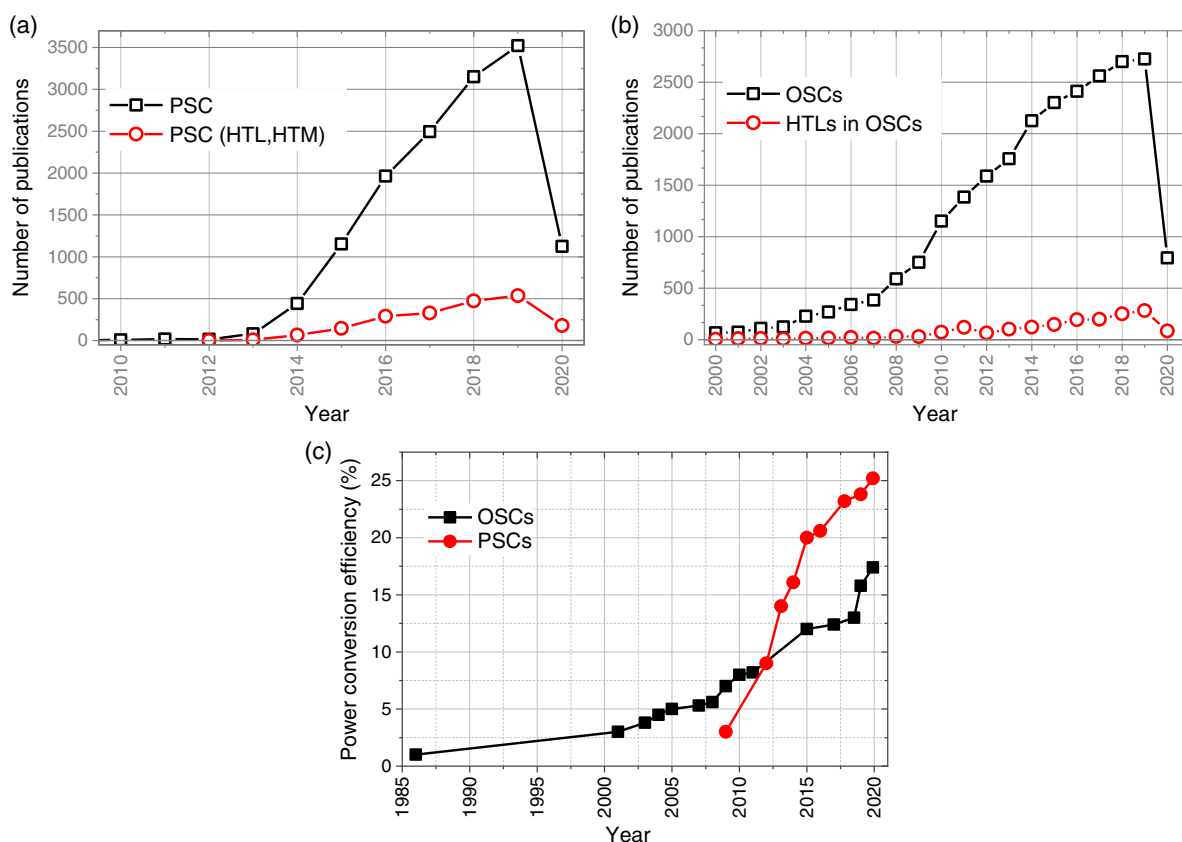


Figure 1. a,b) A trend of research publications in perovskite and OSCs and their comparison with focused articles on HTLs. The data were taken from Scopus on April 3, 2020, using keywords ‘perovskite solar cells AND HTLs/materials’ and vice versa. c) The PCE trend for both PSCs and OSCs. Both these solar cells demonstrated a rapid increase in the PCE in the last few years. The graphs are plotted from values reported in this article and based on the values reported in the National Renewable Energy Laboratory efficiency chart.^[26]

planar devices can be processed at temperatures below 150 °C and therefore are advantageous for mass production. In contrast, in a mesoporous PSC, a thicker ETL scaffold ($\approx 200\text{--}500\text{ nm}$), typically TiO_2 , is deposited on the TCO. The perovskite absorber layer infiltrates within the pores of the ETL scaffold and also forms a capping layer on top of it.^[24]

Unlike their planar counterparts, mesoporous PSCs require a high-temperature ($\approx 450\text{ °C}$) annealing process, which is regarded as a drawback for mass production.^[36] Another important device architecture, which replaces expensive metal contacts such as Au or Ag with carbon (C), is the monolithic configuration of PSCs.^[23,37,38] Such structures, even though they lag behind in efficiency compared with their mesoporous or planar counterparts, provide improved operational stability and low-cost fabrication. Another interesting aspect of perovskites is their tunable electrical properties such as carrier mobility, which can be tuned to be either n- or p-type by manipulating their defect density.^[39–41] This leads to a variation in the energy band diagrams, as shown in Figure 2d,e, which necessitates the application of charge transporting materials with tunable energetics.

The typical 3D halide perovskite, for example, MAPbI_3 or FAPbI_3 , show optimum direct bandgaps (E_g) of ≈ 1.6 and 1.5 eV , respectively.^[42–44] Theoretical calculations predicted that an optimized single-junction MAPbI_3 PSC can deliver a PCE of $\approx 31\%$.

This efficiency corresponds to a photocurrent density (J_{sc}) of 26 mA cm^{-2} , an open-circuit voltage (V_{oc}) of 1.3 V , and a fill factor (FF) of 91% .^[45] However, this requires that there are no nonradiative losses within the bulk of the perovskite as well as the device interfaces. The PSCs still have to overcome losses due to bulk and interfacial defects to reach their Shockley–Queisser limit.

The PV process in PSCs can be split into three steps, e.g., light absorption from the perovskite absorber, charge dissociation, and charge transport to respective electrodes. An optimum bandgap of the perovskite ($\approx 1.55\text{--}1.6\text{ eV}$) and a high absorption coefficient ($\approx 10^5\text{ cm}^{-1}$) ensure that maximum visible light is absorbed by the perovskite layer.^[46] A high-efficiency PSC requires negligible light absorption by the TCO and charge transport/extraction layers such that most light reaches the perovskite layer and is absorbed therein, followed by charge dissociation and separation. Herein, the low-exciton binding energy (BE) of MAPbI_3 , in the range of a few eV only,^[47] suggests that photon absorption leads to the generation of free charge carriers. This is extremely desired for a high-efficiency solar cell operation as no external force is required to separate the photogenerated electron–hole pair. The low BE and the generation of free charge carriers are among the key reasons for high-efficiency PSCs.^[48] In other excitonic solar cells, where photogenerated charge pairs (excitons) are bound with a higher BE ($300\text{--}500\text{ meV}$), losses

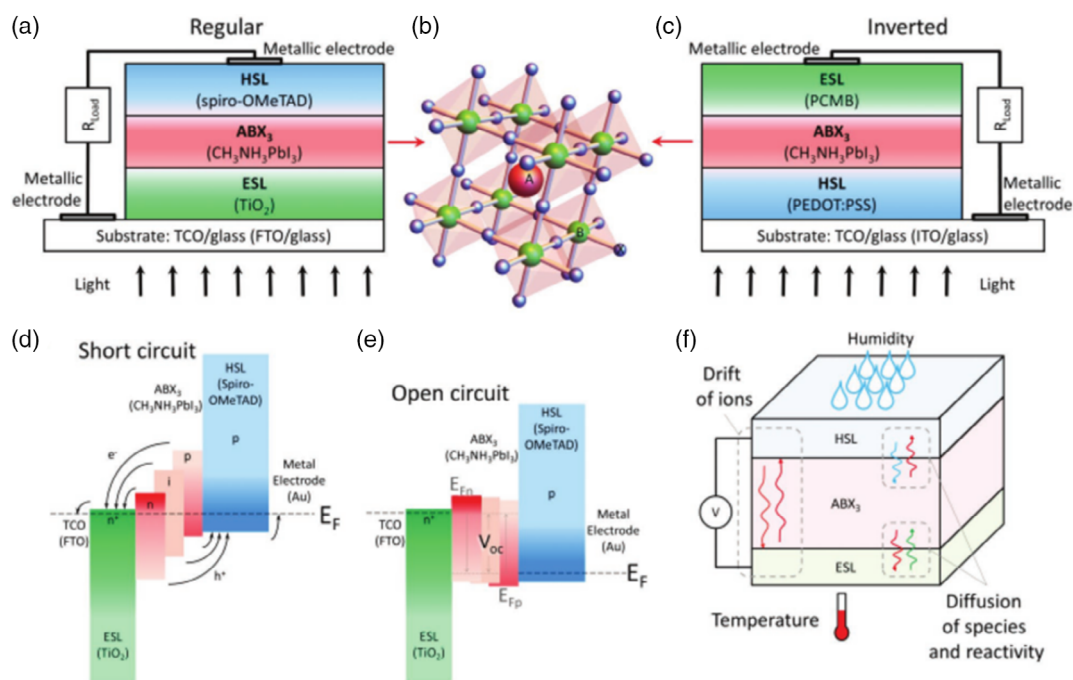


Figure 2. Typical device architecture of perovskite solar cells. a) The regular (n-i-p) PSC configuration where electrons are collected at the conducting substrate and c) an inverted (p-i-n) architecture with hole collection at the TCO. b) The crystal structure of a typical ABX_3 perovskite with a cubic phase. Schematics showing the energy levels of PSCs are d) short circuit and e) open circuit for perovskites with different conductivities. Here, E_F is the Fermi energy level at equilibrium and E_{Fn} and E_{Fp} are quasi-Fermi levels of electrons and holes, respectively. f) A PSC stack highlighting various degradation pathways within the device. Reproduced with permission.^[57] Copyright 2018, WILEY-VCH.

during exciton dissociation and migration account for significant losses.^[49]

During the process of charge separation, which starts when electrons (or holes) are injected into the neighboring ETL (HTL), an electron generated near the HTL/perovskite interface (or holes near the ETL/perovskite interface) must travel through the entire perovskite film to be collected at their respective electrode. Herein, high electron and hole mobility in the range of $1\text{--}10\text{ cm}^2\text{ V}^{-1}\text{ s}^{-1}$ and beyond,^[50–52] a large diffusion length beyond $1\text{ }\mu\text{m}$,^[53] and their ambipolar charge transport^[54,55] characteristics ensure effective charge screening and transport toward the respective electrodes. The high dielectric constant in hybrid perovskites (≈ 1000) is also beneficial as it reduces the Coulombic attraction between these electron-hole pairs and thus enables efficient charge separation.^[56]

The third step that completes the PV operation in PSCs is charge extraction toward respective electrodes. This requires the injection of at least one type of charge carrier from the perovskite absorber layer into the transport/extraction layer (and blocking of the other type). Charge-selective layers that allow only one type of charge carriers to be extracted are used alongside the perovskite layer (Figure 2a) to facilitate their extraction. It is important that these selective layers have 1) a negligible energy offset for charge extraction from the perovskite layer, 2) a high conductivity to maximize charge transport and collection efficiency, and 3) a clean electronic interface to avoid any nonradiative recombination.^[12] These selective contacts heavily influence interfacial recombination, charge accumulation, and extraction and consequently play a critical role in determining PV

parameters in PSCs.^[20] For instance, upon photon absorption, electrons are excited from the valence band (VB) to conduction band (CB), splitting the Fermi levels. This splitting can be numerically translated by the difference between the electron (E_{Fn}) and hole (E_{Fp}) quasi-Fermi levels and represents the upper limit of the achieved V_{OC} in the fabricated cell. In order for the V_{OC} to be maximized, energy losses should be minimized and selective layers play a vital role in this process. An “ideal” selective layer would enhance charge mobility and maintain the Fermi levels close to the interface without causing losses during the charge transfer (CT) process and should not induce the degradation of the absorber. A “nonideal” selective interface would result in a loss of achievable V_{OC} , i.e., a voltage lesser the Fermi-level splitting ($E_{Fn}-E_{Fp}$).^[12] For a detailed insight into the working principle of PSCs and their unique photophysical properties, we refer to some focused articles.^[57–60]

2.2. OSCs–Working Principle and Common Device Architectures

The PV process in OSCs differs from that in perovskite and inorganic counterparts. In the latter, the absorption of photons with energies above the optical bandgap results in the generation of free carriers (electrons and holes) that diffuse through the corresponding bands, i.e. conduction and VB, under the application of an external electric field, and are collected at the respective electrodes. Organic semiconductors, however, exhibit much lower dielectric constants (around 3.5) than the perovskites

and inorganic counterparts (reaching 1000), which leads to a stronger Coulombic interaction between electrons and holes. Light absorption thus generates Coulombically bound electron/hole pairs, the so-called Frenkel excitons, rather than free charge carriers.^[49,61] In order for these excitons to dissociate into free carriers, the presence of a driving force provided by a two-component system containing an electron donor (D) and an electron acceptor (A) that is similar to that of a p–n junction is necessary (Figure 3a).^[62,63] Upon photon absorption usually by the donor, an exciton is formed through excitation of an electron from its highest occupied molecular orbital (HOMO) to the lowest unoccupied molecular orbital (LUMO) (Figure 3b). This exciton then diffuses towards the donor:acceptor interface, where it dissociates into a hole and an electron when

$$E_A^A - E_A^D > U_D \quad (1)$$

where E_A^A and E_A^D are the acceptor and donor electron affinity, respectively, and U_D is the BE of the exciton. The electron is then transferred to the LUMO of the acceptor and forms a CT complex (Figure 3b).

The electron/hole pair that forms the CT state can also be referred to as the geminate pair and is highly dependent on the Coulombic attraction between opposite carriers and on the distance that separates these species.^[18] If the latter becomes larger than the Coulomb capture radius, the geminate pair dissociates into free carriers; otherwise, the geminate pair will recombine across the donor:acceptor interface, the so-called geminate recombination, which constitutes a common loss mechanism in OSCs.^[64,65] The dissociated electrons and holes can then be transported through the acceptor and donor domains, respectively, to the respective electrodes, with electrons being collected at the cathode and holes at the anode.

In the most efficient OSC architecture, the so-called BHJ (Figure 3a), an interpenetrating network of donor and acceptor domains, forms the photoactive layer that assures a balance between light absorption and exciton dissociation efficiencies. Key objectives in OSCs are the minimization of energy and charge losses both upon exciton dissociation and through transport within the BHJ device (the latter is crucial due to the low carrier mobility and low diffusion length of the order of 10 nm in organic semiconductors)^[66] to enhance the efficiency of devices. For a more detailed explanation of these complex processes, the reader is referred to excellent reviews already published.^[64,67–69]

A challenging step that contributes to efficient OSC operation is charge transport and collection at the electrodes. As most photoactive materials exhibit large energetic differences of their molecular levels, i.e., the HOMO of the donor and the LUMO of the acceptor with the work function (W_F) values of the corresponding electrodes, a typical OSC device configuration, fabricated on a transparent rigid (e.g., glass) or flexible substrate, usually comprise a HTL/HEL and an ETL/EEL, which are all sandwiched between a high- W_F anode (the hole-selective contact) and a low- W_F cathode (the electron-selective contact). The interfacial properties of charge transport/extraction materials can strongly influence the device performance. The main requirement that needs to be satisfied for highly efficient interfacial CT to occur is the energetic alignment of the HOMO and LUMO of the photoactive layer with both the respective ones of the HTL and ETL and the Fermi level (i.e., the W_F) of the electrodes. An energetic mismatch at any device interface may lead to barriers for charge extraction, high contact resistance, space charge formation, and undesirable recombination; all these factors decrease device performance.^[70] Other issues that may influence charge transport/extraction, even when interfacial energetic

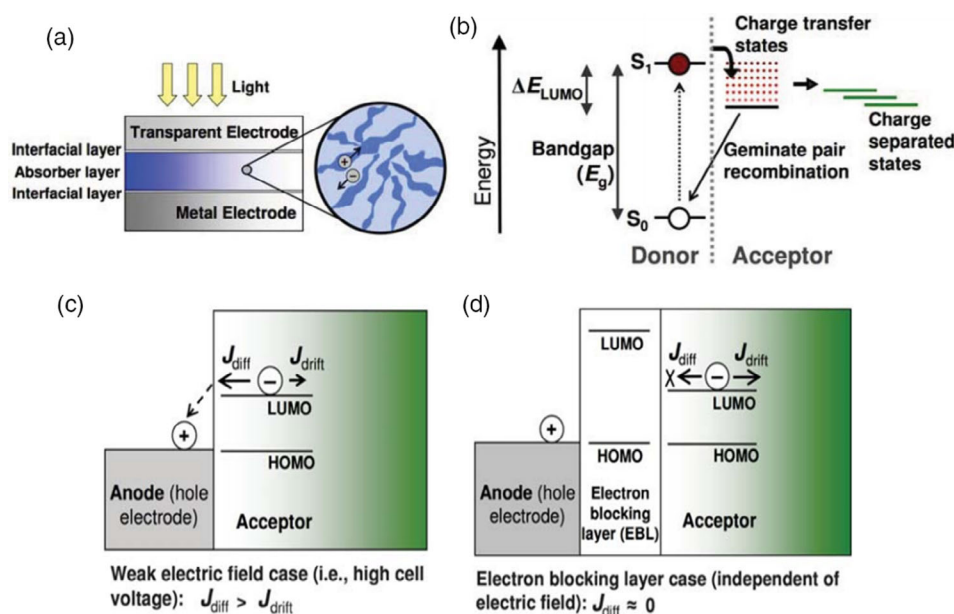


Figure 3. a) Schematic representation of the mixed donor:acceptor (the so-called bulk heterojunction, BHJ) OSC. b) The energy-level diagram in a representative OSC structure depicting the HOMO (S_0) and LUMO (S_1) levels of the donor and the formation of CT states between the donor and acceptor. The process of geminate recombination is also illustrated. Illustration of electron leakage toward the anode (the hole-selective contact) in c) the absence and d) presence of an appropriate EBL. Reproduced with permission.^[49] Copyright 2011, the Royal Society of Chemistry.

alignment is excellent, are the presence of interface defect states and poor interfacial compatibility/morphology.^[56] To address these issues, several strategies have been explored. In particular, to ameliorate stringent CT/extraction requirements, a common approach involves inserting varying functionality interlayers at the electrode/organic interface with desirable electronic characteristics to act as an energy gradient (by providing a lower energy step) and, thus, mediate CT/extraction.

2.3. The Role of the HTL

The HTL serves as the medium that enables efficient extraction of photogenerated holes from the absorber. Therefore, it plays a key role in enhancing the device efficiency and stability in both the regular and inverted architectures. A higher efficiency can be achieved due to its role in allowing fast hole transport toward the hole-selective contact (termed the anode in OSCs and as the cathode in PSCs), improving the selectivity of the corresponding interface, suppressing carrier recombination, and blocking electron transfer toward the respective contact. HTLs deposited prior to the photoactive layer deposition (in regular OSCs and inverted PSCs) are also important in modifying the morphology/crystallization of the organic/perovskite underlayer that significantly influences the device efficiency and stability. There are two large categories of materials serving as HTLs in OSCs/PSCs, namely organic and inorganic compounds.^[71,72] The organic ones possess the advantage of the simple manipulation of their chemical/electronic structure and facile solution processing. The inorganic ones are more robust, hence also acting as buffers to protect the device from degradation.

The HTL is also vital for device stability because it can protect the underlying absorber (in inverted OSCs and regular PSCs) from degradation caused by the penetration of moisture/oxygen through the electrode or the HTL itself.^[8,73,74] As inferior stability represents a major bottleneck toward the commercialization of these devices, especially of those based on perovskite absorbers, the development of robust HTLs could offer the opportunity to resolve this issue. Furthermore, a high efficiency can be achieved due to its role in improving interfacial transport, suppressing charge recombination, and blocking electron transfer toward the hole-selective contact (Figure 3c,d). The surface energy of the HTL is also of paramount importance because it largely influences the morphology/crystallinity of the organic or perovskite absorber when grown above it. However, the basic requirement is the favorable energy-level alignment at the interface. In particular, the HOMO or valence band maximum (VBM) of the HTL should be aligned with or slightly higher than the HOMO of the donor material in OSCs or the VBM of the perovskite in PSCs. Such requirement allows for efficient hole extraction with minimal voltage loss, leading to improved open-circuit voltage (V_{OC}). Moreover, the LUMO or conduction band minimum (CBM) of the HTL should be considerably higher than the corresponding energy levels of the photoactive absorber (i.e., the LUMO of the donor in the BHJ architecture or the CBM of the perovskite) to act as an electron blocking layer (EBL), hence preventing electron leakage toward the hole-selective contact. Therefore, the electronic structure of the material is of paramount importance when designing novel HTLs. Additional merits are good solubility,

high environmental and thermal stability, and hydrophobic nature. They should also provide the advantage of simple preparation and manipulation of their properties.

3. Transition Metal Oxides: Theoretical Investigations of Electronic Properties and Influence Of Processing Methods and Doping in their Charge Transport Properties

TMOs have demonstrated adjustable structural, electronic, and optical properties, which are highly desirable for their application as HTLs in diverse PV architectures. They also exhibit highly attractive features, such as high transparency and nanometer-scale controllable film morphology with excellent reproducibility. Their stoichiometry can be adjusted from fully stoichiometric (i.e., molybdenum trioxide, MoO_3) to semimetallic (like MoO_2) with a bandgap energy ranging from about 3.5 to below 2.7 eV. Oxygen vacancies are critical on the surface of the electronic structure, especially in α -phase MoO_3 , and thus their control is pivotal to alter the conductivity and chemical stability of TMOs.^[75] Apart from the oxygen vacancies, other factors that affect their conductivity are doping, film thickness, grain size, and thermal treatment.^[75] The electronic structure of TMOs should be well known when designing OSCs/PSCs with them as the HTL as it defines the energetic alignment at the hole extracting interface. We hence include in this Review theoretical calculations of the most studied TMOs regarding their crystal structure and electronic properties and dependence on processing methods and doping.

3.1. Molybdenum Oxides (MoO_x)

Molybdenum oxides have been successfully applied as HTLs in OSCs and PSCs due to their desired optical and electronic properties such as a high W_F above 6.0 eV, optical transparency, and adequate conductivity, especially in under-stoichiometric phases. Regarding their structural properties, stoichiometric molybdenum trioxide (MoO_3) is generally found in two phases, the orthorhombic α -phase ($a = 3.96 \text{ \AA}$, $b = 13.85 \text{ \AA}$, $c = 3.69 \text{ \AA}$), which exhibits a 2D structure,^[76] and the monoclinic β -phase with a 3D crystal structure.^[77] β -phase can be converted to the α -phase upon thermal treatment ($T > 350^\circ\text{C}$). Figure 4a shows the X-ray diffraction (XRD) patterns of electrodeposited MoO_3 films on FTO, showing the evolution from quasiamorphous to crystalline thin films, having both α - and β - MoO_3 phases upon annealing at 300°C . Other crystal structures include ϵ - MoO_3 , a metastable high-pressure phase, and the hexagonal h - MoO_3 structure, with the latter octahedral phase illustrating similar properties with α -phase.

In the 2D α -phase, the Mo–Mo and O–O distances between interlayers are ≈ 7 and 0.79 \AA , respectively (Figure 4b). Regarding the electronic structure of MoO_3 , the upper states of the VB mainly consist of O 2p orbitals, whereas the bottom of the CB shows contribution mainly from Mo 4d atomic orbitals. In Figure 4c, the arrow indicates the indirect bandgap between the VBM and CBM from U to Γ symmetry points. The nonstoichiometric oxides present both Mo and O vacancies (termed V_{Mo} and V_{O} , respectively) that create gap states (see density of states

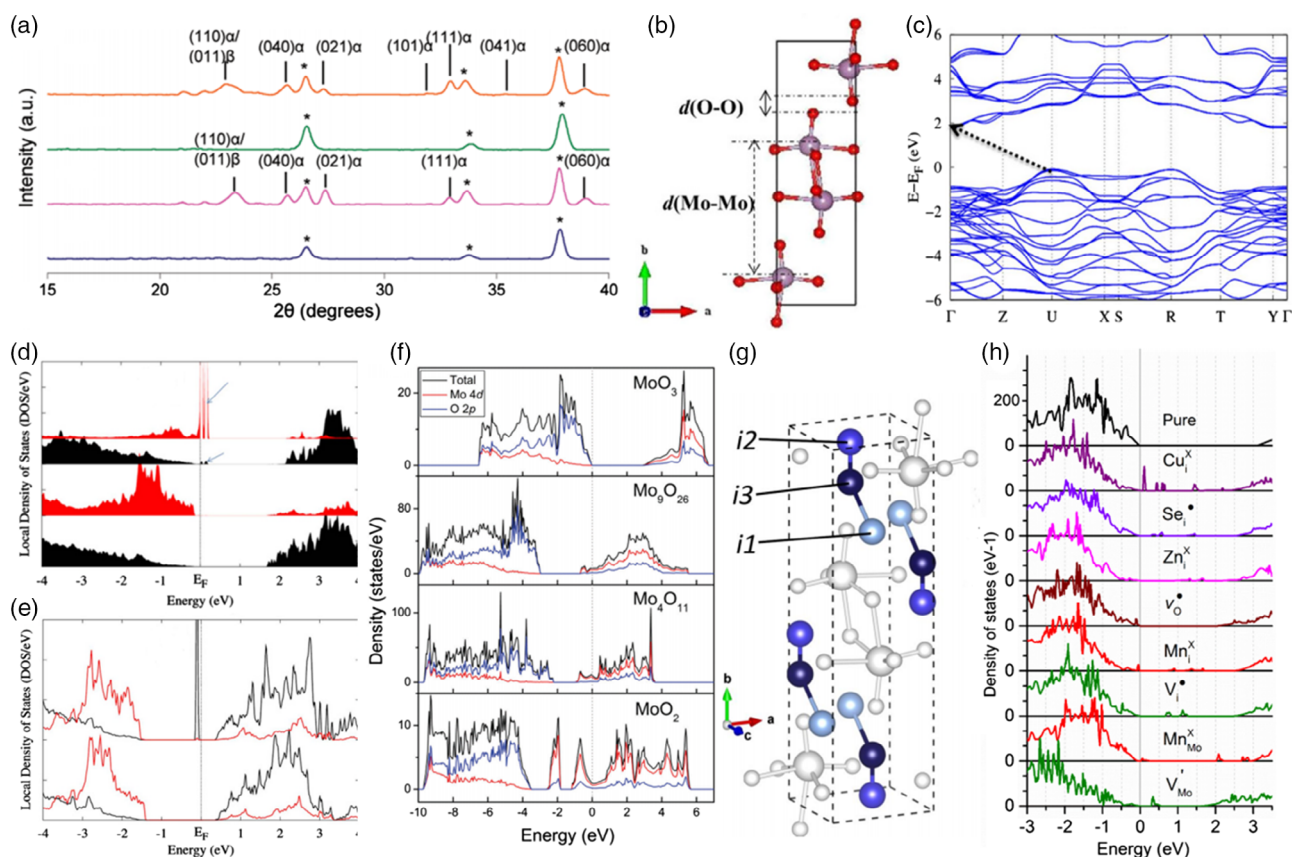


Figure 4. a) The XRD patterns of MoO₃ films electrodeposited on FTO, from top to bottom: annealed at 300 °C for 2 h, as deposited; asterisk denotes FTO peaks. Reproduced with permission.^[77] Copyright 2012, American Chemical Society. b) Unit cell of the MoO₃ structure and c) MoO₃ band structure diagram with the black arrow indicating the indirect bandgap from U to Γ symmetry points. d) MoO₃ DOS diagram with a Mo vacancy. The arrows indicate the defect-induced gap states. e) V_O (oxygen vacancy), with red and black lines corresponding to the Mo and O DOS, respectively, including the defect-induced gap states. Reproduced with permission.^[76] Copyright 2016, Springer Nature. f) Total, Mo 4d and O 2p orbital DOS of MoO₃ and under-stoichiometric MoO_x phases. Reproduced with permission.^[79] Copyright 2017, American Chemical Society. g) MoO₃ unit cell illustration including the stable interstitial sites (i1, i2, i3). h) The DOS of MoO₃ (pristine) and after including different dopants (along with O and Mo vacancies). Reproduced with permission.^[81] Copyright 2018, American Chemical Society.

[DOS] charts in Figure 4d,e). V_{Mo} induces states being closer to the VB and that can be attributed to oxygen atoms being unsaturated. However, V_O leaves behind immobilized Mo due to the dangling bond and induces d states that are closer to the CB. This indicates unintentional p-type and n-type doping of this oxide in the first and latter case, respectively. V_O is energetically more favored than V_{Mo}, which leads to commonly used MoO_x n-type semiconductors.^[78]

The MoO₃ structure consists of six oxygen atoms surrounding octahedrally the Mo atom.^[78] Inzani et al.^[79] demonstrated that oxygen vacancies affect the lattice parameters of the MoO₃ structure (Figure 4f). In particular, O₁ and O₂ vacancies have only a minor impact on *a* and *c* parameters, with the *b* parameter remaining unchanged. The formation of O₃ vacancies, however, results in a large increase in the *b* parameter and a decrease in *a* and *c* parameters. These changes significantly affect the electronic properties of Mo oxides and consequently, their functionalities as hole transport materials (HTMs) in both OSCs and PSCs.

Besides oxygen vacancies, the structure and electronic properties of these oxides can be effectively controlled through doping

in either interstitial or substitutional sites with several elements. Density functional theory (DFT) calculations have predicted that three sites are stable for substitutional doping, as shown in Figure 4g, with i1 and i3 interstitial sites being the most preferable for different ions including sodium (Na), potassium (K) (also preferring i2, i3 sites),^[80] indium (In), manganese (Mn), and gallium (Ga) (also preferring i2 sites).^[81] A bandgap reduction is observed in all cases due to the creation of intergap states (Figure 4h), which are generally closer to the CBM, except for doping with copper (Cu), which serves as a p-type interstitial dopant, hence inducing gap states near the VBM.

A good match between the theoretical and experimental bandgap of MoO₃ has been reported, with the theoretical bandgap being around 2.8 eV, closely matching the experimental range (2.7–3.4 eV).^[82] As O concentration is decreased, the bandgap is narrowed due to the filled 4d states of Mo, with the Fermi level being inside the CB in nonstoichiometric Mo oxides that are generally of n-type character. The indirect bandgap of the stoichiometric MoO₃ ranges between 2.7 and 3.2 eV, with an electron affinity at around 6 eV, ionization energy

at around 9 eV, and a W_F higher than 6.9 eV.^[75] This high- W_F value constitutes MoO_3 as the selection material for engineering the hole-selective interface of several types of PV devices as it induces the formation of large positive interfacial dipoles, hence significantly strengthening the device's built-in field that accelerates hole transport.

3.2. Tungsten Oxides (WO_x)

Tungsten trioxide (WO_3) has also been frequently applied as HTL in OSCs and PSCs. It is considered a wide-bandgap semiconductor, with O 2p and W 5d contributions in the VBM and CBM, respectively, the difference of which corresponds to the band gap value E_g .

WO_3 can be found in monoclinic phases ($\epsilon\text{-WO}_3$, $\gamma\text{-WO}_3$), orthorhombic β -phase, tetragonal α -phase, and cubic phase.^[83,84] The transition to different phases is achieved mainly through annealing and cooling processes (Figure 5a), with stable γ -phase occurring mostly at room temperature and either β -phase or α -phase occurring at high annealing temperatures. At very low temperatures, the ϵ -phase is stabilized. The WO_3 structure is composed of several perovskite structures (Figure 5b), which explain its nonstoichiometric properties. Like in MoO_x , electric conductivity of WO_3 depends on several factors like film thickness, presence of defects such as V_O , grain size and boundary, and synthesis method, and it can be also increased by the introduction of different dopants.^[83,85]

The most recent theoretical studies consider WO_3 as the perfect cubic despite the distortion in the crystal structure that has been attributed to the rotation of WO_6 octahedra and differences in the lengths and angles of the W–O and W–O–W bonds, respectively.^[84,86] Both phases of WO_3 (hexagonal and cubic, Figure 5c) have demonstrated similar characteristics, including similar theoretical bandgaps, e.g., 0.4 and 0.5 eV for the cubic and hexagonal, respectively. Notably, both showed high deviation from the experimental values ($\approx 2.5\text{--}3.0$ eV). Also, hexagonal and cubic WO_3 have shown similar formation and ground-state energies, with the hexagonal tungsten phase illustrating high stability in temperatures up to 500 °C and the cubic tungsten phase being the most preferred and most commonly occurred.^[84]

Similar to MoO_3 , WO_3 is a high- W_F semiconductor ($W_F > 6.0$ eV), which renders it appropriate for hole extraction, as it is expected to form large positive interfacial dipoles with the commonly used ITO hole-selective contact material ($W_F \approx 4.7$ eV). However, the low conductivity of the stoichiometric phase necessitates the use of relatively thin interlayers.

3.3. Copper Oxides (CuO_x)

Copper oxides show intrinsic p-type semiconducting behavior and attractive physical and chemical properties along with superconductivity at a relatively high temperature, a phenomenon not yet fully understood.

Cupric oxide (CuO) has been investigated for a range of applications, such as electrode material in diverse types of optoelectronics such as solar cells, batteries, and gas and infrared radiation sensors. It has a monoclinic structure, bandgap between 1.2 and 2.1 eV depending on its nature (direct or

indirect) and thickness of the CuO layer, and Bohr's radius of 6.6 nm. It shows a strong quantum confinement effect below that thickness range.^[87,88] Its electron configuration has an open 3d cell ($3d^9$), which is considered to significantly affect the ionization states and its band structure. While cuprous oxide (Cu_2O) has a cubic structure, CuO is monoclinic with lattice *a*, *b*, and *c* parameters approximately equal to 4.68, 3.42, and 5.13 Å, respectively, with each atom neighboring four atoms of the other kind (Figure 5d).^[89]

Due to their intrinsic p-type conductivity, copper oxides have been also applied as HTLs underneath the photoactive layer in regular OSCs and inverted PSCs. They are generally processed using the solution deposition method followed by appropriate thermal annealing.

3.4. Nickel Oxides (NiO_x)

Nickel oxides (NiO_x) are the most widely studied metal oxides for use as HTLs in PSCs with the inverted architecture. NiO , unlike CuO , adopts the NaCl rock salt structure (Figure 5e) and is commonly nonstoichiometric.^[90] In its stoichiometric form, it is an insulator.^[91] Due to its high specific capacitance (theoretically around 2584 F g^{-1}), resistivity of around $10^{13} \Omega \text{ cm}$ (at room temperature), and its multiple oxidation state favoring redox reactions, it has been used for a broad range of applications including supercapacitors, electrochromic devices, chemical sensors, micro- and normal batteries, photocatalysis, and smart windows.^[92–94] It has a melting temperature of 1995 °C and a density of around 6.7 g cm^{-3} . Like CuO , it shows p-type semiconducting behavior; however, it has a significantly wider bandgap ranging between 3.6 and 4 eV. The most widely used manufacturing method for NiO involves the thermal sol-gel decomposition of nickel hydroxide, with thermal evaporation being the most commonly used deposition method.^[81,95,96] Other successful deposition methods include pulsed laser deposition and solution-processed NiO .^[97,98]

The thermodynamically most abundant defect is the nickel vacancy (V_{Ni}),^[99,100] whose twofold negative charge is compensated by the stabilization within the lattice of Ni^{3+} cations, resulting in p-type self-doping.^[101] Due to this, $\text{Ni}_{1-\delta}$ (or NiO_x as generally referred to in the perovskite PV field) optoelectronic properties depend on the oxidation state of the film, which can be controlled by processing conditions.^[102] Therefore, the bandgap of NiO might vary between 3.4 and 4.0 eV,^[103] with the VB lying between -5.0 and -5.4 eV.^[104] This makes NiO attractive for perovskite PVs, due to good energy-level alignment with the VB of the most common perovskite composition (such as methyl ammonium iodide, MAPbI_3 , or triple-cation perovskites). Further, the wide bandgap assures high transparency and promotes selectivity in charge extraction (or “EBL”).

The spin coating of a precursor solution followed by an annealing step at about 300 °C is the standard deposition route for NiO hole-selective layers in p–i–n perovskite solar cells.^[105,106] Combustion chemistry principles allow a reduction of the annealing temperature.^[107] Herein, an additive couple is selected to initiate a combustion (exothermic) reaction, which provides the energy required for the crystallization of NiO , allowing to reduce the annealing temperature at 250 °C and still achieving

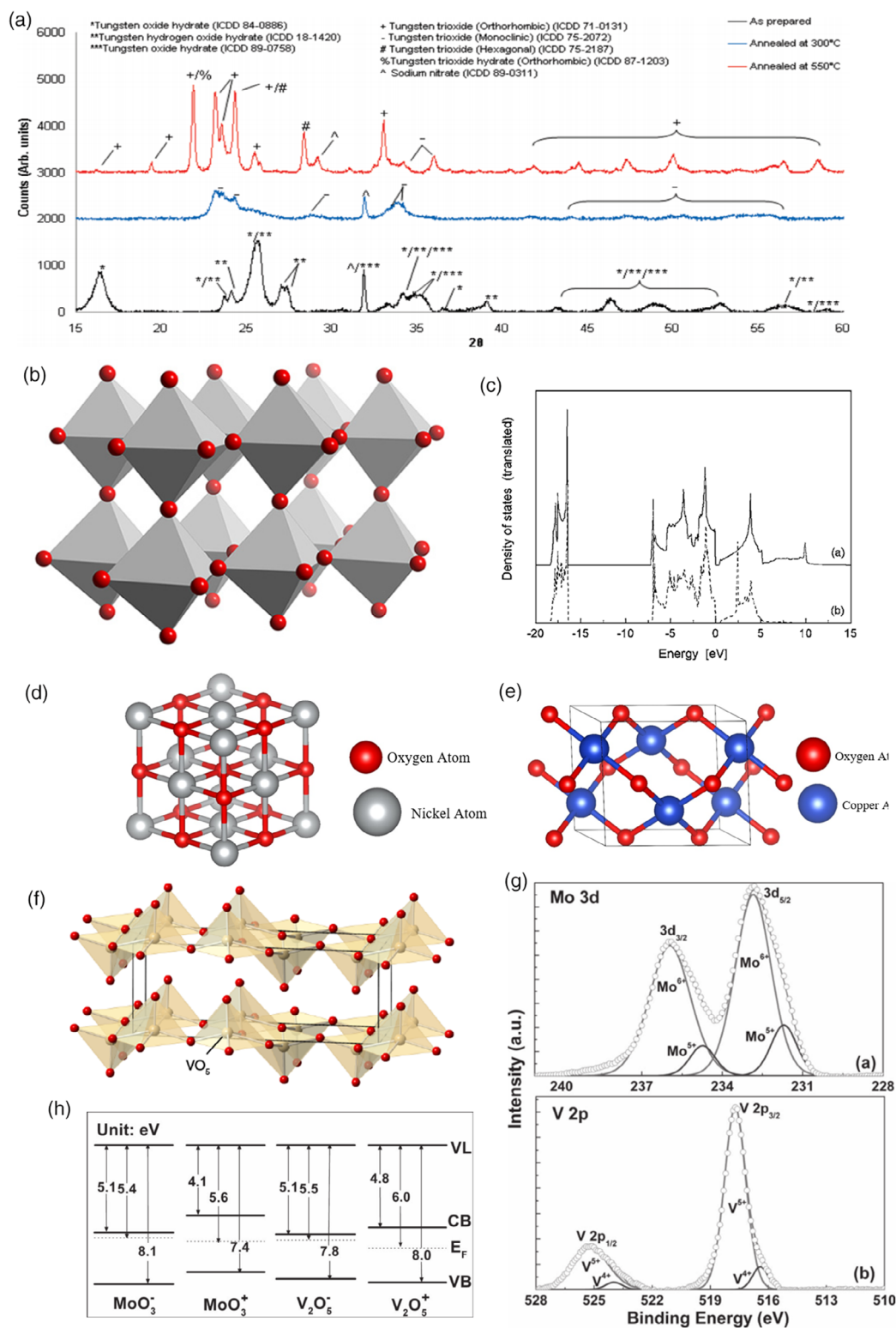


Figure 5. a) XRD patterns of tungsten oxide at different stages of fabrication.^[366] Copyright 2009, American Chemical Society. b,f) illustrations of the crystal structure of WO₃ and V₂O₅, respectively. Adapted from ChemTube3D (<https://www.chemtube3d.com/>). c) DOS of cubic (top) and hexagonal (bottom) WO₃. Reproduced with permission.^[160] Copyright 2005, American Physical Society. Crystal structure of d) Cu₂O and e) NiO. g) XPS spectra of the Mo 3d core level in MoO₃ (top) and V 2p core level in V₂O₅ (bottom). The circles show the experimental XPS data and the solid lines show the fits. h) Band diagrams MoO₃ and V₂O₅ with oxygen vacancies (-) and excess oxygen (+). VL, EF, CB, and VB represent vacuum level, Fermi level, CB, and VB, respectively. Reproduced with permission.^[161] Copyright 2013, WILEY-VCH.

20% efficient p–i–n PSCs.^[108] However, to adopt plastic substrates (e.g., polyethylene terephthalate, PET) for flexible PVs, the processing temperature must be substantially lower than 250 °C. In this case, NiO thin films can be deposited from inks of NiO nanoparticles (NPs).^[109,110] The advantage is that NiO is already crystalline, and the annealing step is replaced by a drying step at temperatures within 100 °C. NiO NPs are obtained from the annealing of Ni(OH)₂ precipitated from aqueous solution. It has been proposed that the crystalline NP dispersion stability is guaranteed by an amorphous coexisting phase,^[111] whose impact in hole extraction, recombination, and stability might deserve further investigation, especially considering that this route is widely adopted to fabricate devices with PCEs approaching 20%.^[112] Notably, the NP route might enable effective adoption of NiO in the n–i–p architecture,^[113] especially if the NPs are functionalized to be dispersed in perovskite-compatible solvents.^[114,115] Electrodeposition,^[116,117] chemical bath deposition,^[118] and spray coating^[119] are alternative solution-based techniques demonstrated, suitable to obtaining good performing NiO. High-performing devices have been demonstrated, also using NiO from physical methods: pulsed laser deposition,^[120] e-beam deposition,^[121] glancing angle deposition,^[122] atomic layer deposition (ALD),^[123,124] sputtering,^[125,126] or even the evaporation of metallic nickel followed by oxidation in air at high temperatures.^[127]

The high conductivity of selective contacts is fundamental to minimize the resistive losses detrimental to the energy output of PV devices. One of the first parameters investigated in detail was the effect of “oxygen doping” on NiO, which can be exploited via UV–ozone or O₂–plasma as postsynthesis treatments^[128] or by tuning the O₂ partial pressure during synthesis, such as in the case of physical deposition techniques like sputtering.^[129] The oxidation of NiO yields a more conductive material and deepens the W_F ,^[130] improving the energy match between the NiO and perovskite VB. However, optical losses accompany the improved electrical properties, and concerns about the stability of the NiO oxidized state should be addressed. It has been proved that semiconducting metal oxides can exchange oxygen^[131] or hydrogen^[132] with the perovskite, and oxidized NiO phases tend to be unstable,^[133] which might be an interesting research topic to improve our understanding on the effect of selective contacts on the stability of PSCs.

Conventional doping through the alloying of Ni with foreign cations appears as a more robust strategy. Copper doping of NiO has been a successful strategy, first demonstrated in 2014.^[134] The conductivity of NiO increased from $2.2 \times 10^{-6} \text{ S cm}^{-1}$ to $8.4 \times 10^{-4} \text{ S cm}^{-1}$ when introducing 5% of Cu²⁺. The same group later also demonstrated a low-temperature process by exploiting the nitrate-acetylacetonate combustion route and deposited an efficient Cu:NiO at 150 °C.^[135] Copper doping was later implemented in NiO NPs, which led to the best-performing NiO-based mesoscopic PSC to date (with efficiency approaching 20%).^[136] The doping mechanism is not trivial. In fact, the stable oxidation state of copper is Cu²⁺, the same for nickel. Due to the observation of lattice shrinkage upon doping despite the large ionic size of copper than nickel, Kim et al., proposed that the substitutional replacement of Ni²⁺ with Cu²⁺ leads to an increase in the concentration of V_{Ni} .^[134] Chen et al., through X-ray photoelectron spectroscopy (XPS), observed

the copresence of Cu²⁺ and Cu⁺, with the latter acting as the effective p-type dopant.^[137]

Several other transition metal cations have been introduced as p-type dopants in NiO such as Ag,^[138] Co,^[139] Y,^[140] and Zn.^[141] Cobalt (Co)-doped NiO was first demonstrated by Huang et al., with a co-sputtering deposition route.^[142] The conductivity increased upon Co doping, whereas the W_F was slightly reduced. Interestingly, the change of the W_F in the opposite direction was observed later by Kaneko et al.^[143] (using Co-doped NiO NPs) and by Xie et al.^[144] (using a solution-processed NiO), still obtaining an increase in conductivity. A reason behind this opposite behavior might be the different cobalt oxidation state obtained from the high-vacuum cosputtering route, where only a single XPS peak for the Co 2p_{3/2} peak is obtained, compared with solution-processed Co:NiO, where Co 2p_{3/2} is more complicated, pointing to the coexistence of 2+ and 3+ oxidation states, as reported by Lee et al.^[139] Hou et al. explored a regime beyond the doping, investigating a mixed Ni–Co (1:1) oxide.^[145] Here, the coexistence of Co²⁺ and Co³⁺ in the mixed oxide (similarly to CoO_x) is evident and the work function is increased as in the works from Kaneko et al.^[146] and Xie et al.^[147] Along with Co³⁺, Fe³⁺ has been reported to enhance the hole concentration (by a factor of 1.5) and hole mobility (by a factor of 2.5) of NiO NPs.^[148]

The case of zinc (Zn) is of particular interest, as this cation assumes only the 2+ oxidation state, the same of Ni²⁺. Nonetheless, its doping into NiO enhances the conductivity and the PV performances of p–i–n PSCs, as demonstrated by Wan et al.^[141] DFT calculations showed that the DOS around the Fermi level increases when Zn²⁺ replaces Ni²⁺ in the NiO lattice along with a substantial reduction of the V_{Ni} formation energy. Zn²⁺ is not the only isovalent dopant effective in NiO. In fact, Ge et al., systematically investigated the effect of alkaline cation doping of NiO.^[149] The main effect found was a downward shift of the VBM going from –5.04 eV for the pristine NiO to –5.19 eV with magnesium (Mg) and –5.29 eV with calcium (Ca) and –5.34 eV with strontium (Sr) (and barium, Ba, leading to –5.18 eV), with all the cations apparently substituting Ni, as suggested by the lattice expansion from XRD. At the same time, the conductivity was increased due to enhanced hole mobility. Another successful dopant is Mg²⁺, which demonstrated that the downward shift of the VBM is proportional to Mg concentration, introduced via a cosputtering route.^[150]

The Mg-induced downshift of NiO VBM was exploited by Chen et al.,^[151] in their seminal paper on lithium and magnesium codoped NiO, where the synergy between the enhancement of conductivity due to p-doping of lithium and tuning of energy level from Mg was achieved. Li⁺ has a different valence and a similar ionic radius with respect to Ni²⁺, two features easily allowing p-doping through substitutional replacement.^[152]

In fact, different groups reported a positive impact of NiO lithium doping on PSC performances, due to a substantial increase in the conductivity of NiO.^[153,154] Moreover, codoping strategies including lithium and transition metal cations were demonstrated, such as lithium:silver (Li:Ag)^[146] and Li:Co.^[147] Interestingly, positive effects on NiO HTL properties have been demonstrated by alloying also the larger alkaline cations, for which the substitutional replacement of Ni²⁺ should be energetically hindered. Indeed, Na⁺ has been shown to passivate NiO defectivity rather than increasing the conductivity,^[155] whereas

potassium (K^+) doping combines the two positive effects.^[156] An increase in conductivity has been observed also from rubidium (Rb^+)^[157] and Cs^+ doping.^[158,159] Cesium, moreover, has been reported to suppress the eventual formation of metallic Ni during the processing of NiO .^[158]

3.5. Hydrogen Molybdenum and Vanadium Bronzes

The stoichiometric composition of TMOs is a crucial consideration for synthesized HTMs.^[160] For instance, vanadium oxides may be found in the form of V_2O_3 and V_2O_5 (Figure 5f), which also present intrinsic n-type conductivity (similar to MoO_x and WO_x) due to oxygen vacancies and high- W_F values.

Besides oxygen content, the presence of hydrogen (H) or other elements within the TMO structure has a significant influence on their electrical properties (i.e., band structure). Xie et al.^[161] prepared solution-processed hydrogen Mo and V bronzes for application as HTLs in OSCs. To successfully obtain hydrogen bronzes, ethanol was used to control the reaction between metal oxide NPs and hydrogen peroxide. XPS regarding Mo 3d in molybdenum and V 2p in vanadium bronzes (Figure 5g) revealed that the Mo 3d spectrum could be well fitted by two separated doublets in the form of a Gaussian function, indicating molybdenum species present in two different oxidation states. The major contribution was from the peaks centered at BEs of 232.8 and 236.0 eV. These are the typical doublets for Mo 3d in the oxidation state 6+. The minor peaks were the doublets at 231.7 and 234.7 eV attributed to Mo 3d in the oxidation state 5+. The atomic concentration ratio of Mo^{6+} to Mo^{5+} was 6:1 and that between Mo and O was about 1:2.93, indicating a small degree of oxygen deficiency.

Similar results were obtained for vanadium bronzes prepared in the same work.^[161] The XPS spectrum of vanadium bronze consisted of two Gaussian-like 2p doublets, which were indicative of V^{5+} and V^{4+} oxidation states. V^{4+} accounted only for 8% of total vanadium atoms. The atomic ratio between V and O was found equal to 1:2.46, also indicative of a small degree of oxygen deficiency in that case. The oxygen deficiency (the presence of oxygen vacancies) was attributed to the insertion of a small amount of H^+ into the structure of the oxides, which hence were treated as bronzes (H_xMoO_3 and $H_xV_2O_5$, respectively). The electronic band structure of these bronzes was evaluated using ultraviolet photoelectron spectroscopy (UPS). From the secondary electron cut-off of these spectra, the W_F values for ITO, H_xMoO_3 , and $H_xV_2O_5$ were found as 4.6, 5.4, and 5.5 eV, respectively. From the band diagram (Figure 5h), it is observed that H_xMoO_3 and $H_xV_2O_5$ films exhibit very low-lying CBMs and n-type characteristics, which are typical for molybdenum and vanadium oxides. These characteristics could be very beneficial for their application as HTLs in OSCs, where hole transport through n-type metal oxides has been considered to be realized by extracting electrons through their CBs.

4. Applications of TMOs in OSCs and PSCs

4.1. TMOs as HTLs in OSCs

TMO, where a transition metal is bonded to oxygen, is one of the most widely studied class of solid compounds that shows diverse

structures and semiconducting properties.^[162,163] They have been widely applied as HTLs in OSCs and PSCs with both the regular and the inverted architecture. The most successful applications in OSCs are discussed in the following sections and shown in Table 1.

4.1.1. MoO_x in OSCs

As a notable example, a high- W_F MoO_x was proposed as an efficient HTL in OSCs, as it can form layers with excellent quality and controlled thickness by various deposition techniques. Especially, they have been of paramount importance in BHJ OSCs, where the interface between the HTL and the anode (hole-selective contact) has been reported to play a major role in efficient hole extraction.^[164]

Lee et al.^[165] inserted in both polymer and small-molecule cells MoO_3 interlayers between the ITO bottom anode electrode and the active layer (a mixture of poly(3-hexylthiophene-2,5-diyl) with phenyl-C61-butyric acid methyl ester, P3HT:PCBM, for

Table 1. PV parameters of OSCs using TMOs as HTLs.

HTL	Organic absorber	PCE [%]	J_{sc} [mA cm ⁻²]	V_{oc} [V]	FF	Ref.
MoO_3	P3HT:PC ₆₁ BM	3.08	7.20	0.59	0.68	[165]
MoO_3	P3HT:PCBM	3.46	9.15	0.60	0.63	[168]
MoO_3	P3HT:PCBM	4.03	10.20	0.61	0.65	[169]
$H_{12}MoO_{3-x}$	P3HT:PC ₇₁ BM	4.34	11.64	0.69	0.54	[166]
MoO_x :Cs	PBDTDTT-S-T:PC ₇₁ BM	6.00	15.68	0.61	0.63	[170]
H_yWO_{3-x}	PCDTBT:PC ₇₁ BM	6.00	10.50	0.89	0.64	[174]
WO_3	P3HT:PCBM	3.04	7.79	0.60	0.64	[86]
$V_2O_5 \cdot nH_2O$	PBDSe-DT2PyT: PC ₇₁ BM	5.87	13.96	0.72	0.59	[182]
$s-V_2O_x$	PFDT2BT-8:PC ₇₀ BM	5.90	10.20	0.87	0.67	[185]
$V_2O_x(sol, N_2, N_2)$	P3HT:PCBM	3.34	8.13	0.59	0.65	[186]
V_2O_x :Cs	PBDTDTT-S-T:PC ₇₁ BM	6.08	15.81	0.63	0.61	[170]
NiO_x	P3HT:PCBM	3.54	12.31	0.645	0.44	[190]
NiO_x	P3HT:PCBM	3.60	8.60	0.583	0.71	[191]
O_2 - NiO_x	d-DTS(PTh ₂) ₂ :PC ₆₁ BM	5.10	12.30	0.735	0.56	[193]
NiO	P3HT:PCBM	5.16	11.30	0.638	0.69	[192]
NiO_x	TQ1:PC ₇₁ BM	6.42	10.50	0.87	0.70	[197]
NiO_x	PCDTBT:PC ₇₀ BM	6.70	11.50	0.88	0.65	[188]
NiO_x	PBDTTT-C-T:PC ₇₀ BM	7.42	15.82	0.75	0.625	[195]
NiO	pDTG-TPD:PC ₇₁ BM	7.82	13.90	0.82	0.68	[196]
e-CuO	P3HT:PC ₆₁ BM	3.91	10.98	0.63	0.571	[199]
CuO_x	P3HT:PC ₆₁ BM	4.02	11.90	0.53	0.64	[198]
Cu_2O	P3HT:PCBM	4.13	12.14	0.58	0.59	[202]
CuO_x	P3HT:PC ₆₁ BM	4.14	10.10	0.63	0.65	[201]
CuO_x	PBDTTT-C:PC ₇₁ BM	5.84	15.03	0.71	0.55	[201]
UVO-treated CuO	PCDTBT:PC ₇₁ BM	6.44	10.58	0.89	0.68	[203]
CuO_x	PBDTTT-C:PC ₇₀ BM	7.14	16.86	0.71	0.60	[200]
Cu_2O	PTB7:PC ₇₁ BM	8.51	16.40	0.77	0.66	[205]
O- CuO_x	PTB7:PC ₇₁ BM	8.68	16.44	0.74	0.71	[204]

polymer cells) to facilitate the hole transport process. In polymer cells, the insertion of MoO_3 improved the FF and the PCE (for about 4% and 16%, respectively) while also reduced the series resistance compared with reference cells using poly(3,4-ethylenedioxythiophene)-poly(styrenesulfonate) (PEDOT:PSS). The UPS measurements revealed that the insertion of MoO_3 has changed the energetic alignment at the heterointerfaces.

Vasilopoulou et al.^[166] reported an extensive study on the correlation between the structure (Figure 6a), stoichiometry (Figure 6b), and electronic properties (Figure 6c) of MoO_x . They demonstrated that both V_O and W_F can be precisely controlled through depositing nonstoichiometric MoO_x in the reducing environment to beneficially tune the oxides electronic structure (Figure 6d,e). They found that the significant

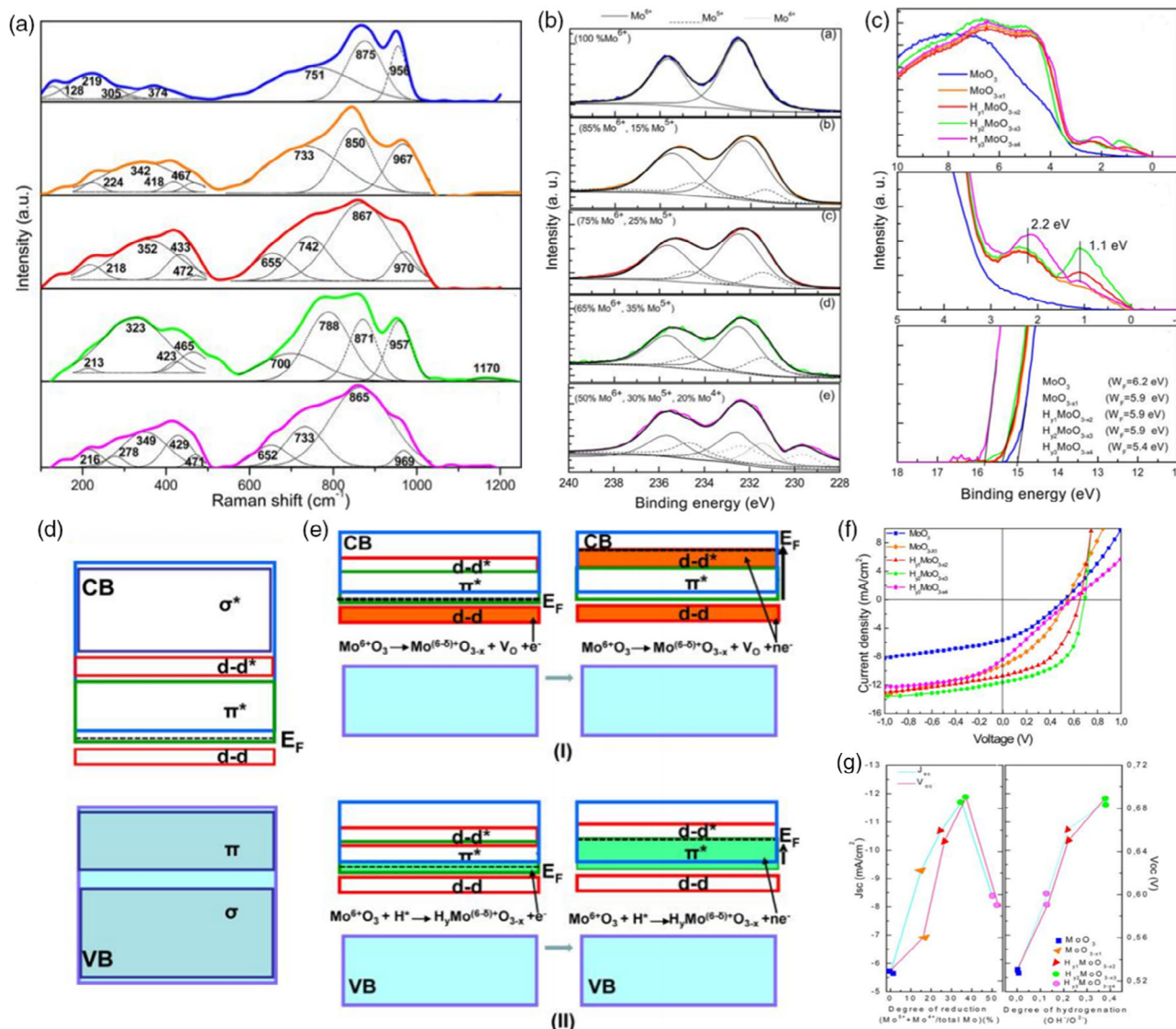


Figure 6. a) Raman of the fully oxidized and hydrogenated Mo oxides prepared in different environments; from top to bottom: MoO_3 , deposited in oxygen environment; MoO_{3-x1} , deposited in nitrogen; $\text{H}_{0.1}\text{MoO}_{3-x2}$, deposited in forming gas (FG, 90% N_2 and 10% H_2); $\text{H}_{0.2}\text{MoO}_{3-x3}$, deposited in pure hydrogen and e) $\text{H}_{0.3}\text{MoO}_{3-x4}$, deposited in FG while also injecting H_2 pulses. b) XPS and c) UPS spectra of the same Mo oxide films. In (c), it is shown from top to bottom: VB spectra, near the E_F region VB and secondary-electron cut-off region. d) Illustration of the band structure of MoO_3 , where the occupied orbitals with the dominant O 2p character comprises the VB, whereas empty orbitals with mainly the Mo 4d character comprise the CB. The d-d bands attributed to Mo-Mo bonds formed in the distorted lattice of the oxygen-deficient Mo oxides are also shown. e) Schematic illustration of the evolution of gap states occupation and Fermi-level movement toward higher a BE in MoO_x (I) with the progress of oxygen vacancy formation in hydrogen-poor reducing environments and (II) with the evolution of hydrogenation. f) Current density versus voltage characteristics for P3HT:PCBM BHJ devices embedding 5 nm MoO_x hole extracting layers. g) Variation of J_{sc} and V_{oc} with the degree of reduction (the portion of Mo atoms with oxidation states 5^+ and 4^+ relative to the total Mo cations, as derived from 3d Mo XPS measurements) and the hydrogen content (the amount of Mo-OH relative to Mo-O bonds, as derived from O 1s XPS results), respectively. Reproduced with permission.^[166] Copyright 2012, American Chemical Society.

enhancement of OSC performance was achieved when using hydrogenated Mo oxides with an optimized hydrogen content as the HTL/extraction (Figure 6f,g), as a result of the favorable energy-level alignment at the metal oxide/organic interface and enhanced charge transport through the formation of a large density of gap states near the Fermi level.

The PEDOT:PSS component has been reported to play a significant role regarding degradation issues in inverted OSCs,^[73] as its phase separation to PEDOT rich and PSS rich results in more rapid degradation, which becomes more intense under high humidity conditions. MoO₃, V₂O₅, and WO₃ have been reported as potential substitutes of PEDOT:PSS in inverted OSC. MoO₃ is considered an extremely promising alternative due to energy alignment levels and its high W_F (≈ 6.9 eV for the fully stoichiometric compound).^[167] Weerasinghe et al.^[168] compared the performance of OSCs using MoO₃ as the HTL with those using PEDOT:PSS and both showed degradation issues in high humidity levels. This could be attributed to the alternatives of the W_F and conductivity properties of MoO₃ due to humidity. Also, under UV radiation, the W_F of MoO₃ shifted due to the fact that MoO₃ releases oxygen, which consequently lowers Mo oxidation states. Furthermore, even without UV radiation and just under high heat conditions, Mo undergoes reduction due to its interaction with the Al contact.^[169]

Li et al.^[170] addressed the earlier-mentioned degradation issues of OSCs using PEDOT:PSS by intercalating different

mole ratios of Cs in V₂O_x and MoO_x layers of varying thicknesses that can be efficiently used as HTLs. Also, a constraint for the preparation of such intercalated oxide layers has been their high annealing temperature. They managed to process these layers at room temperature and fabricated both normal and inverted OSCs. **Figure 7** shows the layer-by-layer energy diagram of all the materials, as studies have reported the significance and impact that the alignments of these energy levels can have in the performance of OSCs.^[171,172] They demonstrated the dependence of the W_F of the resultant oxide layers on the varying molar ratio of the intercalated Cs. Their report also emphasizes the prospect of tunability of the W_F by altering the Cs molar ratio, with MoO_x and V₂O_x demonstrating W_F values changing for about 1.14 and 1.31 eV, respectively. Both inverted and regular structures have been tested and the devices using small-bandgap polymer semiconductors in the active layer along with Cs-intercalated oxide interlayers achieved efficiency values compared with those obtained in PEDOT:PSS OSCs, demonstrating the potential of MoO_x:Cs and V₂O_x:Cs HTLs.

4.1.2. WO₃ in OSCs

One of the main factors that limit the performance of OSCs is charge carrier recombination losses due to the poor charge carrier mobility of the photoactive layer.^[173] Oxygen deficiencies

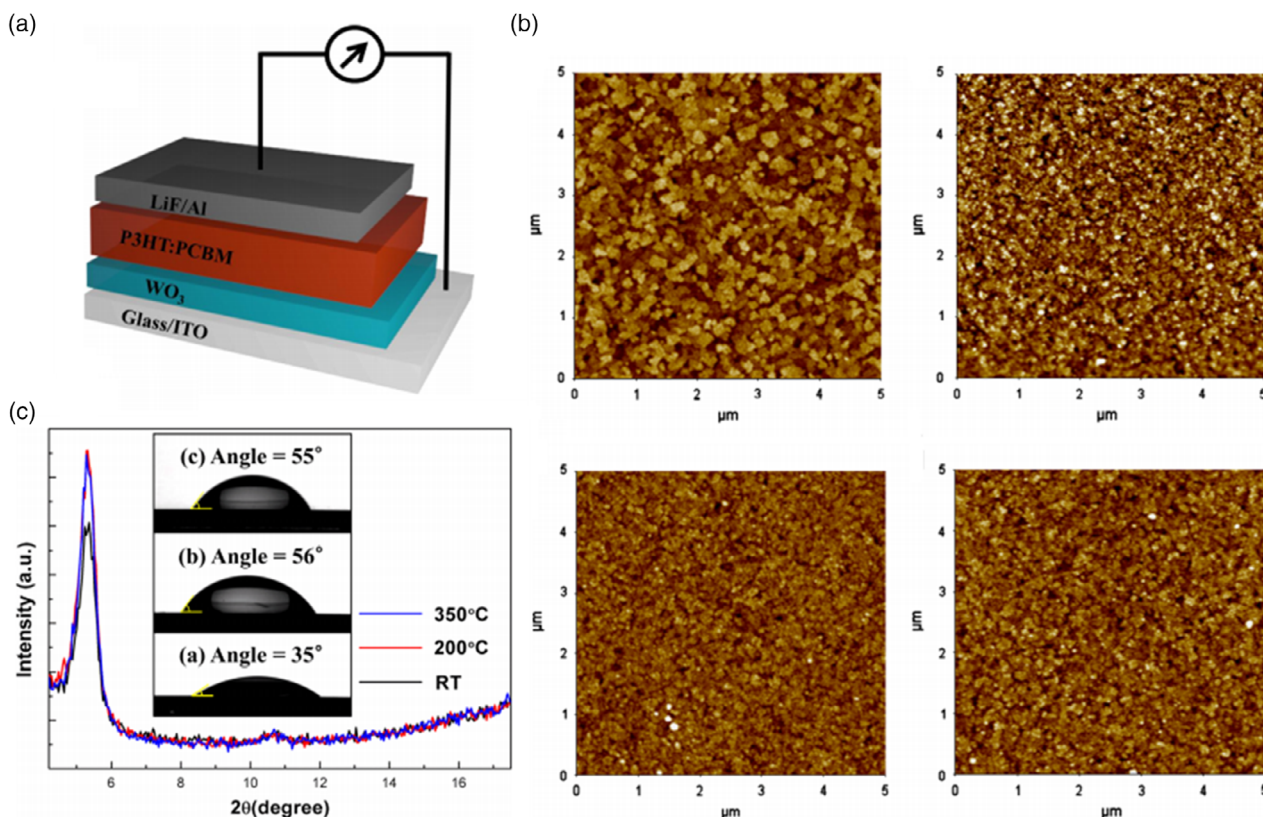


Figure 7. a) The structure of OSCs with the WO₃ interlayer of different thicknesses for different temperatures: ITO/WO₃/P3HT:PCBM/LiF/Al. b) AFM images of (up, left) bare ITO, (up, right) WO₃ on ITO (RT), (down, left) WO₃ on ITO (200 °C), and (down, right) WO₃ on ITO (350 °C). XRD spectra of P3HT films on WO₃ films for different annealing temperatures. Inset: The contact angles of the WO₃ films with increasing temperature. Reproduced with permission.^[86] Copyright 2013, Elsevier.

in TMOs have been reported as a potential method to reduce these losses. Vasilopoulou et al.^[174] fabricated high-efficiency conventional OSCs by intercalating hydrogen ions in the WO₃ lattice. The resultant hydrogenated tungsten trioxide demonstrated high charge carrier mobility due to the formation of partially occupied energy states close to the Fermi level. These states facilitated fast electron extraction toward the anode (hole-selective contact) and increased the device built-in field, hence reducing undesired recombinations.

Nonstoichiometric tungsten oxides demonstrate unusual defects that significantly improve their electric behavior. Still, tungsten oxides have drawbacks that have to be considered. Their low solubility in polar solvents and low crystallinity when processed at low temperatures along with wide-bandgap values and their instability issues are their more severe drawbacks.^[175] Oxygen vacancies in WO_x have been reported to significantly narrow the relatively wide bandgap. That is mainly due to the formation of energy states below the CB due to oxygen deficiencies.^[85] Regarding their instability, it has been explained on the basis of their high photocatalytic activity. More specifically, the CB of WO₃ is higher than the reduction potential of H₂/H₂O and the VB is higher than the oxidation potential of H₂O/O₂. This explains the high degradation effect that occurs when it is used alongside organic compounds.^[176] One of the characteristic properties of tungsten oxides is their easily adjustable morphology. The temperature conditions along with the precursor concentration have been reported to heavily affect the morphological properties of WO_xS.

Lee et al.^[86] replaced PEDOT:PSS with WO₃ as an interlayer between the anode and the active layer (Figure 7a). In the same study, the PCE values of the fabricated devices improved with increased thickness of the deposited WO₃ layer due to the improved morphology (Figure 7b), crystallinity, and hydrophobicity (Figure 7c) of WO₃ annealed at high temperatures. For WO₃ layers thicker than 40 nm though, the PCE started to decrease. Thus, 40 nm is reported as the optimal thickness. Another factor that affects the performance of the devices is the annealing temperature applied after WO₃ deposition. They demonstrated that the wetting properties of WO_x strongly affect the growth and nanomorphology of P3HT used as the donor component in the photoactive absorber layer. After pouring droplets of diionized (DI) water during the annealing of WO₃ layer, Lee et al.^[86] managed to increase the WO₃ hydrophobic behavior. They also reported that higher annealing temperatures resulted in an increase in the W_F of the WO₃ film. Generally, hydrophobicity increases the crystallinity of the P3HT film, which significantly improves hole mobility. Also, the undesired aggregation of PCBM acceptors can be avoided using a hydrophobic layer.^[177] Moreover, Jafari et al.^[178] also reported that annealing at 350 °C results in the formation of a smooth and crystalline interlayer of high hydrophobicity. Thus, hydrophobic interlayers have the potential to improve the crystallization of the photoactive blends used in OSC technology.^[179,180] When introducing small amounts of dopants like H, Na, or Li, they were able to formulate stability at high-temperature applications in the cubic c-WO₃ phase. An additional advantage of WO₃ and tungsten oxides, in general, is their stability in different pH environments. Moreover, they are very stable in acidic

environments, as under these conditions they are not soluble. Remarkably, WO₃ can withstand extremely high temperatures, as its melting point is around 1473 °C.^[181]

4.1.3. V₂O₅ in OSCs

Acquiring films of sufficient quality using solution-processed high- W_F metal oxides needs high annealing temperatures along with other post-annealing processes (e.g., plasma post-treatment).^[182] Vanadium oxide-based layers, however, can be deposited in ambient air conditions at low temperatures.^[183] For example, vanadium pentoxide (V₂O₅) layers have been reported to result in high-quality thin films without the need for any post-treatment processes.

Jiang et al.^[182] reported a melting–quenching sol–gel process for the preparation of the V₂O₅ layer, which was enabled by a higher solubility of V₂O₅ nanocrystals that was an issue in other related reports.^[184] These authors applied the hydrated vanadium pentoxide layer (V₂O₅·*n*H₂O), with water concentration being adjustable through thermal treatment, to replace PEDOT:PSS HTL. The inclusion of such an HTM improved the crystallinity of the active layer and the fabricated devices illustrated enhanced charge generation and collection efficiencies and reduced recombination losses.

As already mentioned, low-temperature synthesis and deposition methods under ambient conditions for OSCs using TMOs are highly desirable. Alsumani et al.^[185] included V₂O_x interlayers (acquired from a vanadium oxytriisopropoxide precursor) in OSCs and investigated their performance characteristics at different annealing temperatures. **Figure 8** shows the energy levels of the materials used in this study, including the HOMO and LUMO levels, along with the chemical structure of the active layers. The *J*–*V* characteristics and transmission spectra of the s-V₂O_x devices using different annealing temperatures for the metal oxide HTLs along with their Tauc plots derived from absorption measurements for the estimation of the bandgap energy are also shown in the same figure. It is shown that, at relatively low annealing temperatures of the metal oxide, the performance characteristics of the devices seem to stay unaffected. At higher temperatures, a decrease in the operational characteristics, especially of the V_{oc} values, is obtained, which can be attributed to the reduced shunt resistance values. The absorption spectroscopy results indicated that the variations of the optical bandgap of V₂O_x did not affect the performance of the devices. A large efficiency reduction was reported when the s-V₂O_x layers were annealed at 400 °C, which was explained by the increased number of oxygen vacancies that are generated at higher temperatures.

Hancox et al.^[186] further investigated how atmospheric conditions affect the performance of polymer solar cells using a solution-processed V₂O_x interlayer. When comparing the metal oxide devices with PEDOT:PSS ones, the V₂O_x-based OSCs illustrated similar performance and stability characteristics. However, they showed efficiency reduction under ambient temperature-processed V₂O_x-based devices, which were attributed to a bandgap reduction of the oxide. Such performance

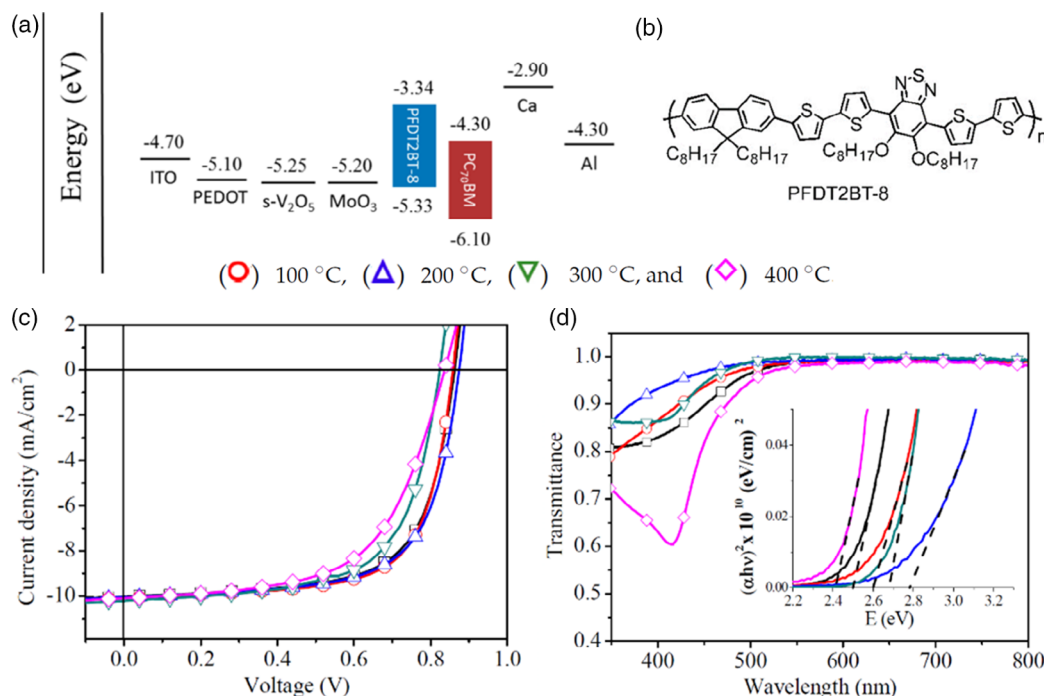


Figure 8. a) Energy-level diagrams of the different materials used by Alsulami et al. b) PFDT2BT-8 chemical structure. c) *J*-*V* curves and d) optical transmission spectroscopy and Tauc plots of V₂O_x devices tested at different temperatures. Reproduced with permission.^[185] Copyright 2016, MDPI.

decline was not observed when the metal oxide was processed under N₂ conditions, which was explained on the basis of the formation of an impurity-free material.

4.1.4. NiO_x in OSCs

Among the TMOs mentioned earlier, nickel oxide (NiO_x) has been widely used as an interfacial layer, improving charge carrier injection/transport in organic optoelectronic devices, especially in inverted OSCs, due to its excellent electronic properties, high transparency in the visible light, along with good environmental stability.^[97,187–189] NiO_x is an ideal material for the HTL offering excellent hole transport, as well as electron blocking properties, attributed to its well-matched VB with the HOMO level of many polymer donors and the high-lying CBM, respectively. In the past decade, NiO_x thin films have been deposited with various techniques and incorporated as efficient interfacial layers in OSCs.

Wang et al.^[190] developed Ni thin layers using thermal evaporation, followed by oxygen plasma treatment to oxidize the pure Ni film and form NiO_x layers, and investigated the influence of these layers thickness on the OSCs performance. Olson's group^[191] deposited a solution-processed NiO film on ITO substrates, using a Ni metal-organic ink precursor, followed by thermal annealing at 250 °C along with oxygen plasma treatment. Interestingly, it was found that the O₂-plasma surface treatment of the NiO film was critical to the device performance, exhibiting reduced series resistance and improved FF compared with the reference device with PEDOT:PSS HTL. The improvement was attributed to the increase of the NiO *W_F* after O₂-plasma

treatment. The same group^[188] also investigated the optoelectronic properties of pristine and oxygen plasma-treated NiO HTLs using UPS and inverse photoemission spectroscopy (IPES) measurements (Figure 9). An increase in the *W_F* of 0.5 eV was demonstrated for the modified NiO sample, leading to enhanced hole transport and device performance. In addition, the insertion of the NiO HTL in OSCs improved the device stability, maintaining 82.7% of the initial PCE value after 450 h.

In another study, Irwin and coworkers^[192] demonstrated the efficient application of NiO as an HTL in BHJ P3HT:PCBM-based OSCs deposited by pulsed layer deposition (PLD) on the ITO anode. OSCs based on a 5–10 nm thin NiO anode interfacial layer exhibited a high PCE of 5.16%, whereas the control device showed a poor PCE value of 2.87%. The dual role of NiO as the hole transporting and EBL was also reported, as the VB of NiO was aligned to the HOMO level of P3HT, leading to a favorable ohmic contact at the BHJ/anode interface, whereas its wide bandgap prevented electron transfer to the anode.

The hole transporting and electron blocking properties of NiO were also investigated by Ratcliff et al.^[98] It was found that the large bandgap of NiO substrates and the formation of a strong dipole at the PCDTBT:PCBM photoactive layer/anode interface facilitated hole transfer from the organic layer to the HTL, leading to a high PCE value of 6.7% for the NiO-based OSCs. Furthermore, Garcia et al.^[193] reported the influence of NiO properties and interfacial chemistry on OSCs performance using as photoactive layer the d-DTS(PTTh₂)₂:PCBM blend. OSCs based on the NiO HTL exhibited a PCE value of 5.1%, which was much higher than that of the reference device with the PEDOT:PSS HTL (PCE of 2.3%). It is suggested that the poor

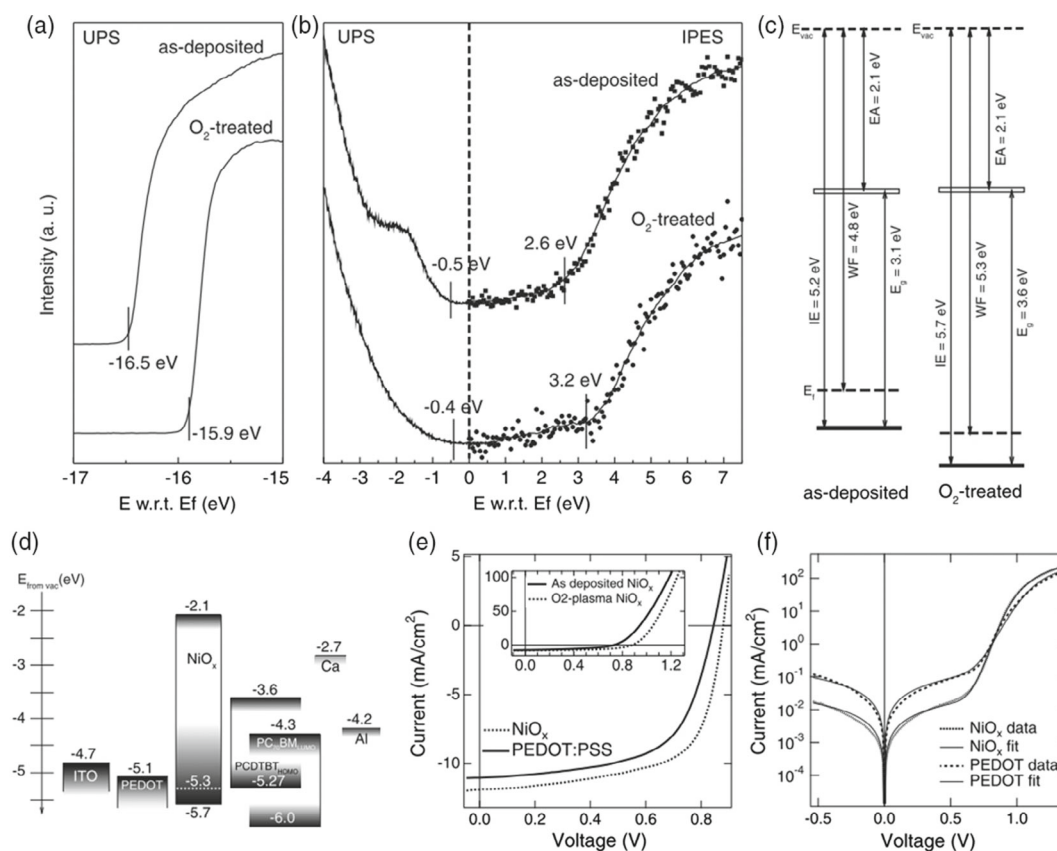


Figure 9. UPS and IPES measurements of the DOS near the VB edge and CB and the resulting band energies. a) UPS spectra (He I) of the photoemission cut-off, showing an increase in the WF after O₂-plasma treatment of the NiO_x. b) Combined UPS and IPES spectra of NiO_x near the VB and CB edge. c) Energy-level diagrams of NiO_x before and after O₂-plasma treatment. d) Schematic showing architecture and energy levels of the OSCs. e, f) Current voltage and dark *J*-*V* characteristics of OSCs. Reproduced with permission.^[188] Copyright 2011, WILEY-VCH.

efficiency of reference OSCs was due to the chemical interaction of PEDOT:PSS with the active layer, whereas no such interfacial chemical interactions were observed in the case of the NiO HTL, according to XPS and UV-vis spectroscopy measurements. To strengthen the opinion that NiO is an outstanding hole transporting interfacial layer, Irwin et al.^[194] studied the structural and electronic functionality of the NiO HTL in BHJ OSCs. It was found that NiO films deposited with pulse laser deposition (PLD) were smooth, crystalline, and highly transparent in the visible range, as well as electrically passivating the ITO anode, reducing the hole extraction barrier, and preventing electron transport toward the anode. Consequently, the application of NiO as the HTL in OSCs resulted in enhanced electrical parameters and thus the device performance.

Fan et al.^[195] demonstrated the effect of the optimized thickness of the NiO_x anode interlayer deposited with a radio-frequency magnetron sputtering deposition system on the performance and stability of OSCs based on PBDTTT-C-T:PC₇₀BM photoactive layer. The OSC with the optimum 9 nm-thick NiO HTL exhibited not only a higher PCE value of 7.42% compared with the reference device (6.91%), but also enhanced long-term stability, maintaining 92.1% of the initial PCE value after 60 days. It was suggested that the enhanced stability of NiO-based OSCs was a result of the chemical robustness

and low reactivity of the NiO HTL; on the contrary, the acidic nature of PEDOT:PSS affected the BHJ film, thus leading to device degradation. In addition, solution-processed nonstoichiometric NiO was used effectively as the HTL in highly efficient and stable OSCs by Manders et al.^[196] The nonstoichiometry of NiO films was determined by XPS measurements, confirming the p-type conductivity of the metal oxide, whereas from the UPS results, the favorable energy-level alignment of the HTL with the pDTG-TPD:PC₇₁BM active layer was evident, leading to a high PCE value of 7.82%. The NiO layer also affected the morphology of the active layer deposited on top of it, due to the hydrophobic nature of NiO samples, inducing a smooth and homogeneous donor/acceptor phase nanomorphology at the HTL/active layer interface, resulting in improved hole transport.

Although low-cost solution-processed NiO films have been successfully used as HTLs in OSCs, the high processing temperature (over 250 °C) during film formation may prohibit the use of NiO in flexible optoelectronic devices. Bai et al.^[197] demonstrated the low-temperature approach of 175 °C to sufficiently convert the metal oxide precursor solution to thin NiO films. In addition, a high PCE value of 6.42% was obtained when low-temperature solution-processed NiO films were introduced as anode interfacial layers in OSCs based on TQ1:PC₇₁BM blend photoactive films.

4.1.5. CuO_x in OSCs

In the past decade, copper oxides, including cupric (CuO) and cuprous (Cu_2O) oxides, which are also p-type semiconductors, have been extensively used as HTLs in organic OSCs due to their advantages of being Earth-abundant sources, low-cost, and simplicity of film formation, along with their ability to form an ohmic contacts with the commonly used ITO anode electrode.

One of the first studies on the application of CuO_x as the interfacial layer in OSCs was demonstrated by Lin et al.,^[198] where the formation of the ohmic contact between the P3HT:PCBM photoactive blend films and the anode was reported. These authors demonstrated that the application of CuO_x as the HTL in OSCs resulted in reduced a hole extraction barrier, decreased series resistance, and thus improved device performance with a PCE value up to 4.02%. Similarly, Lien et al. reported the energy-level alignment at the active layer/electrode interface using a fully oxidized copper oxide HTL.^[199] CuO_x -based OSCs exhibited a PCE value of 4.06%, whereas the device showed improved stability, maintaining 75% of the initial PCE value. In another study, Xu et al. demonstrated the use of solution-processed CuO_x deposited from an environmentally friendly 1,2-dichlorobenzene solution of the $\text{Cu}(\text{acac})_2$ precursor, followed by thermal annealing at 80 °C to form the oxide from its precursor.^[200] CuO_x showed remarkable optoelectronic properties, including high transparency at the visible light and high W_F , facilitating hole transport, as well as reducing recombination losses, when used as HTLs in OSCs (Figure 10). Consequently, a high PCE value of 7.14% was obtained for the CuO_x -based OSC using a PBDTTT-C:PCBM BHJ layer. Moreover, Shen et al.^[201] introduced an ultrathin CuO_x ,

consisting of CuO and Cu_2O according to XPS measurements, as an HTL in OSCs. It was found that the CuO_x film exhibited a smoother surface and better hydrophobic properties compared with the widely used PEDOT:PSS HTL, resulting in a more favorable contact with the photoactive layer and beneficial hole transfer from the BHJ toward the anode. Therefore, an improvement in device performance was observed when CuO_x was used as the HTL in these OSCs, reaching a maximum PCE value of 4.14%, which was higher than those based on PEDOT:PSS (3.63%). The CuO_x -based device also showed enhanced stability, showing an efficiency loss of only 10% after 7 days. Yu et al.^[202] investigated the incorporation of Cu_2O between the photoactive layer and the anode of OSCs. The enhanced efficiency of Cu_2O -based devices was attributed to an improvement in hole transport and reduction of series resistance. In addition, Cu_2O acted as the protection layer of the underlying photoactive film, hence improving the long-term stability of the device.

Furthermore, low-temperature, low-cost, and environmental-friendly solution-processed CuO_x NPs were used successfully as HTLs in OSCs, by Zhang and co-workers.^[203] A UV-ozone treatment of CuO_x substrates was proposed to increase their W_F , resulting in favorable interfacial contact and improved hole transport/extraction. The fabricated OSCs using CuO_x NP HTLs showed improved performance as well as enhanced stability, ascribed to the less hydrophilic nature of CuO_x NPs compared with that of PEDOT:PSS. Chen's group demonstrated that UV-ozone transformed Cu_2O into CuO , which was found to be more efficient in facilitating the dissociation of photogenerated excitons into free carriers and thus increasing the photocurrent density of the device. Therefore, an OSC based on PTB7:PCBM with a CuO_x HTL exhibited a high PCE value of 8.68%

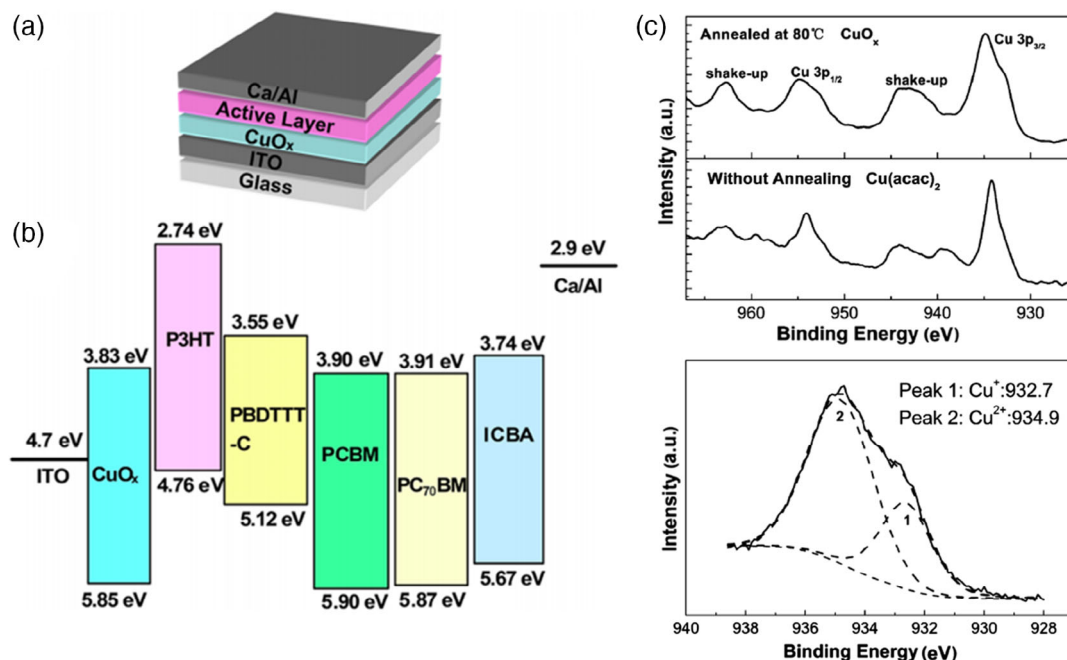


Figure 10. a) Device structure of the polymer solar cells. b) The HOMO and LUMO energy levels of the materials involved in the PSCs. c) XPS of CuO_x and $\text{Cu}(\text{acac})_2$ films on the silicon substrate: Cu 2p core-level spectra (upper panel) and typical deconvolution of the Cu 2p_{3/2} main peak of CuO_x (lower panel). Reproduced with permission.^[200] Copyright 2013, American Chemical Society.

and remarkable long-term stability.^[204] Recently, Guo et al.^[205] studied the use of highly transparent and p-conductive single-phase Cu₂O HTLs deposited by magnetron sputtering in OSCs. A 15% improvement in device performance was observed when Cu₂O was inserted as the interfacial layer in PTB7:PCBM-based OSCs compared with that using the PEDOT:PSS HTL, attributed to the well-matched HOMO level of PTB7 (donor polymer) with the VB of CuO_x, suggesting that copper oxides are promising HTMs for large-area PV technologies.

4.2. Metal Oxide Bronzes as HTLs in OSCs

Metal oxide bronzes have also been explored as HTLs in OSCs mainly due to their highly desirable conductivity induced from metal nonstoichiometry. Xie et al.^[161] developed a simple one-step synthesis method for low-temperature solution-processed hydrogen Mo and V bronzes with an excess of oxygen vacancies that increased their conductivities to serve as effective HTLs. The oxygen vacancy was found to play an essential role in the measured W_F values in these materials. Moreover, Soultati et al.^[206] synthesized Mo bronzes using a sol-gel method with the critical step being the partial reduction/hydrogenation of molybdenum oxide used in the precursor solution in the alcohol-based solvent. The bronze composition, stoichiometry, and electronic properties were correlated with the postannealing process. Hydrogen molybdenum bronze with a moderate degree of reduction was found to be highly advantageous as HTL because it maintained a high W_F , whereas it simultaneously exhibited a high density of occupied gap states near the Fermi levels. These were considered to serve as available paths for the transfer of holes toward the anode. Enhanced J_{SC} , V_{OC} , and FF were obtained for a variety of BHJ mixtures based on different polymeric donors and fullerene acceptors, compared with the reference devices using PEDOT:PSS.

4.3. TMOs as HTLs in PSCs

As already discussed, metal oxides exhibit a large variety of desired characteristics for use as HTLs in optoelectronic devices. They are transparent in the visible wavelength region, are either n- or p-type semiconductors with mobility, and have W_F values that can be precisely controlled through doping. They are, therefore, of interest for use as HTLs in the rapidly advanced field of PSCs (Table 2).

4.3.1. MoO_x in PSCs

MoO_x is incorporated as a HTM not only to reduce the cost of the fabrication process, but also to improve the performance of the devices. MoO_x can be paired with different electrode materials like Ag, Au, and especially Al, which improve the hole extraction process both in OSCs and in PSCs.^[207–209] According to Sanehira et al.,^[210] when MoO_x is used as the HTL combined with the Al electrode in PSCs, it inhibits the decomposition of the perovskite layer and enhances the performance and stability of the devices. The MoO_x PSCs, based on the same paper, showed lower humidity rates, indicating that the layer reduced the moisture retention in the perovskite-HTL interface. Apart from moisture retention,

Table 2. PV parameters of PSCs using TMOs as HTLs.

HTL	Perovskite absorber	PCE [%]	J_{sc} [mA cm ⁻²]	V_{oc} [V]	FF	Ref.
MoO _x	MAPbI ₃	12.26	17.06	1.02	0.693	[216]
MoO _x /F4-TCNQ	MAPbI ₃	16.26	20.17	1.06	0.760	[216]
Spiro/MoO _x	FAMAPbI _{3-x} Br _x	18.63	23.31	1.11	0.72	[218]
WO _x /PEDOT	(FA _{0.4} MA _{0.6} PbI _{2.8} Br _{0.2})	15.1	22.69	1.025	0.648	[228]
VO _x	MAPbI ₃	11.15	16.83	0.95	0.702	[233]
VO _x :0.3Cs	MAPbI ₃	14.48	20.67	0.92	0.765	[233]
PEDOT/VO _x	MAPbI ₃	14.22	20.3	0.969	0.722	[234]
NiO/DEA	MAPbI _{3-x} Cl _x	15.90	20.90	0.95	0.80	[246]
NiO	MAPbI ₃	16.03	22.61	1.058	0.699	[249]
NiO/F6TCNNQ	MAPbI ₃	19.75	22.05	1.12	0.80	[250]
NiO/PEAI	MAPbI ₃	20.11	24.21	1.092	0.761	[249]
NiO/F6TCNNQ	CsFAMA	20.86	23.15	1.12	0.802	[250]
CuO _x	MAPbI ₃	17.1	23.2	0.99	0.73	[270]
CuO _x	MAPbI ₃	17.43	22.42	1.03	0.76	[272]
FBT-Th4/CuO _x	MAPbI ₃	18.85	22.3	1.12	0.754	[272]

the devices illustrated lower absorption losses compared with devices using no HTL. The thickness of the HTL layer seemed also to play an important role in the performance and stability, with a thicker MoO_x layer that significantly lowers degradation rates and reduces the photobleaching effect, as shown via XRD analysis.

Although several reports have used MoO₃ as an interlayer to enhance the hole extraction in PSCs, its working potential is not fully utilized due to the following challenges: when MoO₃ is placed in direct contact with the perovskite layer, e.g., MAPbI₃, it leads to a chemical reaction creating nonperovskite species that deteriorate device performance.^[211] Also, the misalignment of the electronic levels of the two layers results in a less efficient charge carrier collection process. Schulz et al.^[212] revealed that the MoO₃/MAPbI₃ interface in PSCs leads to severe band bending and also caused a chemical reaction that limits device performance. This leads to the creation of interfacial states (ISs). They added a thin layer of Spiro-MeOTAD to minimize the direct contact between MoO₃ and the perovskite layer to inhibit the chemical reaction (Figure 11). Energy levels derived from UPS show that both MoO₃ and an interlayer of Spiro-MeOTAD resulted in 0.5 eV band bending of the MAPbI₃ layer toward the Fermi energy (E_F). It is noteworthy to add that the Fermi energy level of halide perovskites has shown to depend on the W_F of the substrate layer underneath, behaving either as an n-type or a p-type.^[207,213]

MoO₃ deposition on top of the perovskite layer has led to poor contact between the two layers which can limit device efficiency.^[214] Further, Liu et al.^[215] reported the formation of a MoO₂ transition layer at the perovskite/MoO₃ interface, which may inhibit device performance. This transition layer was formed due to the chemical reaction between the perovskite and the MoO₃ layer during MoO₃ deposition on the perovskite. The formation of the MoO₂ layer created a potential barrier of 1.36 eV for hole extraction. The authors suggested that, unless these interfaces

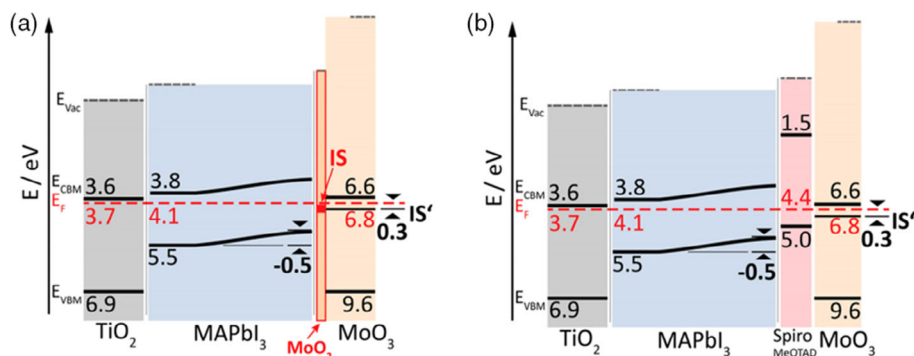


Figure 11. a) Energy-level diagram of MAPbI₃ PSCs using MoO₃ as a HTL. This leads to the creation of IS due to a chemical reaction between MoO₃ and perovskite. b) Incorporation of a thin organic HTL layer (Spiro-MeOTAD) inhibits such a chemical reaction. For each layer, the Fermi-level position (E_F , dotted line), work function (in red), electron affinity, and ionization energy (in black) are indicated in eV. Reproduced with permission.^[212] Copyright 2016, American Chemical Society.

properties are controlled to avoid degradation and the energy mismatch, MoO_x is not a preferred choice as the HTL in PSCs.

An efficient strategy to overcome interfacial degradation is the incorporation of an intermediate layer between the MoO_x and perovskite layer, i.e., the so-called bilayer HTL architecture. This has proven helpful not only in PSCs,^[216] but also in OSCs.^[217] For example, Chen et al.^[216] demonstrated that a thin layer of an organic molecule (F4-TCNQ) between solution-processed MoO₃ and MAPbI₃ perovskite increased the PCE from 12.06% to 16.26%. The devices also showed remarkable improvement in terms of operational stability. Incorporation a thin MoO_x layer between the HTL and top electrode in n-i-p PSCs has also shown to improve hole extraction and device performance. For example, Lin et al.^[218] showed an improvement in PCE from 17.02% to 18.62% when a thin MoO₃ layer was deposited between Spiro-OMeTAD and the Ag electrode. Impedance spectroscopy and dark current investigations revealed that this increase is due to a decrease in series resistance and inhibition of leakage current upon the incorporation of MoO₃ that resulted in a higher V_{OC} and FF. It is important to note that the thickness of the MoO₃ layer significantly influenced device performance. When the thickness was increased beyond 14 nm, the device performance started to decrease due to inefficient hole extraction, as shown in Figure 12.

It is noteworthy that the MoO_x/perovskite interface is not as successful for hole extraction as in the case of the MoO_x/organic absorber interface. This is because the MoO_x/perovskite interface, for both the inverted or regular architecture, leads to a high energy barrier for hole extraction and limits the achievable V_{OC} . For regular architecture,^[215] where the MoO_x layer was evaporated on top of the perovskite (MAPbI₃), the barrier height was ≈ 0.30 eV. For the inverted PSCs, the barrier height was found to be even higher (i.e., 0.8 eV), when MAPbI₃ was evaporated on top of the MoO₃ layer.^[211] More importantly, it was also found that MoO_x forms a reactive interface with perovskite, creating biproducts which act as recombination sites.^[211,212] This explains the generally lower PCE in PSCs using MoO_x.

The inferior performance can be overcome using interlayers that improve energy-level alignment and also avoid interfacial degradation. Pérez-del-Rey et al.^[219] showed that a thin (1–2 nm)

interlayer of 2,2',2''-(1,3,5-Benzinetriyl)-tris(1-phenyl-1-H-benzimidazole, TPBi, results in efficient charge extraction and a PCE exceeding 19%. The insertion of the TPBi interlayer also inhibits chemical reaction at the MoO₃/perovskite interface.

4.3.2. WO_x in PSCs

Tungsten oxides, both stoichiometric (WO₃) and nonstoichiometric (WO_{3-x}), are also investigated for PSCs. WO_x can be more suitable for building integrated PVs due to their electrochromic properties.^[220] In fact, WO_x can be used as both the ETL and the HTL due to their wide bandgap and energetics and high carrier mobility (20 cm² V⁻¹ s⁻¹).^[221–223] For instance, when used as an ETL, WO_x resulted in a higher J_{SC} than TiO₂ counterpart in PSCs using MAPbI₃Cl_{1-x} as an absorber layer and Spiro-OMeTAD as the HTL.^[224] The WO_x ETL showed a nearly identical transmittance as that of TiO₂ but a higher conductivity. In another report, Masi et al.^[225] used room temperature-processed WO_x carved nanorod (CNR) as the ETL and achieved a PCE higher than 13.3% in MAPbI₃ PSCs. The CNRs allowed for easy modification after the deposition through AcOH and UV treatment, resulting in improved hydrophilicity behavior, wettability, and reduced surface resistivity.

The presence of V_O in the WO_x film is a challenge that limits device performance. To minimize these vacancies, Ali et al. reported a room temperature-processed WO_{3-x} thin film using e-beam evaporation.^[226] To reduce the number of oxygen vacancies, the WO_{3-x} films were annealed at 300 °C for 1 h in air. XPS and electron paramagnetic resonance analysis of the as-deposited film with the annealed ones confirmed a reduction in oxygen vacancies in the latter. In another report, these V_O have shown their crucial dependence on device performance and stability in printable PSCs.^[227] It was shown that the presence of these vacancies makes them attractive toward moisture ingress and the devices showed a rapid degradation as compared with a control TiO₂-based PSC.

Toward the use of WO_x as the HTL, Yi et al. used WO₃ NPs–PEDOT:PSS composite to enhance the PCE of their perovskite solar cells.^[228] They noted $\approx 20\%$ improvement in the PCE

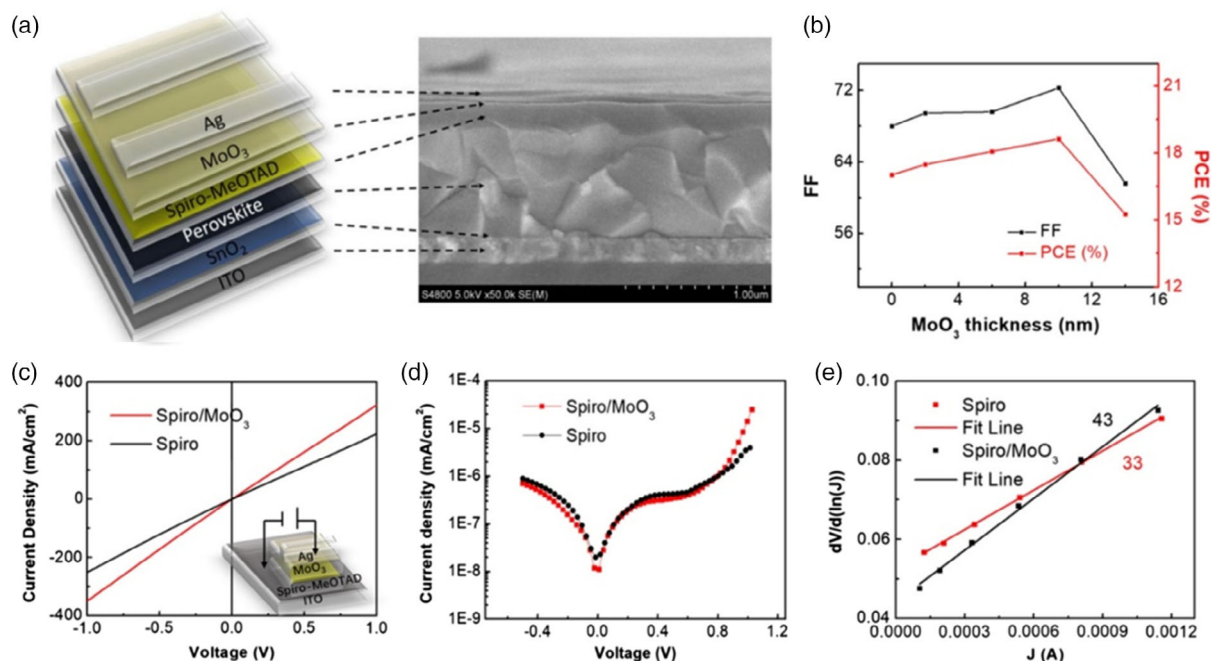


Figure 12. a) A schematic showing device architecture and cross section of PSCs using MoO₃ as a buffer layer. b) FF and PCE as a function of MoO₃ layer thickness. c) J - V curves of HTLs between two metal electrodes, showing the electrical properties. d) Dark J - V curves of PSCs using both HTLs. e) Plots of $d(V)/d(\ln J)$ versus J curves with and without MoO₃ in the dark condition. Reproduced with permission.^[218] Copyright 2018, Springer Nature.

as compared with a pristine PEDOT:PSS HTL counterpart. The WO₃/PEDOT:PSS HTL showed a PCE of 15.1%, which originated from simultaneous improvement in FF, V_{OC} , and J_{SC} . The incorporation of WO₃ NPs increased hole mobility and filled the voids in the PEDOT:PSS HTL surface and also formed an interface with perovskite absorber with a lesser defect density and interfacial recombination, as characterized using a series of characterizations (electrochemical impedance spectroscopy [EIS] and space-charge-limited current-voltage [SCLC] measurements). In another report, p-i-n planar PSCs using WO_x HTLs showed a PCE of around 8%.^[229]

4.3.3. V₂O₅ and VO_x in PSCs

VO_x has emerged as a suitable alternative to the highly reactive MoO_x HTL. VO_x is also a wide-bandgap TMO ($E_g > 2$ eV) with a low-lying CB. Its charge transport properties heavily depend on the concentration of V₅₊.^[230,231] Chu et al.^[232] reported the low-temperature (50 °C) ALD of VO_x as the HTL in PSCs. A VO_x thin layer of 1 nm resulted in PCE 11.53%. It was reported that the as-deposited VO_x film is not suitable as a HTL and a UV post-treatment is required to enhance hole extraction from the perovskite layer and attain high performance. Photoelectron spectroscopy studies suggested that, upon UV treatment, the density of V⁵⁺ defect states that are responsible for hole extraction increases. Doping in VO_x HTL has been shown to improve hole extraction properties. Yao et al. showed that the doping of VO_x with cesium hydroxide monohydrate (VO_x·yCs, y being the Cs/V molar ratio) enhanced device performance by around 30%.^[233] Cs doping

resulted in enhanced conductivity and a higher J_{SC} and FF as compared with the devices using undoped pristine VO_x layers.

A more successful strategy is to use VO_x as a bilayer HTL configuration. For example, VO_x-PEDOT:PSS bilayer HTL in inverted PSCs showed improved band alignment and a higher V_{OC} .^[234] The champion devices showed a nearly hysteresis-free PCE of $\approx 14.22\%$, which is higher than the PEDOT:PSS counterpart. A similar improvement is demonstrated in the work of Wang et al., where the V₂O₅-PEDOT:PSS bilayer HTL demonstrated around 20% improvement in PCE,^[235] compared with conventional PEDOT-only devices. EIS measurements revealed that recombination resistance of the bilayer-based devices were 57% higher than the control devices. The bilayer HTL-based PSCs also showed interfacial capacitance and negligible hysteresis. VO_x was also used in two-terminal tandem PSCs to simultaneously address the two key challenges, e.g. parasitic absorption and long-term instability, which primarily arise due to the widely used Spiro-OMeTAD HTL. Bagri et al.^[236] used the 9 nm air-stable VO_x (via ALD) and 30 nm undoped Spiro-OMeTAD in a bilayer HTL configuration, leading to a nearly semitransparent PSC. The PSC made using this bilayer HTL showed $\approx 15\%$ higher J_{SC} as compared with a control device using 150 nm of the doped Spiro-OMeTAD HTL. The devices used Cs_{0.17}FA_{0.83}Pb(Br_{0.17}I_{0.83})₃ as the photoactive layer and ALD VO_x/ITO as the top contact. It is noteworthy that, while the ALD of VO_x slightly increased the surface roughness (see Figure 13), the surface height distribution showed an improvement. In fact, the VO_x films seemed to adapt the morphology of the underneath substrate layer.

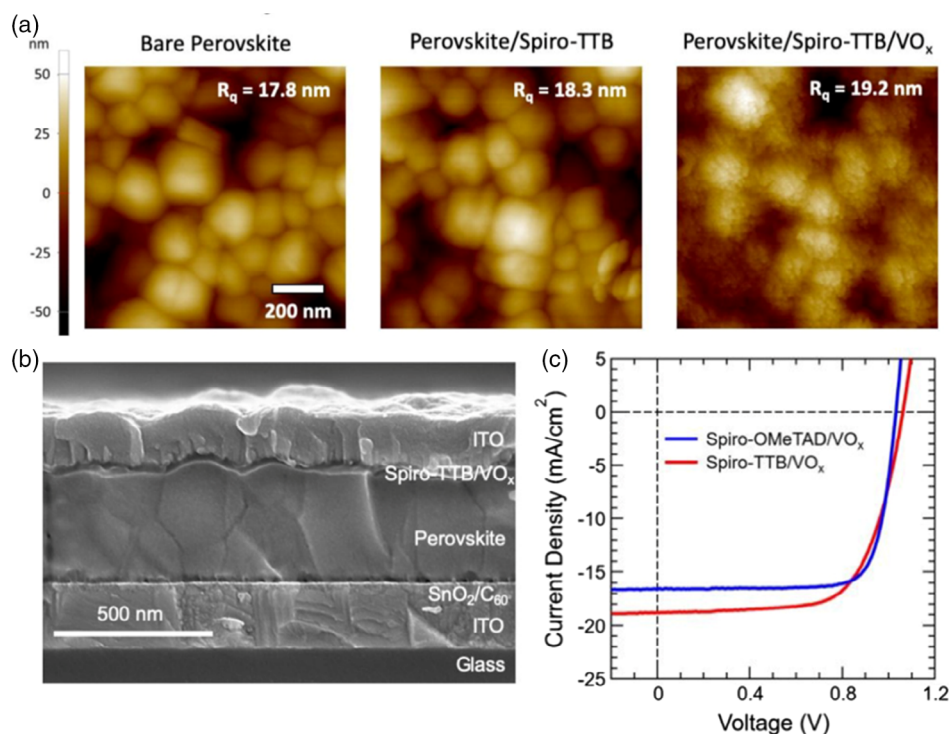


Figure 13. a) AFM images of a bare perovskite ($\text{Cs}_{0.17}\text{FA}_{0.83}\text{Pb}(\text{Br}_{0.17}\text{I}_{0.83})_3$) film and those deposited on two types of HTLs. Scan rate is $1 \mu\text{m} \times 1 \mu\text{m}$. Root mean square roughness (R_q) values are shown in the inset of each image. b) The SEM image showing a cross section of the PSC and c) the current–voltage characteristic curve of PSCs using two types of HTLs. Reproduced with permission.^[367] Copyright 2019, the Royal Society of Chemistry.

4.3.4. NiO_x in PSCs

NiO_x has emerged as one of the most reported and successful HTLs in PSCs for both p–i–n and n–i–p configurations.^[11,110,159,237,238] However, proper attention is required to control the surface properties of NiO . The chemistry of the NiO surface is influenced by the coexistence of different oxidized Ni phases (e.g., NiO , $\text{Ni}(\text{OH})_2$, Ni_2O_3 , and NiOOH), as revealed by XPS investigations^[172,239,240] and determined by the preparation conditions.^[241] For instance, increasing the annealing temperature from 275 to 400 °C (within the range used to anneal the NiO hole-selective layers for PSCs and OSCs) reduces the surface concentration of hydroxides together with the W_F (by about 0.5 eV).^[242] Moreover, the exposure to the strong oxidizing environment (such as in UV–ozone or oxygen–plasma treatment) induces the formation of a NiOOH superficial layer, which increases the W_F and the conductivity of the material.^[243] The Ni^{3+} states are energetically localized within the bandgap of NiO ^[244,245] and might promote surface or interface recombination in PV devices.^[237] The passivation of these defects is required to reduce the PV losses.

Interfacial engineering is the winning strategy in this direction and it can be accomplished by introducing the molecular monolayer, polymers, or additional inorganic materials on the surface of NiO . Bai et al. introduced a self-assembled monolayer (SAM) of diethanolamine on the surface of NiO ,^[246] exploiting the binding of the amine group to the Ni cations. The modified NiO had a deeper VBM, from -5.12 to -5.17 eV, and a lower W_F ,

from 4.47 to 4.41 eV, suggesting chemical passivation of the surface. Further, the MAPbI_3 perovskite (with the addition of chloride in the precursor solution) was of better quality on the modified NiO , with device efficiency increasing from 11.5% to 15.9%, mainly due to an improved FF. One advantage of the molecular monolayer is the possibility to transfer whatever the desired molecular function to the NiO surface.^[247] Wang et al.^[248] investigated the effect of a series of para-substituted benzoic acid, modifying the adhesion and growth of the perovskite layer on NiO and, more interestingly, systematically tuning the W_F of the HTL. The perovskite quality improved with methoxy- and halide-substituted acids and worsened with an amine, whereas a direct correlation between the molecular dipole and the V_{OC} of the devices was observed. Halide-substituted benzoic acids deepened the VBM of NiO , increased the devices' built-in potential, and reduced interface recombination. Top performing devices were obtained out of p-bromide benzoic acid, benefiting also from improved hole transfer. A different approach to improve the p-type interface properties is the insertion of molecules, enabling an energetic cascade for the holes from the perovskite to NiO , as demonstrated by Cheng et al.,^[249] who introduced pyridine-terminated organic molecules with the phenothiazine (electron-donating) group as the core of the skeleton, improving all the PV parameters. Consequently, the PCE increased from 12.53% to 17.00% upon surface modifications of NiO_x with pyridine derivatives. The alignment of the NiO /perovskite interface can be also improved, using the strong electron acceptor F6TCNNQ, whose LUMO is at -5.37 eV, as

demonstrated by Chen et al.^[250] The molecular layer was formed upon surface p-type doping, with excess electrons lying on F6TCNNQ and the doped NiO surface undergoing a slight reconstruction. The difference between the VBM and E_F for NiO was reduced from 0.58 to 0.29 eV with subsequent improved hole transfer, enabling a record device with 20.86% PCE (the control device was 19.75% efficient).

The fact that such a large variety of different molecules, as well as polymers^[251] or chemical treatments,^[252] were successfully demonstrated to improve the NiO/perovskite interface supports our statement that the optoelectronics at this interface is not intrinsically of top quality. One limiting factor could be the quality of the underlying perovskite, which has been addressed by several authors. Recently, Glowienka et al. proposed that the NiO/perovskite interface can be modeled by introducing the concept of the “dead layer”,^[253] which is a physical region of few-nm thickness with very high nonradiative recombination. Although a structural hypothesis for this dead layer was not provided by the authors, it was shown that the introduction of PTAA as a passivation agent reduced the thickness and the impact of this dead layer, according to the model proposed. A reasonable hypothesis is that the dead layer arises from the strain in the perovskite due to its lattice mismatch with NiO. This is in line with the work of Tsai et al.,^[254] showing that light soaking reduces the strain in the perovskite, improving the energetic of the NiO/perovskite interface. Along with strain effect, the firsts perovskite layers can shift from the metal halide perovskite stoichiometry by incorporating oxygen due to chemical reactions with NiO during the

device fabrication, as suggested by Lin et al.,^[255] who observed a $\text{MAPbI}_{3-2\delta}\text{O}_\delta$ interface phase and proposed a beneficial effect from this mixed halide-oxide compound in promoting the hole transfer.

Yu et al.^[256] demonstrated significant suppression of interfacial recombination by facile alkali chloride interface modification of the NiO_x HTL in inverted planar PSCs (Figure 14). Experimental and theoretical results revealed that the alkali chloride interface modification resulted in significantly improved ordering of the perovskite films, which in turn reduces defect/trap density, causing reduced interfacial recombination and hence increased V_{OC} from 1.07 V for pristine NiO_x to 1.15 V for the KCl-treated one. As a result, a PCE approaching 21% was obtained. Furthermore, the suppression of ion diffusion in the potassium chloride (KCl)-treated NiO_x devices improved their stability.

Ionic conduction properties of lead halide perovskites force us in considering that the interface quality is a dynamic feature. The lack of current density–voltage (J – V) hysteresis in NiO-based p–i–n PSCs does not necessarily imply that ion migration is suppressed, and this can have a strong impact on interface behavior and even formation. In fact, Cheng et al. proposed that NiO electrostatics leads to a certain amount of perovskite precursor ions (i.e., methylammonium and iodide), remaining attached on the surface and ruining the interface quality.^[257] The high defect concentration at the interface, proved by photothermal deflection spectroscopy and photoluminescence (PL), was reduced by UV light soaking or the introduction of *n*-butylamine monolayer,

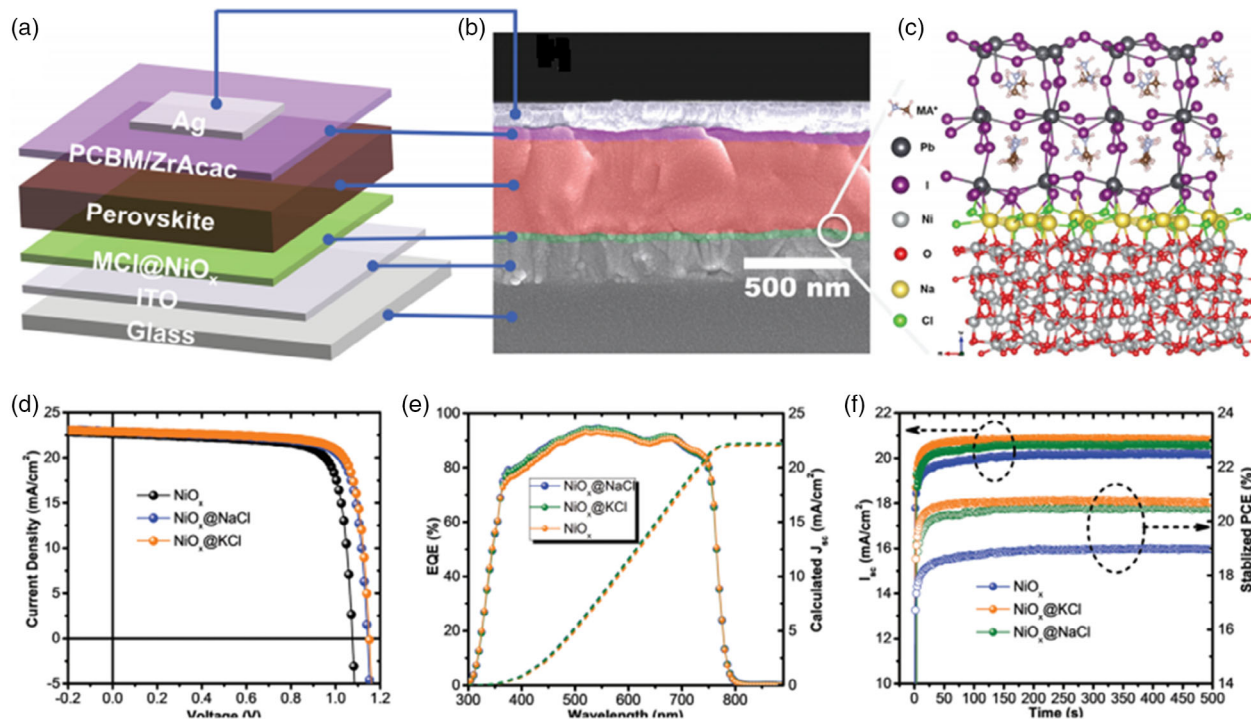


Figure 14. a) Schematic diagram of the device structure of PSCs. Pristine or alkali chlorides (MCl)-modified NiO_x were used as HTLs. b) Cross-section scanning electron microscopy (SEM) image of a typical PSC with CsFAMA perovskite and sodium chloride (NaCl)-modified NiO_x HTLs. c) A supercell illustrating the structural details in the perovskite/NaCl/ NiO_x HTL interface. d) Current–voltage characteristics of the optimal CsFAMA PSCs with pristine or alkali chlorides (MCl)-modified NiO_x HTLs. e) External quantum efficiency (EQE) spectra of the corresponding PSCs in (d). f) Stabilized PCE of the corresponding PSCs in (d). Reproduced with permission.^[358] Copyright 2019, Wiley-VCH.

which reduced the effect of the NiO dipole on the formation of perovskite. The detrimental interaction of NiO with perovskite ions has been further highlighted by Di Girolamo et al., who reported the occurrence of noncapacitive hysteresis in the dark for NiO-based p-i-n PSCs.^[258] The noncapacitive hysteresis has been proposed to arise from bias-induced reactions (e.g., electrochemical reactions such as iodide oxidation)^[259,260] at the interface between the HTL and perovskite. In fact, by introducing a solution-processed MgO interlayer, the hysteresis vanished and the devices became electrically more stable. Similarly, Zhang et al. stabilized the p-type interface with the introduction of 5-aminovaleric acid (5-AVA, bonded to NiO through the carboxylic functional group).^[261]

Doping in NiO has proved to be a successful strategy to increase the performance of PSCs. For example, Cu-doped NiO has shown improvement in PCE up to 15.4% (from 11.16% for pristine NiO counterparts).^[134] In another report, low-temperature-processed Cu:NiO showed an even higher efficiency of the devices of 17%.^[135] Copper doping has been later implemented in NiO NPs^[262] for planar PSCs and also for the best-performing NiO-based mesoscopic PSCs to date (with efficiency approaching 20%).^[136] Similarly, alkaline doping in NiO has also enhanced device performance,^[149] primarily due to a downward shift of the VBM going from -5.04 eV for the pristine NiO to -5.19 eV with Mg and -5.29 eV with Ca and -5.34 eV with Sr (and barium leading to -5.18 eV), with all the cations apparently substituting Ni, as suggested by the lattice expansion from XRD. At the same time, the conductivity was increased due to enhanced hole mobility. The best device performances were obtained using Sr-doped NiO, with PCE attaining 19.49% and V_{OC} of 1.14 V, in line with the results from Zhang et al.^[263] Li et al.^[150] demonstrated that Mg-doped NiO improves the FF of PSCs from 70% for NiO to 79% when 8% of Mg is introduced via a cosputtering route. Nonetheless, an excessive concentration ($>10\%$ atomic ratio), worsened the charge extraction, as demonstrated low FF of 64% when 12% of Mg is introduced.

4.3.5. CuO/Cu₂O in PSCs

PSCs with copper oxides as efficient HTLs have also been demonstrated with enhanced performance. Wang et al.^[264] and Hossain et al.^[265] conducted theoretical studies on planar PSCs based on MAPbI_{3-x}Cl_x or MAPbI₃ as the active layer and Cu₂O as the HTL, using a solar cell simulation program (wxAMPS). The influence of Cu₂O thickness, hole mobility, and midgap defects on the device performance was extensively investigated, leading to the conclusion that 10–50 nm Cu₂O films could successfully be used as HTLs in PSCs achieving a PCE close to 24%.

Ding's group^[266] reported a facile low-temperature Cu₂O film formation via the reaction of CuI films in NaOH solution, whereas CuO films were formed by heating Cu₂O in air. PSCs with Cu₂O and CuO HTLs showed high PCE values of 13.35% and 12.16%, respectively, attributed to the well-matched energy levels between the copper oxide HTLs and the perovskite absorber, leading to reduced energy loss. Cu₂O and CuO substrates also improved the film quality of MAPbI₃ deposited on top of them, resulting in favorable hole transport as well as improved device stability.

Cu₂O thin films have also been deposited by successive ionic layer adsorption and reaction (SILAR),^[267] reactive magnetron sputtering,^[268] and electrodeposition^[269] methods and used as HTLs in PSCs. Although the PCE values of 8.23%, 8.93%, and 9.64% were poor, it is shown that Cu₂O is a promising HTM, which could effectively replace the widely used, but also expensive, Spiro-OMeTAD, offering high hole extraction ability, appropriate energy levels for charge carrier separation, and good pin-hole free film formation of the perovskite absorber deposited on top. A high PCE of 17.1% was reported by Sun and coworkers^[270] for inverted planar heterojunction PSCs based on MAPbI₃ using a solution-processed CuO_x as the HTL. The same group reported an even higher PCE of $\approx 19\%$ in MAPbI_{3-x}Cl_x CuO_x PSCs.^[271] Interestingly, the oxidation of Cu(acac)₂ was observed after a UV-ozone treatment, forming CuO_x films of high transparency and a large W_F , leading to beneficial energy-level alignment at the CuO_x/perovskite interface and thus improved hole extraction and enhanced device performance.

In a similar study, Yu et al.^[272] fabricated efficient PSCs using a solution-processed CuO_x HTL, followed by UV-ozone, exhibiting a PCE of 17.34%, proper surface properties of the HTL, and a good ohmic contact between the perovskite absorber and the CuO_x film, resulting in reduced recombination losses. In addition, the CuO_x-based device showed good stability in ambient air. Recently, Guo et al.^[273] proposed the use of an organic-inorganic HTL consisting of conjugated polymer FBT-Th4 and CuO_x in PSCs. It was found that the FBT-Th4/CuO_x HTL facilitated hole extraction, resulting in an enhanced PCE value of 18.85%, whereas it also enhanced long-term device stability due to successfully blocking moisture penetration into the perovskite layer.

5. Graphene Oxide and Reduced Graphene Oxide

5.1. Electronic Properties

Graphene oxide (GO) has gained large interest for application in solar cells among other optoelectronic devices. It is an atomically thin, 2D framework of carbon atoms. These mutable sp²–sp³-bonded carbon atoms are draped with oxygen functional groups on the basal plane and edges.^[274] This arrangement results in unique optical and electrical properties, that is a complex reciprocation of the size, shape, and fraction of sp² and sp³ hybridized carbon atoms (Figure 15).^[275]

The idealized structure of GO consists of the in-contact hexagonal σ framework of the carbon lattice that can be obtained by controlled temperature and manufacturing conditions.^[276] Since its reconsideration from 2004, the elucidation of structural and electronic properties of GO was the key research area for graphene and its derivatives, which have been revolutionized with the advancement in atomic scale fabrication and characterizations.^[277] Despite its higher electrical conductivity, graphene lacks the semiconducting features of field-effect transistors and resonant tunneling diodes, hindering its way to potential future electronic devices.^[278] However, its oxidized variant (GO, rGO) offers itself to be used as transistors and Schottky diodes with isolated conductive regions and barrier layers, explicitly reliant on the degree of the oxidation and manufacturing

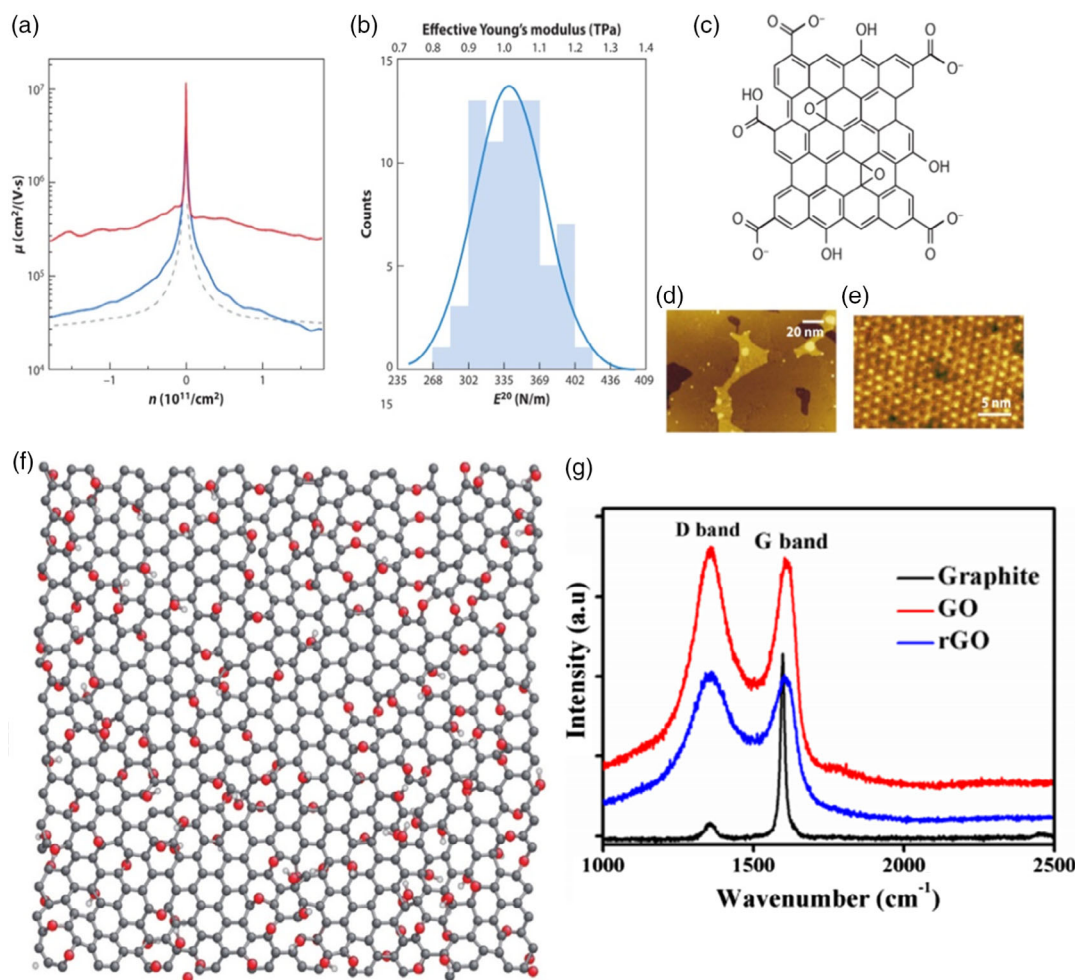


Figure 15. a) Charge mobility of a suspended graphene device as a function of carrier density. Reproduced with permission.^[286] Copyright 2008, Elsevier. b) Elastic stiffness and distribution of graphene film on a silicon oxide cavity. Reproduced with permission.^[287] Copyright 2008, AAAS. c) Chemical structure of GO. Reproduced with permission.^[288] Copyright 2012, American Chemical Society. d,e) Scanning tunneling microscopy (STM) topographs of epitaxial graphene on silicon carbide (SiC). Scale bar in (e) is 5 nm. Reproduced with permission.^[289] Copyright 2007, Elsevier. f) Morphology of GO sheets (oxygen concentration is 20%). g) Measured Raman spectra of graphite, GO, and rGO. Reproduced with permission.^[236] Copyright 2015, American Institute of Physics.

process.^[279] These sp^3 covalent-bonded oxygenated functional groups on basal planes and edges (hydroxyl, epoxy, carboxyl, carbonyl, lactone, phenol, and quinone)^[280] induce stoichiometric inhomogeneities increasing to surface defects, residual defects, and Stone–Wales, defects resulting in loss of electrical conductivity and carrier mobility.^[275] However, it is also beneficial to tune the physicochemical properties rendered from hydrophilicity and fine dispersibility in many solvents, making it applicable to be used as cost-effective transparent conducting electrodes that can be deposited by common methods.

The nonuniformity in the electronically hybrid GO due to the presence of the sp^2 cluster (conducting π states) and sp^3 -bonded C–O framework (nonconducting σ states) has been identified by nuclear magnetic resonance (NMR),^[276] atomic force microscope infrared spectroscopy (AFM-IR),^[281] high-resolution transmission electron microscopy (HRTEM),^[282] PL,^[283] tunneling electron microscopy (TEM), and Raman

spectroscopy.^[275] Even though extensive efforts have been conducted to determine the structure, a precise understanding of GO structural parameters remains ambiguous due to inherent nonstoichiometric arrangements, the mixture of chaotic sp^2 , sp^3 framework, and concealed atomic assembly due to the presence of surface impurities like airborne oxidative moieties (Figure 15).^[236,284–289]

Over the years some conflicting models were proposed for the structural considerations (see a study by Chen^[279] and studies therein). Gao et al. suggested the complete structure of GO having a five-to-six-membered ring in the basal plane as well as the decorated functionalities at the edges.^[284] Perumbilavil et al. demonstrated that in the Raman spectra of graphite, GO, and rGO, the G band is common for all sp^2 carbon forms, and it arises from the C–C bond stretch (Figure 15g). This band is formed from first-order Raman scattering.^[286] Liang et al. represented the elucidation of the complete band structure of GO by

detailed analysis of PL, UV-vis, and Raman spectroscopy, suggesting an approximate value of 3.54 eV for as-prepared GO, which is decreased during the reduction process.^[285]

Recently, Feicht and Eigler explained several types of defects in GO, for example, rearrangement defects, transient defects, vacancy defects, on-plane functionalization, and in-plane lattice defects.^[177] According to them, Raman spectroscopy is the best analytical technique among others to probe and differentiate the various kinds of possible defects.^[276] Liu et al. determined the spatial distribution of the sp^3 - sp^2 , carbon-oxygen framework with the resolution at the molecular level by combined AFM-IR mapping and presented an updated structural model for GO that is very useful to determine morphology, chemical composition, and type and position of C—O bonding in the GO layer.^[281]

5.2. GO and rGO in OSCs

GO and its derivatives are wide-bandgap, high- W_F materials suitable to make an ohmic contact with the organic absorber layer and hence are successful HTLs in OSCs (Table 3).^[290] Interestingly, GO can also be used as a dopant in the photoactive layer. For example, Amollo and coworkers^[291] explored the dual nature of GO as a dopant in the PEDOT:PSS-based HTL and also in the photoactive layer and reported an improvement in PCE up to 120% and 40%, respectively. They attributed this improvement in PCE to an enhanced photocurrent of 18 mA cm^{-2} , which arose from the improved optical absorbance and conductivity of the photoactive layer. They, however, explained that GO synthesized in their work was not beneficial to improve charge transport due to the high sheet resistance of $68 \text{ k}\Omega \text{ sq}^{-1}$, although it effectively blocked electron leakage. Furthermore, the carboxylic edge group of GO induced the formation of an ohmic contact with P3HT, providing a low extraction barrier for holes.

Chen et al. successfully modified GO with noncovalent phosphorylation and compared OSCs using pristine GO, modified GO, and PEDOT:PSS as HTL and various donor-acceptor polymer blends.^[292] Due to enhanced hole extraction efficiency, modified GO shows the highest PCE of 7.85% with V_{OC} 0.71 V, J_{SC} of 16.12 mA cm^{-2} , and a FF of 0.68. A lower leakage current was also observed for modified GO-based OSCs. The use of a phosphate ester group enhanced the W_F of ITO/GO from 4.2 to 4.7 eV, thus improving hole extraction in modified GO-based

OSCs. In a different study, Sun et al.^[293] used a mixture of CuCl_2 and GO as the HTL in OSCs and compared their device performance with pristine GO and PEDOT:PSS as HTLs. They reported a higher PCE for the GO: CuCl_2 -based device (7.68%) than that of the pristine GO HTL-based OSC (7.10%). A similar improvement was also reported for GO and oxygen-deficient MoO_{3-x} bilayer HTL.^[294] The PCE of OSCs using PThBDTP:PC₇₀BM as the photoactive layer increased to 8.5%, higher than a reference device using PEDOT:PSS as the HTL (PCE of 7.85%).

Recently, Cheng and coworkers^[295] used fluorine-functionalized rGO (F-rGO) as the HTL in OSCs and reported PCEs of 8.6% in contrast to pristine GO and PEDOT:PSS-based OSCs with PCEs of 7.8 and 7.9%, respectively. They showed this improvement due to a higher conductivity and W_F of F-rGO HTL. Similarly, Cheng et al.^[296] demonstrated the self-assembled quasi-3D GO: NiO_x composite as a HTL in an inverted OSC. The remarkable improvement in conductivity led to a high PCE of 12.13% (average PCE was 11.45%), which was at that time the highest reported value for inverted OSCs. This improvement was referred to as breaking the vertical conductivity limit of the usual 2D HTL and enhanced carrier extraction properties probed by transient photocurrent decay analysis and impedance spectroscopy. The devices with GO: NiO_x HTLs presented a low leakage current (0.06 vs 0.96 mA cm^{-2}) in comparison with a pristine GO HTL, benefitting the suppression in electron-hole recombination at the HTL/anode interface.

5.3. GOs and rGOs in PSCs

GO is among the successful HTL material in PSCs (Table 4) due to its effective hole extraction, alignment of its VB with that of the perovskite, and cost effectiveness. Jokar et al.^[297] compared the performance of GO, PEDOT:PSS, and rGO as HTLs in PSCs and reported 16% PCE for rGO devices, exceeding PEDOT:PSS and GO counterparts. Interestingly, despite lower PCEs, GO/perovskite interfaces showed superior hole extraction than rGO, as suggested by PL spectra, PL decay, and transient photovoltage decay. The authors suggested that, while the GO interface offers improved hole extraction, hole transport/transfer from GO to ITO substrates was slower than that in rGO, which increases charge recombination and is responsible for the lower performance in GO-based devices. A PCE of 13.5% was also reported in flexible PSCs using rGO HTL.

A solution-processable sulfated GO (sGO):PEDOT:PSS (1:1 ratio) composite was used by Guo and coworkers^[298] as HTL. Notably, the pristine sGO showed a lower PCE of $\approx 9.9\%$ compared with a PEDOT:PSS-based reference device (PCE 11.3%). The optimized ratio of sGO and PEDOT:PSS composite led to a higher PCE $\approx 13.9\%$ due to improvement in hole extraction and improved morphology of the perovskite deposited on top of the composite HTL. In another report,^[299] GO-modified PEDOT:PSS also led to PCE improvement from 11.9% to 15.34% in inverted PSCs. The improvement was attributed to the improved wettability of the HTL film and higher crystallinity of the perovskite film deposited on top of it. GO incorporation also led to an improvement in hole extraction and higher carrier mobility. Similarly, Yu et al.^[256] reported a composite HTL made of PEDOT:PSS and GO that led to high performance

Table 3. PV parameters of OSCs using GO as HTLs.

HTL	Organic absorber	PCE [%]	J_{sc} [mA cm^{-2}]	V_{oc} [V]	FF	Ref.
PEDOT:PSS-GO	P3HT:PCBM	2.80	14.00	0.53	0.38	[291]
GO	PTB7-PC ₇₁ BM	6.03	15.26	0.65	0.61	[292]
GO	PTB7-Th:PC ₇₁ BM	7.10	15.19	0.775	0.60	[293]
Go: CuCl_2	PTB7-Th:PC ₇₁ BM	7.68	15.52	0.785	0.63	[293]
GO	PTB7-Th:PC ₇₁ BM	7.80	15.65	0.776	0.64	[295]
P-GO	PTB7-PC ₇₁ BM	7.85	16.12	0.71	0.68	[292]
GO/ MoO_{3-x}	PThBDTP:PC ₇₁ BM	8.05	12.21	0.97	0.68	[294]
F-rGO	PTB7-Th:PC ₇₁ BM	8.60	16.89	0.786	0.65	[295]
L-GO: NiO_x	PBDB-T:IT-M	11.45	17.81	0.91	0.71	[296]

Table 4. PV parameters of PSCs using GOs as HTLs.

HTL	Perovskite absorber	PCE [%]	J_{sc} [mA cm^{-2}]	V_{oc} [V]	FF	Ref.
GO	MAPbI ₃	13.8	19.5	0.943	0.75	[297]
sGO-PEDOT	MAPbI ₃	13.9	20.4	0.95	0.72	[298]
rGO/CuSCN	MAPbI ₃	14.28	18.21	1.031	0.76	[368]
GO flakes	FA _{0.2} MA _{0.8} Pb(I _{0.8} Br _{0.2}) ₃	14.9	21.00	1.00	0.71	[369]
GO	MAPbI ₃	14.9	21.8	0.898	0.76	[256]
GO-Au NP	MAPbI ₃	14.9	20.2	0.913	0.81	[256]
rGO-BH	MAPbI ₃	15.3	21.8	0.970	0.72	[297]
PEDOT/GO-30	MAPbI ₃	15.34	21.92	0.94	0.75	[299]
rGO-NH ₂	MAPbI ₃	15.9	21.3	0.963	0.78	[297]
rGO	Cs _{0.05} (MA _{0.17} FA _{0.83}) _{0.95} Pb(I _{0.83} Br _{0.17}) ₃	16.28	21.46	1.06	0.72	[302]
rGO-HBS	MAPbI ₃	16.4	22.1	0.961	0.77	[297]
GO	MAPbI ₃	16.5	21.6	1.00	0.76	[301]
GO-MoO _x NP	MAPbI ₃	16.7	21.8	0.99	0.77	[300]
PEDOT:GO	MAPbI _{3-x} Br _x	18.09	21.55	1.02	0.82	[256]

(PCE 18.09%) inverted PSCs. This remarkable performance was due to an optimized HTL that showed higher transmittance, higher electrical conductivity, an aligned W_F with the perovskite absorber, better perovskite crystallinity, and suppression of leakage current than the PEDOT:PSS counterpart.

In another report, Bhosale et al.^[300] conducted the functionalization of GO with NPs of Au and MoO_x. The modified GO HTLs showed improved alignment for hole extraction, as evidenced by Kelvin probe force microscopy and ultraviolet photoelectron spectra measurements and hence a higher V_{OC} . However, the Au:GO HTL (PCE 14.6%) showed an almost identical performance to the GO HTL (PCE 14.4%), despite a faster hole extraction, whereas the MoO_x:GO HTL showed significant improvement in PCE (16.7%). In addition, a lower J_{SC} was obtained for Au:GO HTL (Figure 16). Using transient photoelectric measurements, the authors revealed that the Au NPs led to

hole trapping and their localization inside NPs, leading to rapid charge recombination. In the case of MoO_x:GO HTL, the delocalization of holes and no hole trapping led to rapid CT to ITO, thus leading to a higher J_{SC} and V_{OC} .

Optimization of GO film thickness is a key parameter to improve device performance. This was shown in the work of Yang and coworkers,^[301] where an optimized GO thickness (2 nm) as the HTL demonstrated a low series resistance, high conductivity, and optimum work function. The balanced work function thus led to a hysteresis-free PCE of 16%. Upon systematically increasing the GO thickness to 10 nm, the device performance decreased due to higher series resistance. Similar to optimizing film thickness, surface coverage by GO HTL was also found to be critical in determining device performance. Yin et al.^[302] deposited GO and rGO via a layer-by-layer self-assembly process to control HTL thickness and also

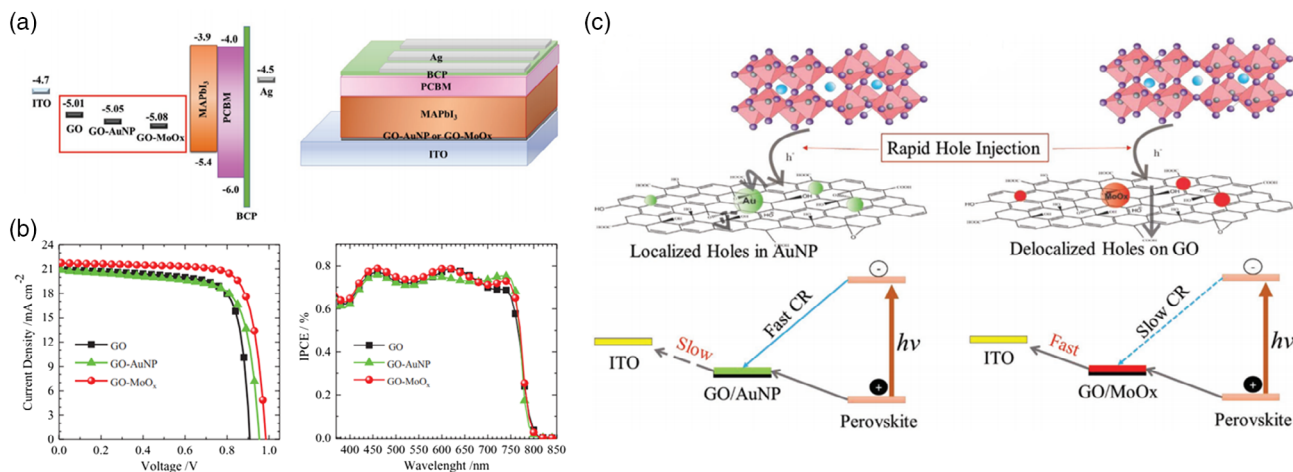


Figure 16. a) The measured energy levels and the PSC structure. b) Current–voltage and EQE curves of PSCs using GO and GO modified with Au and MoO_x NPs. c) A schematic showing hole extraction and hole trapping mechanism in modified GO HTLs. Reproduced with permission.^[300] Copyright 2017, WILEY-VCH.

attain a better surface coverage and showed $\approx 33\%$ improvement in PCE.

6. Other Inorganic HTLs in OSCs

Apart from TMOs, other novel inorganic semiconducting molecular materials such as copper-based semiconductors and TMDs have been used as HTLs in OSCs (Table 5).

6.1. CuI and CuSCN

Copper iodide (CuI) has a high hole mobility of $\approx 1 \text{ cm}^2 \text{ V}^{-1} \text{ s}^{-1}$ and was the first transparent p-type inorganic semiconductor to be successfully used as a HTL in OSCs. Its high transparency and hole mobility combined with its suitable energetics (i.e., a high W_F of $\approx 5.1 \text{ eV}$) rendered it suitable for an inexpensive HTL with low-temperature solution processability. Peng et al.^[303] reported the first application of CuI in OSCs with a PCE of 5.54%, whereas Mohamed et al.^[304] demonstrated improvements in OSCs with a PCE of 3.20% when using a CuI HTL.

More recently, another wide-bandgap p-type semiconductor, namely copper thiocyanate (CuSCN), with a hole mobility of $\approx 0.5 \text{ cm}^2 \text{ V}^{-1} \text{ s}^{-1}$ and a W_F of $\approx 5.2 \text{ eV}$, suitable to match the ionization energy (HOMO) of most organic semiconductors, was reported. CuSCN HTLs have been used in different OSCs (regular and inverted types) with PCEs reaching 8.07% for OSCs based on blends of narrow-bandgap polymer semiconductors with PCBM. CuSCN was also found to be beneficial on regulating the morphology (i.e., grain size) and enhancing the crystallinity and the photoactive underlayer.^[305–307]

To increase its hole conductivity, p-type molecular doping with strong organic electron acceptors such as $C_{60}F_{48}$ and $F_4\text{-TCNQ}$ has been successfully demonstrated.^[308,309] The p-type doped CuSCN layers were used as HTLs in OSCs. Improved PCEs of 6.60% for PCBTBT:PC₇₀BM-based OSCs^[308,309] have been

reported, accompanied by a lower dark current and enhanced shunt and lower series resistance. Enhanced solar cell performance was attributed to the enhanced hole mobility and the facile hole transfer as a result of the Fermi level shift toward the VB of the p-type-doped CuSCN, thus reducing the interfacial energetic mismatch.

6.2. Transition Metal Dichalcogenides (TMDs)

TMDs are a novel family of 2D nanosheets with the chemical form MX_2 (M is the transition metal and X is the chalcogen).^[310,311] Water and/or alcohol solubility and their superior optoelectronic properties make them excellent candidates for charge extraction/transport in OSCs. A plethora of recent reports unambiguously demonstrated that OSCs based on TMDs, such as sulfides and selenides as HTLs and/or ETLs, exhibited superior performance, in terms of both PCE and stability, compared with other used materials.^[310,312,313] Representative examples are discussed in this section.

Copper sulfide (CuS) was initially reported to function as an effective HTL in P3HT:PCBM-based OSCs with a PCE of 2.64%.^[314] Liquid-exfoliated tungsten sulfide (WS_2) was proposed to function as an effective HTL in nonfullerene-based OSCs. High uniformity on ITO, large, tunable, W_F ($\approx 5.2\text{--}5.9 \text{ eV}$, depending on the number of deposited layers), favorable photonic structure, and reduced recombination losses resulted in a superior PCE of 16.50% for PBDB-T-2F:Y6:PC₇₁BM-based OSCs with an exceptional J_{SC} of 26 mA cm^{-2} , thus representing the highest PCE to date for OSCs with 2D charge transport layers.^[315]

As an attractive alternative to WS_2 , molybdenum sulfide (MoS_2) has been used as a highly effective HTL in OSCs. The enhanced interfacial energy-level alignment facilitated exciton dissociation and charge transport, and excellent uniformity of the fabricated organic and perovskite layer on the MoS_2 layer resulted in high PCEs of 8.43% for PBDTTT-C-T:PC₇₀BM-based OSCs.^[316] Figure 17a,b show a schematic diagram illustrating the process of sonication-assisted liquid exfoliation used to prepare MoS_2 and WS_2 suspensions and their work function was determined both experimentally and with DFT calculations.^[315] Figure 17c,d show the OSC architecture used (ITO/ MX_2 (M: Mo or W)/PBDB-T-2F:Y6:PC₇₁BM/PFN-Br/Al) and the EQE curves of the fabricated OSCs for both MoS_2 and WS_2 HTLs.

6.3. CuI and CuSCN as HTLs in PSCs

Recently, copper-based inorganic compounds have emerged as cost-effective alternatives to organic HTLs. This field has been extensively reviewed in recent years and the readers are referred to several specific review papers.^[317,318] Here, some representative examples are summarized and discussed (Table 6).

The incorporation of CuI as a HTL in n-i-p type (i.e., regular) MAPbI₃-based planar PSCs was first reported by Li et al., resulting in a PCE of 17.60%, reduced hysteresis, and outstanding stability, as manifested by a constant PCE over a period of 50 days after storage in the dark.^[319] Saranin et al. later reported the advantageous application of CuI as a HTL in p-i-n-type (inverted) MAPbI₃-based PSCs with a PCE of 14.23%.^[320] Few other reports on CuI as the HTL in MAPbI₃-based PSCs with

Table 5. PV parameters of OSCs using Cu-based and TMDs as HTLs.

HTL	Organic absorber	PCE [%]	J_{SC} [mA cm ⁻²]	V_{OC} [V]	FF	Ref.
CuI	AnE-PVab:PCBM	1.3	2.42	0.82	0.52	[304]
CuI	AnE-PVstat:PCBM	3.2	5.45	0.76	0.63	[304]
CuI	PBDTPD:PCBM	5.54	14.0	0.81	0.50	[303]
CuSCN	PCDTBT:PC ₇₀ BM	6.3	11.8	0.91	0.59	[308]
$C_{60}F_{48}$:CuSCN	PCDTBT:PC ₇₀ BM	6.6	11.5	0.92	0.61	[308]
CuSCN	p-DTS(FBTTh ₂) ₂ :PC ₇₁ BM	6.89	13.9	0.80	0.62	[306]
CuSCN	PDPP-2T-TT:PC ₇₁ BM	7.72	16.3	0.70	0.68	[305]
CuSCN	PBDTPD:PCBM	8.07	12.74	0.92	0.69	[305]
CuSCN	PTB7-Th:PC ₇₀ BM	10.70	21.1	0.80	0.63	[307]
CuS	P3HT:PCBM	2.64	8.38	0.62	0.44	[314]
MoS_2	PBDTTT-C-T:PC ₇₀ BM	8.43	15.69	0.76	0.70	[370]
MoS_2	PBDB-T-SF:IT-4F	12.0	20.0	0.84	0.71	[315]
WS_2	PBDB-T-SF:IT-4F	13.5	20.6	0.88	0.74	[315]
WS_2	PBDB-T-SF:Y6	15.8	25.9	0.84	0.73	[315]
WS_2	PBDB-T-SF:Y6:PC ₇₁ BM	17.0	26.0	0.84	0.78	[315]

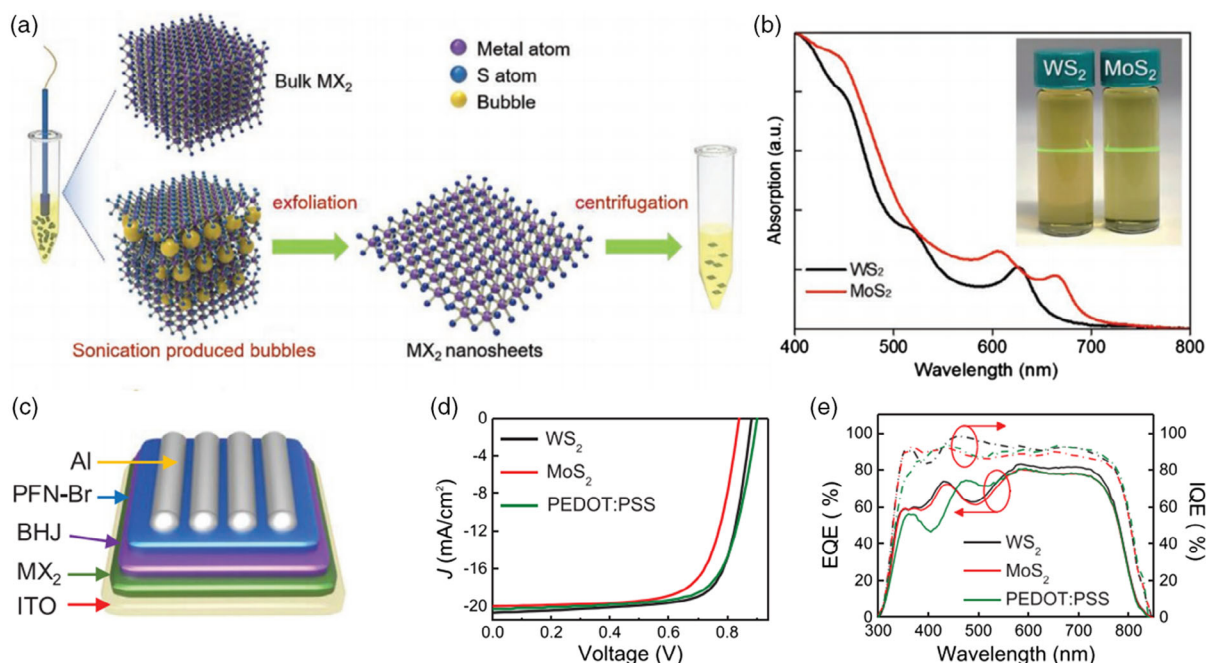


Figure 17. a) Schematic illustrating the process of sonication-assisted liquid exfoliation used to prepare MoS₂ and WS₂ suspensions. b) The UV-vis absorption spectra of MoS₂ and WS₂. c) Schematic diagram of the OSC architecture used (ITO/MX₂ (M: Mo or W)/BHJ)/PFN-Br/Al. d) J-V characteristics taken under 1 sun simulated light and e) EQE curves of OSCs based on a PBDB-T-2F:Y₆:PC₇₁BM active layer for different HTLs. Reproduced with permission.^[315] Copyright 2019, WILEY-VCH.

Table 6. PV parameters of PSCs using Cu-based and TMDs as HTLs.

HTL	Perovskite absorber	PCE [%]	J_{sc} [mA cm ⁻²]	V_{oc} [V]	FF	Ref.
CuI	MAPbI ₃	11.82	17.57	0.95	0.71	[320]
CuI-PEDOT:PSS	MAPbI ₃	13.5	19.8	0.91	0.75	[322]
CuI	MAPbI ₃	13.58	21.06	1.04	0.62	[326]
CuI	MAPbI ₃	14.7	20.9	1.04	0.68	[323]
CuI-NiO	MAPbI ₃	15.26	20.60	1.07	0.69	[320]
CuSCN	MAPbI ₃	11.1	19.0	0.92	0.62	[309]
F4TCNQ-CuSCN	MAPbI ₃	15	20.4	0.99	0.72	[309]
CuSCN	MAPbI ₃	16.6	21.9	1.0	0.76	[33]
CuSCN/NH ₃ (aq)	MAPbI ₃	17.5	22.7	1.1	0.71	[307]
CuSCN	CsFAMAPbI _{3-x} Br _x	20.3	23.4	1.10	0.77	[327]
CuSCN/rGO	CsFAMAPbI _{3-x} Br _x	20.4	23.2	1.11	0.78	[327]
WS ₂	MAPbI _{3-x} Cl _x	9.53	14.9	0.96	0.67	[328]
WS ₂	MAPbI _{3-x} Cl _x	15	21.2	0.97	0.73	[323]
MoS ₂	MAPbI ₃	6.01	12.6	0.84	0.57	[331]
MoS ₂	MAPbI _{3-x} Cl _x	9.93	15.9	0.82	0.64	[328]
MoS ₂	MAPbI ₃	13.3	21.5	0.93	0.68	[324]
MoS ₂	MAPbI _{3-x} Cl _x	14.35	20.94	0.88	0.78	[323]
MoS ₂	MAPbI ₃	14.7	21.2	0.95	0.73	[333]

PCEs of 14.7%^[321] and 13.5%^[322] have also appeared recently in the literature. Wang et al.^[323] adopted a simple solid-gas reaction method to deposit compact and uniform CuI films. They,

particularly, exposed a Cu film fabricated via thermal evaporation to iodine vapors and applied it as a HTL in inverted planar PSCs. The optimized devices exhibited PCEs of 14.7%, derived from a V_{oc} of 1.04 V, a J_{sc} of 20.9 mA cm⁻², and a FF of 0.68. Moreover, these devices exhibited good long-term stability at ambient atmosphere, which was mainly attributed to the hydrophobicity of CuI HTL.

Since CuI possesses several desired characteristics, such as high hole mobility combined with high transparency, good chemical stability, and low production cost,^[324] and it stimulated increasing interest as alternative HTLs for efficient and stable PSCs. Recently, Uthayaraj et al.^[325] fabricated highly efficient PSCs made in air with either CuI or Spiro-OMeTAD as HTLs. A simple and novel pressing method was used for incorporating a CuI powder layer between the perovskite layer and Pt top contact to fabricate devices with CuI. The average J_{sc} of the CuI devices was over 24 mA cm⁻², which was marginally higher than that of Spiro-OMeTAD devices. This was attributed to the high hole -mobility of CuI, which minimizes the electron-hole recombination. However, the average PCE of the CuI devices was lower than that of Spiro-OMeTAD ones due to slightly lower V_{oc} and FF. This was due to the surface roughness of CuI powder. However, optimized devices with solvent-free powder-pressed CuI as the HTL showed a promising efficiency of over 8.0% when fabricated in an open environment with CuI.

One of the successful reports on PSCs, incorporating CuI as the HTL, has been the work of Chen et al.^[326] In this report, a low-cost, solution-processed method has been used to prepare hydrophobic CuI films, that served as the HTLs in inverted planar PSCs with the structure of FTO/CuI or PEDOT:PSS/

MAPbI₃/PCBM/Al. A PCE of 13.58% was achieved using CuI as the HTL, higher than that of the reference device using PEDOT:PSS with a PCE of 13.28%. Added to the merits, CuI-based devices exhibited a high long-term stability upon air exposure. Sun et al.^[270] exceeded the work of Tian et al., using a different, one-step, fast deposition–crystallization method for the perovskite absorber, and managed to increase the PCE to 16.8%. Moreover, the optimized PSCs based on the CuI HTL exhibited excellent air stability, retaining more than 90% of the PCE for 300 h of illumination.

CuSCN is another successful inorganic HTL PSC due to its wide bandgap (>3.4 eV), excellent hole extraction/transport properties, and high optical transparency. Wijeyasinghe et al.^[307] reported an ultrathin CuSCN layer (3–5 nm) processed at a low temperature, i.e., 100 °C. Their CuSCN films revealed a five-fold higher hole mobility than conventionally reported CuSCN films, with a maximum value reaching 0.1 cm² V^{−1} s^{−1}. When used as a HTL in PSCs (ITO/PEDOT:PSS/CuSCN/MAPbI₃/PCBM/LiF/Ag), a remarkable PCE of 17.5% was shown with negligible hysteresis. Ye et al.^[33] used CuSCN in p–i–n planar PSCs. They used a fast crystallization method to deposit the perovskite layer, which led to a reduced surface roughness and a smaller contact resistance at the CuSCN/perovskite interface. They reported a champion PCE of 16.6% (average PCE of 15.6%) in their devices. Jin et al.^[309] reported molecular doping in CuSCN by 2,3,5,6-tetrafluoro-7,8,8-tetracyanoquinodimethane (F4TCNQ) and showed around 35% enhancement in the PV performance of their devices. They showed a more efficient charge transport and less carrier recombination in the F4TCNQ-doped CuSCN-based PSCs, which a PCE of over 15% and negligible hysteresis.

In fact CuSCN as the HTL has led to one of the highest PCEs, exceeding 20% in planar PSCs n–i–p PSCs.^[327] A fast solvent removal technique is used to deposit a dense conformal thin film of CuSCN on top of the perovskite (Figure 18). When compared with a Spiro-OMeTAD reference device (PCE of ≈20%), the CuSCN HTL showed a faster hole extraction from the perovskite photoactive layer (Figure 18c,d). It was however found that the CuSCN reacts with Au electrode (and not with perovskite layer, as often suggested in literature). The authors introduced a thin layer of rGO to overcome the reactivity of the CuSCN/Au interface, which not only slightly improved PCE, but also the operational stability of these devices. Notably, these devices used all-inorganic charge extraction layers (TiO₂ as ETL and CuSCN-rGO as HTL), thus paving the way toward high-efficiency stable PSCs.

6.4. TMDs as HTLs in PSCs

Liquid-exfoliated WS₂ was proposed to function as an effective HTL in PSCs. Kim et al.^[328] applied smooth and uniform WS₂ films as HTLs in PSCs using the chemical vapor deposition (CVD) method. The corresponding device exhibited a PCE value of 8.02%, which was inferior to that of the reference device with the PEDOT:PSS HTL, due to the lower value of V_{OC}. Similar results were also obtained from the same authors for MoS₂-based PSCs with a PCE of 9.53%, suggesting that TMDs are promising

materials for HTLs in PSCs. The successful use of a water-soluble WS₂ film as the HTL in high-efficiency PSCs was also demonstrated by Huang et al.^[323] The fabricated devices reached a PCE value of 15%. Moreover, the stability of the WS₂-based PSC was significantly improved, maintaining 72% of the initial efficiency after 56 days.

As an attractive alternative to WS₂, MoS₂ has been used as a highly effective HTL in PSCs. Capasso et al.^[324] inserted MoS₂ flakes between Spiro-MeOTAD HTL and the Au electrode, demonstrating PSCs with a PCE of 13.3%. The stability of the MoS₂-based device showed significant improvement, maintaining 93% of the initial efficiency after 550 h. On the contrary, the reference cell without the MoS₂ layer degraded much faster with the initial PCE value decreasing 34% over the same period. Kakavelakis et al.^[329] investigated the stability of planar inverted PSCs under illumination conditions in ambient air, introducing MoS₂ nanoflakes between the PTAA HTL and the perovskite absorber. It was demonstrated that MoS₂ acted as a protecting layer for the perovskite, preventing water molecule penetration, along with the migration of indium ions from the ITO electrode to the perovskite film. Therefore, encapsulated PSCs based on the MoS₂ interlayer exhibited a high stability, retaining 80% of the initial PCE value (T₈₀) after 568 h of continuous operation. More recently, Kohnepoushi et al.^[330] studied, via device simulation, the impact of MoS₂ film thickness on the design of low-cost, stable, and highly efficient PSCs. Optimum thickness not only of MoS₂, but also of perovskite and ETL films, as well as the selection of aluminum or silver electrodes, showed the potential to achieve PCE beyond 20%.

Dasgupta et al.^[331] applied a centrifugally cast thin-film formation technique to grow homogeneous MoS₂ thin films through a liquid-based exfoliation method. These thin films have been introduced as HTLs in PSCs. They observed that the band edges of MoS₂ formed a type-II band alignment with the perovskite absorber (MAPbI₃), especially when the 2D material was subjected to ozone treatment. p–i–n heterojunction planar PSCs with the thin film of 2H-MoS₂ showed good device characteristics with a small series resistance and a large shunt resistance. Moreover, Peng et al.^[332] demonstrated that atomically thin MoS₂ films exhibit strong light-matter interaction, large optical conductivity, and high electron mobility, hence being highly promising materials for PSCs. By creating sulfur vacancies in MoS₂ using mild plasma treatment, they enabled the formation of a defect-free heterostructure geometry, comprising MoS₂ and MAPbI₃ perovskite for ultrafast hole transfer from MAPbI₃ to MoS₂, following photoexcitation. Furthermore, Wang et al.^[333] demonstrated that MoS₂ nanoflakes can be successfully applied as HTLs in inverted (p–i–n) PSCs. These nanoflakes were blended within the PEDOT:PSS to form a hybrid HTL. The modified devices simultaneously exhibited significant improvement in the PCE and stability. Compared with the reference device with PEDOT:PSS, the efficiency enhancement of MoS₂-incorporated devices was more than 18%, attributed to reduced recombination at the interfaces (absolute PCE as 14.7%), with a significantly lower-electrode polarization and hysteresis. The composite HTL-based devices also exhibited high device stability, retaining more than 95% of the initial PCE even after 4 weeks. These results demonstrate the potential of 2D TMDs for successful application as HTLs in PSCs.

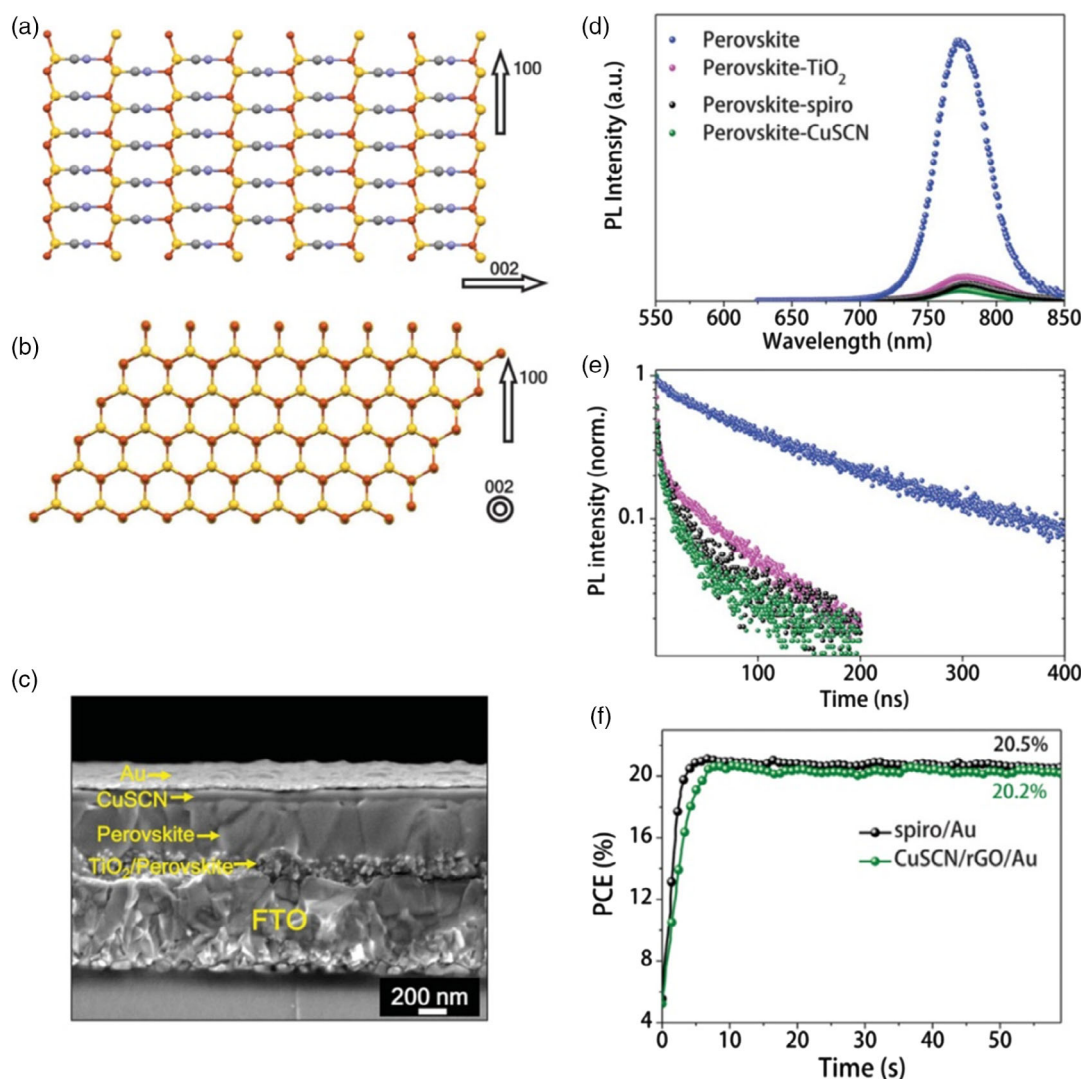


Figure 18. a,b) Preferential out-of-plane orientation of CuSCN (the in-plane orientation rotated by 90°). Color code: red, copper atoms; yellow, sulfur atoms; gray, carbon atoms; blue, nitrogen atoms. c) SEM cross-sectional view of the PSC using CuSCN-rGO as HTL. d,e) Steady-state and time-resolved PL spectra of the perovskite film on various substrates, evidencing efficient charge extraction for CuSCN-rGO interface. f) A stabilized PCE from the maximum power point tracking of a champion device and a control device. Reproduced with permission.^[327] Copyright 2017, AAAS.

7. HTL Layers Toward Operational Stability in OSCs and PSCs

7.1. Stability of OSCs

Apart from improving the PCE of OSCs when incorporated as HTLs, TMOs also have the potential to significantly improve their longevity and stability. In regular OSCs with the HTM deposited underneath the semiconductor blend, the interface between the organic absorber and the front contact has been reported to play a major role in device stability. Besides the reduction in hole extraction barrier, improved physical contact and altered surface energy of the underneath TMO facilitate the formation of compact, pinhole-free photoactive layers with improved morphology and crystallinity.^[164] Contrary to highly acidic PEDOT:PSS which has been reported to cause severe

degradation not only in regular but also in inverted OSCs,^[73] where its phase separation to PEDOT-rich and PSS-rich phases results in more rapid decomposition under high humidity conditions, these materials are chemically and thermally robust while also preventing moisture penetration into the active layers in the inverted structures. Therefore, TMOs have been widely applied as buffer layers to protect the photoactive blend from undesired degradation.

Nevertheless, in some cases, the application of TMOs, especially MoO₃, has been proven to be detrimental for device longevity. Results indicated that inverted OSCs using a combination of PEDOT:PSS/MoO₃ for the HTL showed an even higher degradation than OSCs using pristine PEDOT:PSS, indicating possible chemical interaction between MoO₃ and PEDOT:PSS. In a detailed study by Hermerschmidt et al.,^[334] the stability of OSCs was investigated following the ISOS-D-2 protocol.^[335]

Herein, the devices were kept in the dark at 65 °C with a controlled humidity of $\approx 45\%$ for several hours. Using a range of thiophene-based photoactive materials (P3HT, PTB7, and DPPTT blended with PC₇₀BM), they investigated two interfaces, ITO/ZnO/photoactive layer and photoactive layer/HTL/

Ag. They concluded that P3HT:PC₇₀BM/MoO₃ is the main origin of the degradation of inverted OSCs, although they found that the MoO₃/Ag interface also contributed to device instability (Figure 19). At an elevated heat test, this degradation became more intense. Several studies have reported how the doping

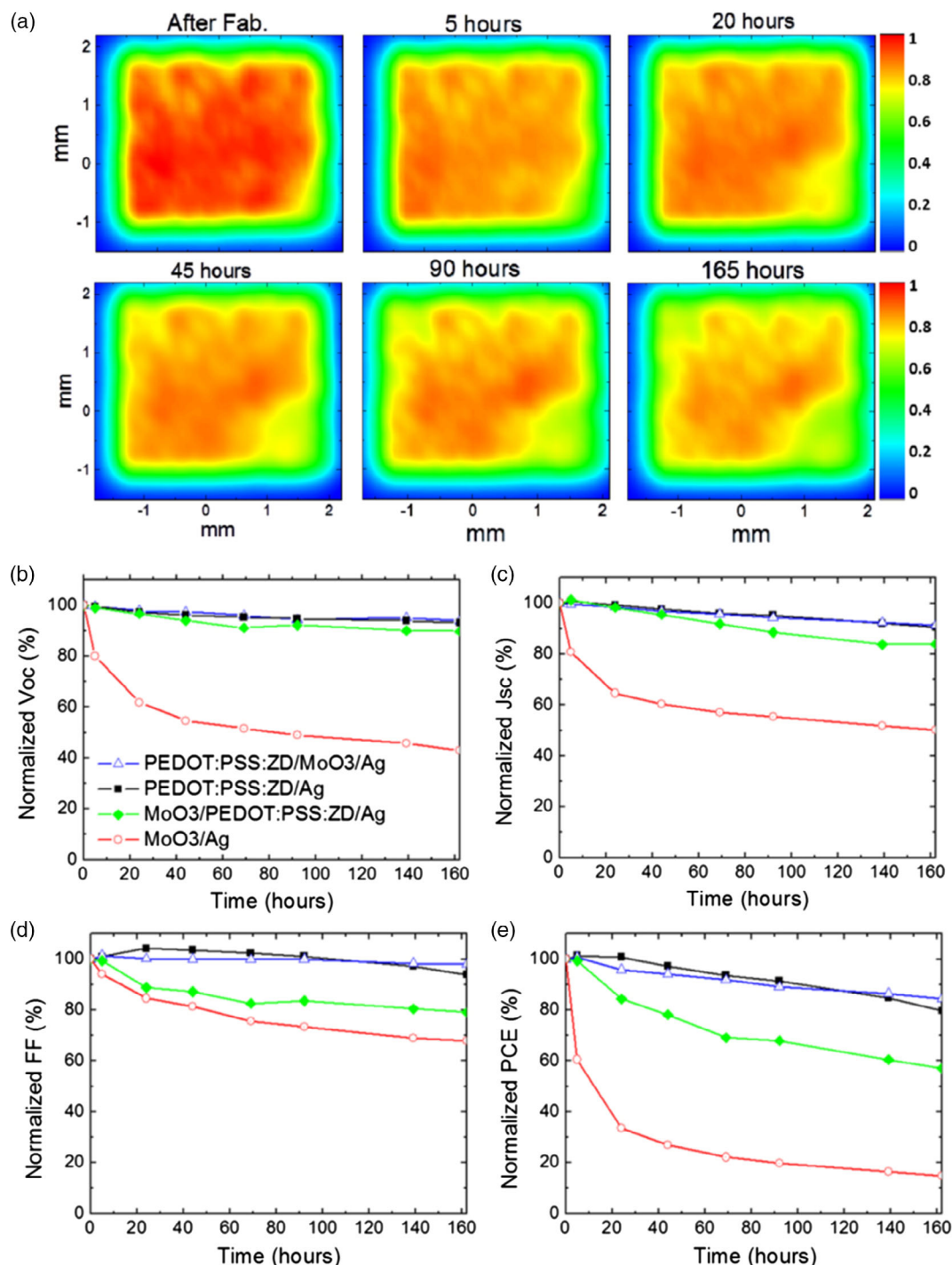


Figure 19. a) Normalized photocurrent maps of inverted nonencapsulated OSCs with MoO₃ as the HTL and P3HT:PC₇₀BM blend as the photoactive layer. The devices are subjected to a heat test at 65 °C for a period of over 165 h. b) V_{OC} , c) J_{SC} , d) FF, and e) PCE versus time of OSCs using different top electrode configurations. Reproduced with permission.^[334] Copyright 2017, American Chemical Society.

of different metal oxides (MoO_3) with Cs can significantly affect their conductive behavior, electron transfer, and blocking properties and also their stability.^[336–338]

Moreover, Pan et al.^[339] demonstrated a MoO_3 :Au coevaporation composite film with a weight ratio of 70:30% (MoO_3 :Au), that can be effectively applied to OSCs to enable better stability than the reference device based on PEDOT:PSS. The MoO_3 :Au composite film was found to improve the surface properties of the ITO electrode, which became smoother upon the deposition of the former, hence increasing the shunt resistance and improving the FF and efficiency of the fabricated devices. The air stability of OSCs using different HTLs (PEDOT:PSS, MoO_3 , and MoO_3 :Au) was investigated and revealed that the MoO_3 :Au composite layer significantly enhanced the device stability with shelf lifetime improved by a factor of 40 and 3 compared with PEDOT:PSS and MoO_3 HTLs, respectively. Girotto et al.^[340] reported the application of sol-gel-based-synthesized MoO_3 thin films as HTLs for all solution-processed OSCs. Their solution-based MoO_3 films (s- MoO_3) were compared with either PEDOT:PSS or thermally evaporated MoO_3 (e- MoO_3) ones regarding the device performance and operational stability. The device shelf lifetime experiments revealed enhanced overall stability when using either thermal-evaporated (e- MoO_3) or solution-processed (s- MoO_3) HTLs compared with those using PEDOT:PSS. Cao and coworkers managed to fabricate stable OSCs with the structure of ITO/HTL/donor/acceptor/cathode using a thin layer

(5 nm) of MoO_3 doped with copper phthalocyanine (CuPc) as the HTL and CuPc/C60 as the organic absorber.^[341] The surface morphology of the HTL played a decisive role in improving the device stability.

Besides MoO_3 , WO_3 has also been found to play an important role in improving OSC stability. Guillaud et al.^[342] developed a solution-processed annealing-free method to deposit WO_3 films, that have shown good performance when used as HTLs in OSCs. In a fully optimized structure, an average PCE of 3.5% was achieved, which was comparable with devices with vacuum-deposited TMOs. More importantly, they demonstrated stable and easily fabricated sol-gel-processed oxides holding the promise for industrial roll-to-roll production on flexible substrates. In a similar manner, Stubhan et al. managed to obtain an improved overall performance in inverted OSCs when using low-temperature postannealed solution-based WO_3 as HTL instead of the commonly used PEDOT:PSS.^[343]

In a different approach, Kim et al.^[344] developed PEDOT:PSS-free OSCs based on mixed electrodes composed of WO_3 and indium oxide (In_2O_3). The resultant composite films (termed IWO) acted as the device-mixed electrodes, protecting buffers and HTLs simultaneously (Figure 20a–d). Through cosputtering and rapid thermal annealing (RTA) of the two oxides in the mixture, they were able to deposit films with a sheet resistance of $17 \text{ Ohm square}^{-1}$ and a remarkable transmittance of 90.32%, having also a high W_F of 4.83 eV. OSCs fabricated on an IWO

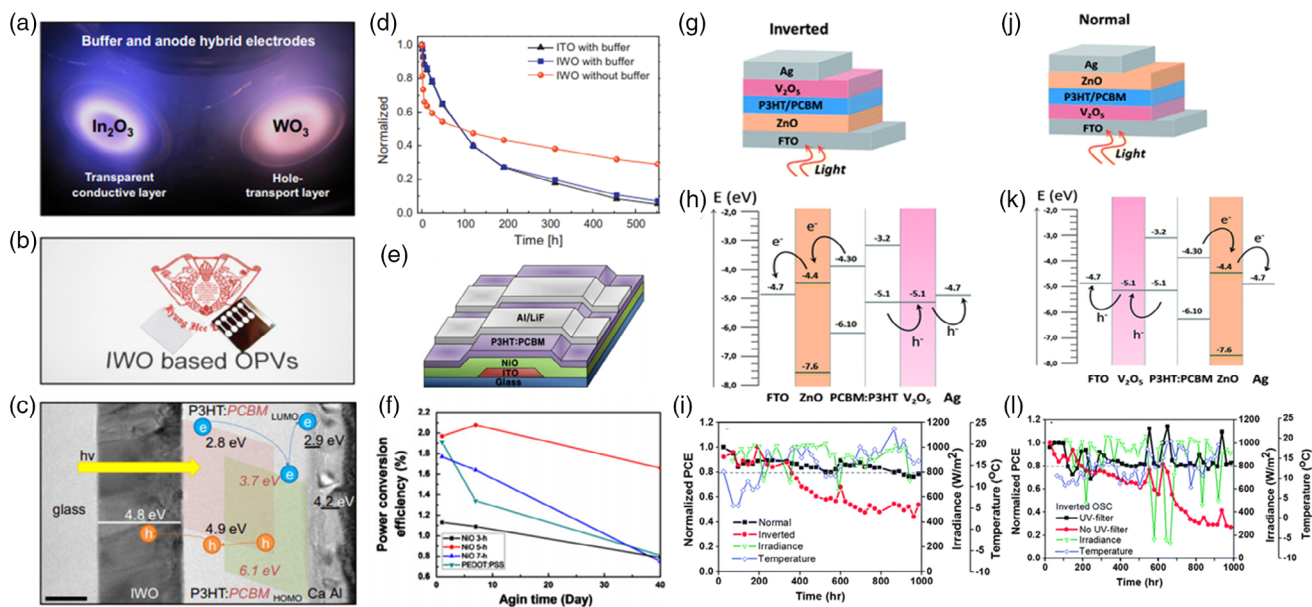


Figure 20. a) Cosputtering of a WO_3 and a transparent conducting indium oxide (In_2O_3) layer to form IWO thin films for the all-in-one (contact + HTL) electrode for OSCs. b) An IWO thin film (on a glass substrate) and IWO-based OSC device. c) The energy-level diagrams for different materials used in the device fabrication process. d) Stability of a PEDOT:PSS-free OSC fabricated on a buffer and anode-integrated IWO electrode. Reproduced with permission.^[344] Copyright 2013, Elsevier. e) The OSC architecture and f) the stability study of NiO-based devices. Reproduced with permission.^[189] Copyright 2013, Elsevier. Schematic representation of the g) inverted and j) regular configuration of OSCs containing water-based, solution-processed V_2O_5 as the HTL. Normal configuration: glass/FTO/ V_2O_5 /P3HT:PCBM/ ZnO /Ag. Inverted configuration: glass/FTO/ ZnO /P3HT:PCBM/ V_2O_5 /Ag. The band energy diagram for the h) inverted- and the k) regular-configuration OSCs. Outdoor stability analysis of sealed OSCs containing water-based, solution-processed V_2O_5 as the HTL. A comparison of the normalized PCE response: i) normal configuration versus inverted configuration (both without the UV filter), l) with the UV filter versus without the UV filter (both in the inverted configuration). The cells were analyzed outdoors in Barcelona, Spain (41.30° N , 2.09° W). The PCE values were calculated using the maximum irradiance level per day. Average temperatures: $10\text{--}15^\circ \text{ C}$ (day) and $5\text{--}7^\circ \text{ C}$ (night). Average relative humidity: 70%. Reproduced with permission.^[347] Copyright 2013, the Royal Society of Chemistry.

electrode exhibited PCE values up to 2.87% with highly improved long-term stability, hence highlighting the potential of TMO-based materials to act as effective electrodes and HTLs simultaneously.

Several other TMOs have shown improvements in OSCs lifetime when used as HTLs in these devices. Liu et al.^[215] demonstrated a remarkable improvement in cell lifetime when replacing PEDOT:PSS with NiO (Figure 20e,f). The improvement was related to the increased oxygen concentration ratio of the NiO structure. Park et al.^[345] reported the beneficial application of p-type NiO thin films with a resistivity of $2.7 \times 10^{-2} \Omega \text{ cm}$ deposited by magnetron sputtering on the stability of OSCs. The insertion of a 5 nm-thick NiO HTL resulted in a PCE of 2.87%, which was comparable with that obtained with PEDOT:PSS. However, the measured lifetime of OSCs adopting the NiO layer was three times higher than that of the PEDOT:PSS-containing devices. Similarly, Wong et al.^[346] demonstrated that OSCs incorporating solution-based NiO HTLs show promising enhancements in device photocurrent and stability. The impact of parasitic shunt and series resistances on both the performance and ambient degradation of these devices was thoroughly investigated. The results showed that charge extraction was predominantly affected by degradation via a decrease in carrier mobility and increased trapping/recombination, revealing the physical mechanism behind the degradation observed in these cells. NiO-based devices, however, sustained their initial performance for a longer time compared with the PEDOT:PSS-containing ones.

Terán-Escobar and coworkers demonstrated an extensive study on OSCs with either the regular or the inverted configuration using solution-processed layered vanadium pentoxide hydrate as the HTL (Figure 20g–l).^[347] V_2O_5 was deposited from a sodium metavanadate solution in water under ambient conditions. The resultant material exhibited the formula $\text{V}_2\text{O}_5 \cdot 0.5\text{H}_2\text{O}$. The 0.5 water molecules remains in the V_2O_5 layered structure unless the sample is heated above 250 °C. It was found that such high annealing made the thin film highly stable under different conditions. The electronic structure of the deposited V_2O_5 thin films was assessed with several methods. It was found that V_2O_5 films exhibited W_F values dependent on the preparation conditions. The measured W_F was lower for films prepared from fresh V_2O_5 –isopropanol (IPA) solutions (5.15 eV) than those prepared from a 24 h-old solution (5.5 eV). This difference was attributed to a gradual reduction of vanadium (from V^{5+} to V^{4+}) in IPA. OSCs made with V_2O_5 from fresh IPA solutions required no phototreatment before measurements, whereas those derived from old solutions required photoactivation. Outdoor stability measurements of encapsulated OSCs using V_2O_5 HTLs in either the normal or the inverted configuration revealed high stability for both devices: the PV response at T_{80} was retained for more than 1000 h.

Besides TMOs, GO and rGO have also demonstrated high potential for high-stability OSCs. Yun et al.^[348] developed an alternative method to obtain pr-GO that was prepared using p-TosNHNH₂ as a reductive medium and compared it with GO and rGO as HTLs in OSCs. A significantly enhanced performance of the fabricated devices was demonstrated by introducing pr-GO into the OSCs. Furthermore, cells with pr-GO manifested a much longer cell lifetime compared with cells with PEDOT:

PSS. Moreover, the use of CuSCN as the HTL improved the overall device stability as well as PCE,^[349] compared with the devices fabricated using either thermal-evaporated MoO_3 or PEDOT:PSS HTLs. These are few examples of OSCs that benefitted from the application of inorganic HTLs in advancing their shelf lifetime and long-term stability.

7.2. Stability of Perovskite Solar Cells

From an application point of view, the stability of solar cells is as important as their efficiency and processing cost. This is of particular significance for PSCs, as if they have to compete with existing PV technologies such as silicon and thin-film PVs that ensure a lifetime of over 20–25 years, they should also provide similar operational stability.^[1,350–352] It is important to note that the energy output of a solar cell is the product of its efficiency and lifetime,^[353] suggesting that any new PV technologies must demonstrate an operational stability prior to commercialization.

Perovskite materials are well known for their instability when exposed to operating conditions of a PV device. While much of their instability is material oriented, device interfaces also play a crucial role as some common charge extraction layers, e.g., metal oxides such as TiO_2 , ZnO , and MoO_3 are known to induce a chemical reaction at their interface with the perovskite photoactive layer.^[13,211,354–356] In many cases, this interfacial reaction is induced due to the defect states present at the surface of the adjacent charge extraction layer to the perovskite photoactive layer. This can be affirmed as efficient and stable PSCs almost always include a passivation agent or a post-treatment of these charge extraction layers prior to the deposition of the perovskite layer. Nonetheless, once the surface defects of these inorganic charge extraction layers are well taken care off, they lead to a more stable device operation than their organic counterparts.

For instance, Chen et al. used inorganic charge extraction layers and reported a certified hysteresis-free PCE > 15% in large-area (1 cm^2) MAPbI_3 PSCs.^[151] They used a ternary oxide HTL (NiMgLiO) for rapid charge extraction and niobium (Nb)-doped TiO_2 as the ETL in inverted planar PSC configuration and showed that the PSC retained over 90% of the initial performance after 1000 h of light soaking (Figure 21a–c). One must, however, note that low-temperature-processed NiO may limit electrical properties due to the high density of surface defects. SAMs on the NiO surface have also shown to improve their electrical properties, device performance, and stability. For instance, the anchoring of a ferrocene carboxylic acid on NiO improved the performance and stability of devices to UV light stress, as demonstrated by Zhang et al.^[357] Not only the PCE increases from 15.1% to 18.2%, but also the device retained $\approx 50\%$ of the initial PCE after 24 h of UV light exposure.

The structure and quality of NiO/perovskite interface affect the transience in the optoelectronic behavior of solar cells, from J – V hysteresis to light-soaking effects and stability. Nie et al. proposed the high-interface perovskite crystallinity, evaluated through grazing-incident XRD (GIXRD) and grazing-incident wide-angle XRD (GIWAXS) investigations, as the reason for their improved stability under light (up to 10 suns), using a hot casted MAPbI_3 .^[154] Moreover, in agreement with the work of Tsai et al.,^[254] the strained perovskite grown on PEDOT:PSS required

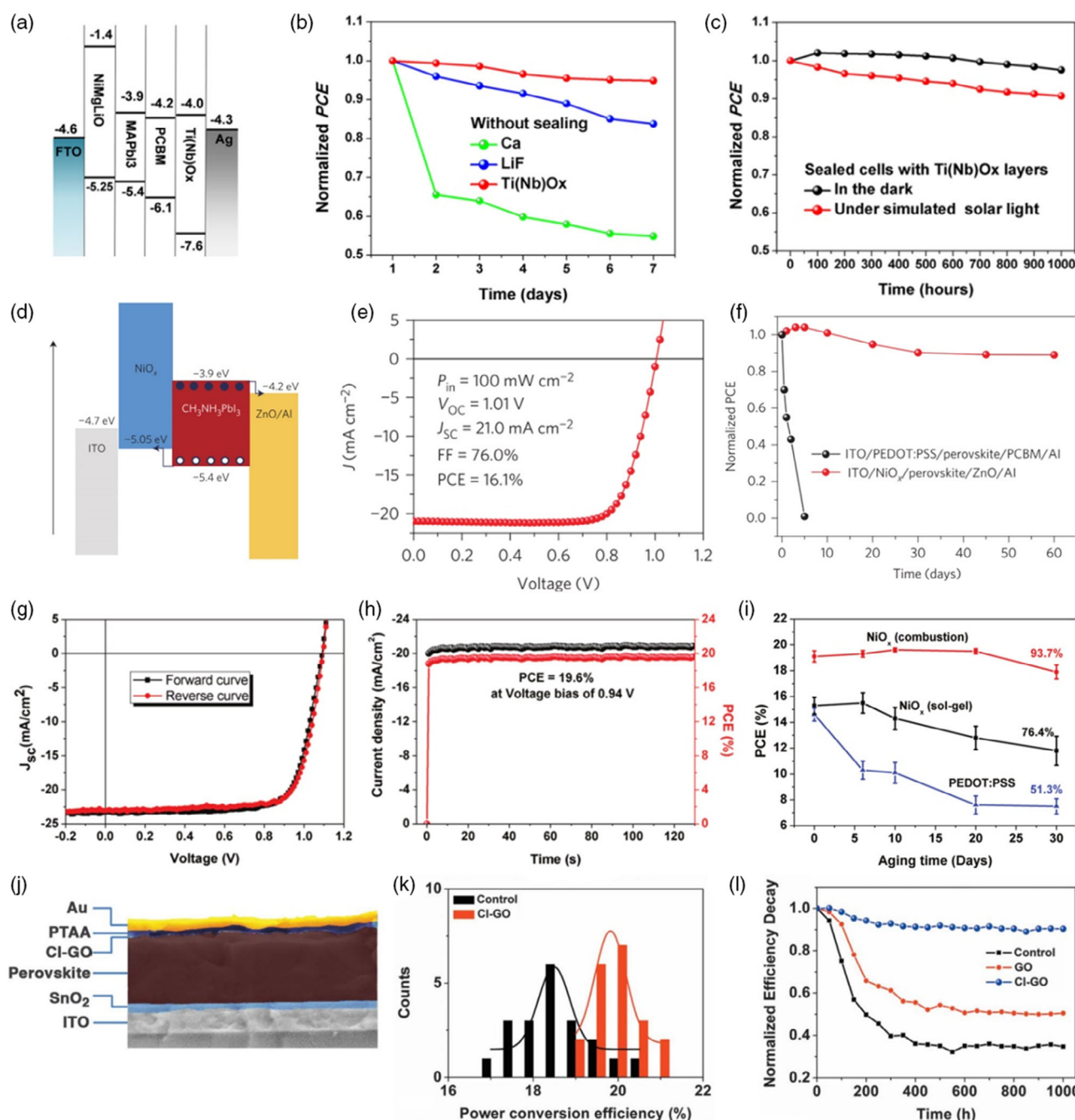


Figure 21. a) Energy levels of the various active layers in PSCs. b) Operational stability of nonencapsulated PSCs based on three different ETLs and doped NiO as HTL, stored in <20% humidity and in the dark. The devices were measured in ambient conditions. c) Stability measurements of encapsulated PSCs kept in the dark under continuous solar illumination (AM 1.5, 100 mW cm⁻², bias potential = 0, surface temperature 45–50 °C). UV light was cut off using a 420 nm UV light cutoff filter. Adapted with permission.^[151] Copyright AAAS. d) Energy levels of PSCs based on UPS measurement and e) current-voltage curve of a champion device measured at 1 sun condition. f) Stability of nonencapsulated PSCs stored and measured in ambient conditions. Reproduced with permission.^[105] Copyright 2016, Springer Nature. g) Current-voltage curves of the champion PSCs based on combustion based NiO_x. The device architecture is glass/FTO/NiO (combustion)/MA_{1-y}FA_yPbI_{3-x}Cl_x/PCBM/BCP/Ag. h) Maximum power point tracking of the same device in (g). i) Operational stability of nonencapsulated devices based on different HTLs, stored and measured in air. Reproduced with permission.^[108] Copyright 2018, WILEY-VCH. j) A cross-sectional view of the PSC showing chlorinated GO interlayer between the perovskite and metal contact. k) Histogram showing device performance trends with and without the GO interlayer. l) Lifetime of the encapsulated PSCs using different HTLs (no GO, GO, or chlorinated (Cl) GO). The stability was measured under 1000 h of light soaking (AM1.5G, 100 mW cm⁻²) at the maximum power point of 60 °C. Reproduced with permission.^[363] Copyright 2019, AAAS.

up to 10 min of light soaking to stabilize the V_{OC} , which was stable from the first seconds for the unstrained perovskite on NiO. Similarly, Chen et al. showed that the introduction of KCl or NaCl at the interface between NiO and CsFAMA perovskite stabilizes (and enhances) the V_{OC} and light emission properties due to an improved perovskite crystallinity, as evaluated from first-principles calculation.^[358] This, in turn, benefits operational stability of device.

You et al.^[105] demonstrated remarkable stability of all-metal-oxide PSCs using NiO_x and n-type ZnO NPs as the HTL and ETL, respectively, against water and oxygen, as compared with control devices using organic charge transport layers. Their p-i-n planar PSCs (glass/ITO/ NiO_x /perovskite/ZnO/Al) retained 90% of their initial PCE after 60 days of storage in air at room temperature. The control device using organic transport layers completely degraded in just five days at the same measurement conditions (Figure 21d–f). In another report, Liu et al.^[108] developed a low-temperature solution combustion-based method for high-quality NiO_x thin films. They applied this NiO_x film in devices and compared its performance with sol-gel NiO_x and PEDOT:PSS-based PSCs. Not only did the combustion-based NiO_x HTL show a better energy alignment with $MA_{1-y}FA_yPbI_{3-x}Cl_x$ perovskite, leading to a PCE exceeding 20%, but also a much higher stability compared with sol-gel-processed NiO_x and PEDOT:PSS-based devices (Figure 21g–i).

In another report, Tsai et al.^[254] demonstrated a remarkable PCE of over 20% using LiNiO as HTL (ITO/LiNiO/ $FA_{0.7}MA_{0.25}Cs_{0.05}PbI_3$ /PCBM/Al) and stability under continuous operation at AM 1.5G (100 mW cm^{-2}) illumination for more than 1500 h. The devices retained over 60% of the PCE after 1500 h. J_{SC} did not show any notable change; however, the FF of the device dropped substantially, leading to a PCE drop over time. It was suggested to be due to the degradation of the PCBM/Al contact, as also suggested in other literatures.^[359] Notably, the authors also reported stability under accelerated 10 sun solar intensities. While the reference $MAPbI_3$ -based PSCs completely degraded in 30 min, the $FA_{0.7}MA_{0.25}Cs_{0.05}PbI_3$ devices retained over 80% of the initial PCE after 600 min.

GO and rGO HTLs have also led to enhanced stability in PSCs. As an example, Zhou et al. reported a low-temperature-processed bilayer HTL comprising rGO and poly(triarylamine) PTAA for flexible and rigid inverted PSCs with 15.7% and 17% PCE, respectively.^[360] These devices exhibited significant light-soaking stability by retaining 96% of their initial PCE after continuous illumination of 500 h at 100 mW cm^{-2} . The control devices using PTAA only retained only 67% of the initial PCE after the same time. This improvement in stability was ascribed to the strong absorption of GO in the near-UV region, which prevents UV radiation damaging the perovskite photoactive layer. Wang et al. used GO and 2D MoS_2 as interlayers in p-i-n planar PSCs to reduce chemical reactions at the PEDOT:PSS/perovskite and perovskite/Ag interfaces.^[361] Not only did their devices show a PCE of 19.1%, a significant improvement was also demonstrated after 500 h of continuous testing at maximum power point. It was suggested, via chemical analysis of these interfaces, that the incorporation of the 2D materials minimizes reactivity at the interfaces and inhibits the movement of ionic species. In another report, Mahmoudi et al. demonstrated that Ag NPs anchored with rGO lead to enhanced thermal and

photostability.^[362] Ag:rGO-based PSCs aged at 90°C retained 94% of their initial performance after 90 h, whereas a control device without rGO showed a 39% decrease in PCE.

A remarkable device performance and operational stability were reported by Wang et al., who used chlorinated GO:PTAA bilayer as the HTL.^[363] They not only reported the highest PCE of 21% on an active area of 1 cm^2 using GO, but also, more importantly, retained 90% of its initial PCE after continuous illumination at a maximum power point under AM 1.5G at 60°C for 1000 h. Importantly, the stability of their devices was further certified by an accredited test center (AIST). This high stability is attributed to the formation of a strong bond between Pb of perovskite and Cl of chlorinated GO by obstructing the decomposed perovskite part to further degrade the organic HTL. As the interfacial degradation is avoided, damage to organic HTL is reduced and the devices demonstrate such a high stability for a prolonged period of time (see Figure 21j–l).

CuSCN as the HTL has also improved the operational stability of PSCs.^[33,327] As discussed earlier, Arora et al.^[327] found that their high-performance PSCs (PCE > 20%) underwent degradation due to the chemical reaction between Au (metal electrode) with CuSCN (HTL). To overcome this, they introduced an interlayer of rGO, which improved device thermal and photostability. The CuSCN-rGO-based device retained 95% of its initial performance after illumination of 1000 h at a maximum power point at 60°C , which was far superior to the control device using Spiro-OMeTAD HTL.

A key route to instability in PSCs is the migration of ionic species toward interfacial layers and their chemical reaction with metal electrodes, particularly the Ag top electrode.^[364] Wu et al. used doped NiO as the HTL in p-i-n planar PSCs and introduced a thin layer of chemically inert bismuth (Bi) between the organic ETL and the top electrode.^[119] Not only this thin layer prevented the migration of ionic species toward the metal electrode, but also enhanced device resilience against moisture. PSCs demonstrated remarkable long-term stability under humidity, thermal, and light stress (Figure 22). The devices maintained above 95% of the initial PCE after thermal aging at 85°C and after storage in ambient conditions for over 6000 h, making them one of the most stable planar PSCs to date.

8. Outlook and Challenges

Organic and perovskite solar cells represent two rapidly advanced PV technologies that continue to draw much interest. For further developments, many novel materials and alternative solution-based fabrication techniques are continuously demonstrated. Interfacial materials, in particular, play a vital role as they facilitate charge transport, passivate surface/interface defects, act as buffer/protective layers, and so on. These materials should possess favorable properties, such as chemical stability, robustness, and a desirable electronic structure combined with the ease of preparation, through solution-based techniques which could be applicable in large-area devices. Several recent reviews have been devoted to the progress made in the field of organic and inorganic charge transport interlayers for OSCs and PSCs with emphasis on device performance.^[317,318,365] In this Review, we

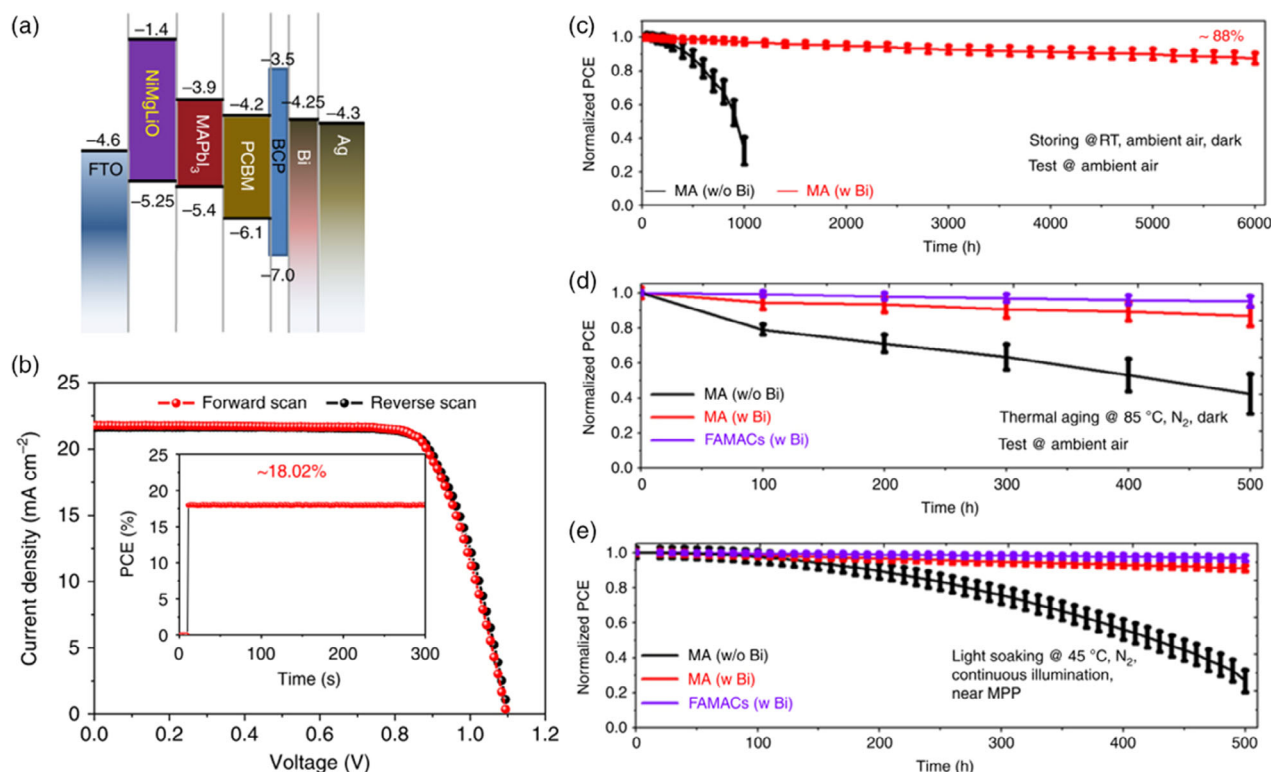


Figure 22. a) Schematic showing energy levels of various material layers in PSCs. b) Performance of a champion device. Inset shows maximum power point tracking. c–e) Operational stability of the PSCs at various conditions with and without a Bi interlayer and with two different types of perovskites. Error bar shows an average PCE from nine devices. The PCE is measured in ambient conditions periodically. Reproduced with permission.^[119] Copyright 2019, Springer Nature.

have summarized both the fascinating electronic properties of robust inorganic HTMs that are very relevant to device performance, as well as the latest advances in their application in organic and perovskite solar cells. This Review therefore differs from the relevant already existing ones that summarize the progress in HTLs in the rapidly evolving field of OSCs and PSCs in the sense that it correlates the materials' characteristics with the device performances. It can thus serve as a guide for the design and further development of robust inorganic compounds to be applied as interfacial materials at the hole-selective contacts of both OSCs and PSCs.

TMOs have been long established as highly efficient HTLs first in OSCs and subsequently in PSCs, due to their suitable electronic properties such as high W_F and transparency within the visible spectral range. In principle, they are more stable than organic molecules, but this is only true if their surface defects are passivated. A big advantage of metal oxide-based HTLs is their facile and controllable synthesis using a wide range of preparation methods. Their stoichiometry can be easily tuned during preparation (i.e., through doping), according to the properties that are desired for the targeted application. Even though they are able to deliver efficient hole transport for both regular and inverted OSCs and PSCs, they might compromise device stability especially in perovskite-based devices, due to the undesired degradation to create biproducts at the metal oxide/perovskite interface. Moreover, mixing with other oxides to form ternary

compounds (i.e., NiMgLiO or NiLiO) with “ideal” properties such as high crystallinity, less defects density, high conductivity, and energy-level alignment opens novel paths toward low-cost and high-performance OSCs and PSCs.

However, the existing TMO-based HTLs are characterized from fixed energy band edges and hence do not exactly fulfill the stringent requirements that govern ideal transport materials design, whose energy band positions should match those of the organic or perovskite absorber. Oxide-based charge transport interlayers are commonly used in OSCs and PSCs, but true interfacial energetic tunability has not been achieved, significantly limiting their adaptability to emerging PV absorber materials having different frontier orbital energies. Thus, HTMs having a broadly tunable VBM would provide generalizable means to optimize OSC/PSC performance. One way is to implement a design strategy using solution-processed TMO alloys where continuous VBM tunability could be achieved by alloying two or more electronically dissimilar oxides, realized by precursor compositional adjustment. For instance, wide-bandgap metal oxides with deep-lying O 2p-based VBMs and a high W_F should be used as tunable HTMs when altered in alloys with appropriate oxides. The position of the VBM will depend on the alloy composition (the nature of metal cations and atomic ratio). Tuning the oxides levels on demand will allow the perfect matching of the VBM of the HTL with that of the absorber to achieve high CT rates toward the hole-selective contact.

TMDs and copper-based HTLs have recently shown significant potential in advancing OSCs and, especially PSC performance, achieving high PCEs and good overall stability. Their ability to be processed from aqueous media makes them suitable candidates for the inverted PSC architecture, excluding them from being applied in the opposite device structure where they would cause the immediate destruction of the perovskite film. While in most cases of OSCs and PSCs device failure has been attributed to a spatial degradation at the absorber/transport layer interface, in the case of CuSCN, it was CuSCN/Au interface that led to degradation, which indicates that Ag electrodes are more appropriate to be combined with this highly promising HTM. There is still plenty of room for improvement, by exploring a combination of 2D perovskites and CuSCN, as it has been demonstrated recently.

Graphene oxide and reduced graphene oxide-based HTLs are very effective in enhancing the efficiency and prolonging the stability, especially UV stability, as they absorb UV. However, the application of doped or decorated GO and rGO as HTLs in these classes of PV devices has begun to draw attention and should be further explored in the years to come. Moreover, the development of composite materials such as GO:carbon nanotubes (CNTs) with extraordinary charge transport capabilities will allow full exploration of carbon-based compounds as interfacial materials for low-cost, large-area devices.

We note that the inorganic materials, particularly in their pristine form, leads to a lower PCE than their state-of-the-art inorganic counterparts, for both the OSCs and PSCs. As already elaborated earlier, this is because of a high energy barrier for hole extraction at the HTL/absorber interface, which limits the achievable V_{OC} , and also, due to the fact that some of the inorganic materials have shown to form a reactive interface with the absorber (perovskite). This creates byproducts at the HTL/perovskite interface, which acts as the recombination site during the CT process. The poor characteristics of the HTL/absorber interface can be overcome by efficient surface passivation and addition of ultrathin (1–2 nm) organic interlayers. The use of such interlayers has already shown to be very successful in, for example, PSCs and has resulted in PCEs between 18% and 21% using a range of inorganic materials (metal oxides, graphene oxide, CuSCN, etc.). Future research should focus to quantify losses at the HTL/perovskite interfaces, such as to calculate band bending and quasi-Fermi level splitting to provide an elaborated picture of the interfacial properties. Moreover, the combination of these robust inorganic materials with organic small molecules with desired electronic properties and ease of synthesis and processing methods such as SAMs, porphyrins, and phthalocyanines could also be in the correct route as it would prevent their direct contact with the absorber layer, hence preventing possible interfacial degradation while also allowing the development of novel material platforms with broadly tunable physical, optical, and electronic properties derived from combinations of the existing ones. To conclude, we should keep in mind that combined research studies at both material properties and device performances would offer the necessary knowledge to further advance these existing classes of inorganic compounds and, accordingly, OSCs and PSC technologies.

Conflict of Interest

The authors declare no conflict of interest.

Keywords

inorganic materials, interfacial recombinations, long-term stabilities, perovskite solar cells

Received: September 7, 2020

Revised: October 14, 2020

Published online: December 10, 2020

- [1] M. A. Green, *Nat. Energy* **2016**, 1, 15015.
- [2] M. Kaltenbrunner, G. Adam, E. D. Głowacki, M. Drack, R. Schwödauer, L. Leonat, D. H. Apaydin, H. Groiss, M. C. Scharber, M. S. White, N. S. Sariciftci, S. Bauer, *Nat. Mater.* **2015**, 14, 1032.
- [3] S. S. Shin, W. S. Yang, J. H. Noh, J. H. Suk, N. J. Jeon, J. H. Park, J. S. Kim, W. M. Seong, S. I. Seok, *Nat. Commun.* **2015**, 6, 7410.
- [4] F. Di Giacomo, V. Zardetto, G. Lucarelli, L. Cinà, A. Di Carlo, M. Creatore, T. M. Brown, *Nano Energy* **2016**, 30, 460.
- [5] C.-Y. Chen, J.-H. Chang, K.-M. Chiang, H.-L. Lin, S.-Y. Hsiao, H.-W. Lin, *Adv. Funct. Mater.* **2015**, 25, 7064.
- [6] M. Saliba, T. Matsui, J.-Y. Seo, K. Domanski, J.-P. Correa-Baena, M. K. Nazeeruddin, S. M. Zakeeruddin, W. Tress, A. Abate, A. Hagfeldt, M. Grätzel, *Energy Environ. Sci.* **2016**, 9, 1989.
- [7] Y. Bai, Q. Dong, Y. Shao, Y. Deng, Q. Wang, L. Shen, D. Wang, W. Wei, J. Huang, *Nat. Commun.* **2016**, 7, 12806.
- [8] Z. H. Bakr, Q. Wali, A. Fakharuddin, L. Schmidt-Mende, T. M. Brown, R. Jose, *Nano Energy* **2017**, 34, 271.
- [9] P. Schulz, E. Edri, S. Kirmayer, G. Hodes, D. Cahen, A. Kahn, *Energy Environ. Sci.* **2014**, 7, 1377.
- [10] J. Shi, X. Xu, D. Li, Q. Meng, *Small* **2015**, 11, 2472.
- [11] Y.-K. Chih, J.-C. Wang, R.-T. Yang, C.-C. Liu, Y.-C. Chang, Y.-S. Fu, W.-C. Lai, P. Chen, T.-C. Wen, Y.-C. Huang, C.-S. Tsao, T.-F. Guo, *Adv. Mater.* **2016**, 28, 8687.
- [12] A. Fakharuddin, L. Schmidt-Mende, G. Garcia-Belmonte, R. Jose, I. Mora-Sero, *Adv. Energy Mater.* **2017**, 7, 1700623.
- [13] K. K. Wong, A. Fakharuddin, P. Ehrenreich, T. Deckert, M. Abdi-Jalebi, R. H. Friend, L. Schmidt-Mende, *J. Phys. Chem. C* **2018**, 122, 10691.
- [14] T.-H. Han, S. Tan, J. Xue, L. Meng, J.-W. Lee, Y. Yang, *Adv. Mater.* **2019**, 31, 1803515.
- [15] P. Schulz, D. Cahen, A. Kahn, *Chem. Rev.* **2019**, 119, 3349.
- [16] K. Schütt, P. K. Nayak, A. J. Ramadan, B. Wenger, Y.-H. Lin, H. J. Snaith, *Adv. Funct. Mater.* **2019**, 29, 1900466.
- [17] W. J. Potscavage, A. Sharma, B. Kippelen, *Acc. Chem. Res.* **2009**, 42, 1758.
- [18] N. K. Elumalai, A. Uddin, *Energy Environ. Sci.* **2016**, 9, 391.
- [19] H. S. Kim, I. Mora-Sero, V. Gonzalez-Pedro, F. Fabregat-Santiago, E. J. Juarez-Perez, N.-G. Park, J. Bisquert, *Nat. Commun.* **2013**, 4, 2242.
- [20] E. J. Juarez-Perez, M. Wußler, F. Fabregat-Santiago, K. Lakus-Wollny, E. Mankel, T. Mayer, W. Jaegermann, I. Mora-Sero, *J. Phys. Chem. Lett.* **2014**, 5, 680.
- [21] L. Fagioli, F. Bella, *Energy Environ. Sci.* **2019**, 12, 3437.
- [22] C. Zhou, H. Lin, Q. He, L. Xu, M. Worku, M. Chaaban, S. Lee, X. Shi, M.-H. Due, B. Ma, *Mater. Sci. Eng. R Rep.* **2019**, 137, 38.
- [23] M. M. Lee, J. Teuscher, T. Miyasaka, T. N. Murakami, H. J. Snaith, *Science* **2012**, 338, 643.
- [24] J. Burschka, N. Pellet, S.-J. Moon, R. Humphry-Baker, P. Gao, M. K. Nazeeruddin, M. Grätzel, *Nature* **2013**, 499, 316.

- [25] H.-S. Kim, C.-R. Lee, J.-H. Im, K.-B. Lee, T. Moehl, A. Marchioro, S.-J. Moon, R. Humphry-Baker, J.-H. Yum, J. E. Moser, M. Grätzel, N.-G. Park, *Sci. Rep.* **2012**, 2, 591.
- [26] NREL, Best Cell Efficiency Report, <https://www.nrel.gov/pv/assets/pdfs/pv-efficiencies-04-02-2018.pdf> (accessed: February 2020).
- [27] J. H. Im, C.-R. Lee, J.-W. Lee, S.-W. Parka, N.-G. Park, *Nanoscale* **2011**, 3, 4088.
- [28] M. Grätzel, *Nat. Mater.* **2014**, 13, 838.
- [29] S. Brittman, G. W. P. Adhyaksa, E. C. Garnett, *MRS Commun.* **2015**, 5, 7.
- [30] M. Liu, M. B. Johnston, H. J. Snaith, *Nature* **2013**, 501, 395.
- [31] L. Dou, Y. M. Yang, J. You, Z. Hong, W.-H. Chang, G. Li, Y. Yang, *Nat. Commun.* **2014**, 5, 5404.
- [32] D. Liu, T. L. Kelly, *Nat. Photonics* **2014**, 8, 133.
- [33] S. Ye, W. Sun, Y. Li, W. Yan, H. Peng, Z. Bian, Z. Liu, C. Huang, *Nano Lett.* **2015**, 15, 3723.
- [34] A. Alnuaimi, I. Almansouri, A. Nayfeh, *AIP Adv.* **2016**, 6, 115012.
- [35] L. Meng, J. You, T.-F. Guo, Y. Yang, *Acc. Chem. Res.* **2016**, 49, 155.
- [36] F. Di Giacomo, A. Fakhruddin, R. Jose, T. M. Brown, *Energy Environ. Sci.* **2016**, 9, 3007.
- [37] S. N. Habisreutinger, T. Leijtens, G. E. Eperon, S. D. Stranks, R. J. Nicholas, H. J. Snaith, *Nano Lett.* **2014**, 14, 5561.
- [38] H. Zhou, Y. Shi, Q. Dong, H. Zhang, Y. Xing, K. Wang, Y. Du, T. Ma, *J. Phys. Chem. Lett.* **2014**, 5, 3241.
- [39] O. Almora, L. Vaillant-Roca, G. Garcia-Belmonte, *Rev. Cub. Fis.* **2017**, 34, 58.
- [40] A. Senocrate, I. Moudrakovski, G. Y. Kim, T.-Y. Yang, G. Gregori, M. Grätzel, J. Maier, *Angew. Chem., Int. Ed.* **2017**, 56, 7755.
- [41] A. Zohar, I. Levine, S. Gupta, O. Davidson, D. Azulay, O. Millo, I. Balberg, G. Hodes, D. Cahen, *ACS Energy Lett.* **2017**, 2, 2408.
- [42] C. C. Stoumpos, C. D. Malliakas, M. G. Kanatzidis, *Inorg. Chem.* **2013**, 52, 9019.
- [43] T. Baikie, Y. Fang, J. M. Kadro, M. Schreyer, F. Wei, S. G. Mhaisalkar, M. Graetzel, T. J. White, *J. Mater. Chem. A* **2013**, 1, 5628.
- [44] G. E. Eperon, S. D. Stranks, C. Menelaou, M. B. Johnston, L. M. Herz, H. J. Snaith, *Energy Environ. Sci.* **2014**, 7, 982.
- [45] W. E. I. Sha, X. Ren, L. Chen, W. C. H. Choy, *Appl. Phys. Lett.* **2015**, 106, 221104.
- [46] S. De Wolf, J. Holovsky, S.-J. Moon, P. Löper, B. Niesen, M. Ledinsky, F.-J. Haug, J.-H. Yum, C. Ballif, *J. Phys. Chem. Lett.* **2014**, 5, 1035.
- [47] Q. Lin, A. Armin, R. C. R. Nagiri, P. L. Burn, P. Meredith, *Nat. Photonics* **2014**, 9, 106.
- [48] S. Collavini, S. F. Völker, J. L. Delgado, *Angew. Chem., Int. Ed.* **2015**, 54, 9757.
- [49] J. D. Servaites, M. A. Ratner, T. J. Marks, *Energy Environ. Sci.* **2011**, 4, 4410.
- [50] C. Wehrenfennig, G. E. Eperon, M. B. Johnston, H. J. Snaith, L. M. Herz, *Adv. Mater.* **2014**, 26, 1584.
- [51] L. M. Herz, *Ann. Rev. Phys. Chem.* **2016**, 67, 65.
- [52] C. Motta, F. El-Mellouhi, S. Sanvito, *Sci. Rep.* **2015**, 5, 12746.
- [53] S. D. Stranks, G. E. Eperon, G. Grancini, C. Menelaou, M. J. P. Alcocer, T. Leijtens, L. M. Herz, A. Petrozza, H. J. Snaith, *Science* **2013**, 342, 341.
- [54] G. Giorgi, J.-I. Fujisawa, H. Segawa, K. Yamashita, *J. Phys. Chem. Lett.* **2013**, 4, 4213.
- [55] E. Edri, S. Kirmayer, S. Mukhopadhyay, K. Gartsman, G. Hodes, D. Cahen, *Nat. Commun.* **2014**, 5, 3461.
- [56] M. Jørgensen, K. Norrman, F. C. Krebs, *Sol. Energy Mater. Sol. Cells* **2008**, 92, 686.
- [57] P. Lopez-Varo, J. A. Jiménez-Tejada, M. García-Rosell, S. Ravishanker, G. Garcia-Belmonte, J. Bisquert, O. Almora, *Adv. Energy Mater.* **2018**, 8, 1702772.
- [58] J. Huang, Y. Yuan, Y. Shao, Y. Yan, *Nat. Rev. Mater.* **2017**, 2, 17042.
- [59] T.-C. Sum, N. Mathews, *Halide Perovskites Photovoltaics, Light Emitting Devices, and Beyond*, Wiley-VCH Verlag GmbH & Co. KGaA, Weinheim **2018**, p. 300.
- [60] I. Mora-Seró, *Joule* **2018**, 2, 585.
- [61] T. Ameri, P. Khoram, J. Min, C. J. Brabec, *Adv. Mater.* **2013**, 25, 4245.
- [62] J. Kniepert, M. Schubert, J. C. Blakesley, D. Neher, *J. Phys. Chem. Lett.* **2011**, 2, 700.
- [63] N. A. Ran, S. Roland, J. A. Love, V. Savikhin, C. J. Takacs, Y.-T. Fu, H. Li, V. Coropceanu, X. Liu, J.-L. Brédas, G. C. Bazan, M. F. Toney, D. Neher, T.-Q. Nguyen, *Nat. Commun.* **2017**, 8, 79.
- [64] J. Weickert, R. B. Dunbar, H. C. Hesse, W. Wiedemann, L. Schmidt-Mende, *Adv. Mater.* **2011**, 23, 1810.
- [65] U. S. Christoph Brabec, V. Dyakonov, *Organic Photovoltaics: Materials, Device Physics, and Manufacturing Technologies*, Wiley-VCH Verlag GmbH & Co. KGaA, Weinheim **2008**.
- [66] J. J. M. Halls, K. Pichler, R. H. Friend, *Appl. Phys. Lett.* **1996**, 68, 3120.
- [67] T. Kirchartz, J. Bisquert, I. Mora-Seroc, G. Garcia-Belmonte, *Phys. Chem. Chem. Phys.* **2015**, 17, 4007.
- [68] A. Pivrikas, N. S. Sariciftci, G. Juška, R. Österbacka, *Prog. Photovolt.: Res. Appl.* **2007**, 15, 677.
- [69] D. M. Stoltzfus, J. E. Donaghey, A. Armin, P. E. Shaw, P. L. Burn, P. Meredith, *Chem. Rev.* **2016**, 116, 12920.
- [70] M. Schwarze, W. Tress, B. Beyer, F. Gao, R. Scholz, C. Poelking, K. Ortstein, A. A. Günther, D. Kasemann, D. Andrienko, K. Leo, *Science* **2016**, 352, 1446.
- [71] L. Calió, S. Kazim, M. Grätzel, S. Ahmad, *Angew. Chem., Int. Ed.* **2016**, 55, 14522.
- [72] P. Agarwala, D. Kabra, *J. Mater. Chem. A* **2017**, 5, 1348.
- [73] K. Kawano, R. Pacios, D. Poplavskyy, J. Nelson, D. D. C. Bradley, J. R. Durrant, *Sol. Energy Mater. Sol. Cells* **2006**, 90, 3520.
- [74] Q. Burlingame, X. Huang, X. Liu, C. Jeong, C. Coburn, S. R. Forrest, *Nature* **2019**, 573, 394.
- [75] I. A. de Castro, R. S. Datta, J. Z. Ou, A. Castellanos-Gomez, S. Sriram, T. Daeneke, K. Kalantar-Zadeh, *Adv. Mater.* **2017**, 29, 1701619.
- [76] K. C. Santosh, R. C. Longo, R. Addou, R. M. Wallace, K. Cho, *Sci. Rep.* **2016**, 6, 33562.
- [77] D. O. Scanlon, G. W. Watson, D. J. Payne, G. R. Atkinson, R. G. Egdel, D. S. L. Law, *J. Phys. Chem. C* **2010**, 114, 4636.
- [78] C. Battaglia, X. Yin, M. Zheng, I. D. Sharp, T. Chen, S. McDonnell, A. Azcatl, C. Carraro, B. Ma, R. Maboudian, R. M. Wallace, A. Javey, *Nano Lett.* **2014**, 14, 967.
- [79] K. Inzani, M. Nematollahi, F. Vullum-Bruer, T. Grande, T. W. Reenaas, S. M. Selbach, *Phys. Chem. Chem. Phys.* **2017**, 19, 9232.
- [80] H. A. Tahini, X. Tan, S. N. Lou, J. Scott, R. Amal, Y. H. Ng, S. C. Smith, *ACS Appl. Mater. Interfaces* **2016**, 8, 10911.
- [81] D. S. Lambert, A. Lennon, P. A. Burr, *J. Phys. Chem. C* **2018**, 122, 27241.
- [82] H. Simchi, B. E. McCandless, T. Meng, J. H. Boyle, W. N. Shafarman, *J. Appl. Phys.* **2013**, 114, 013503.
- [83] H. Zheng, J. Z. Ou, M. S. Strano, R. B. Kaner, A. Mitchell, K. Kalantar-zadeh, *Adv. Funct. Mater.* **2011**, 21, 2175.
- [84] J. Zhu, S. Wang, S. Xie, H. Li, *Chem. Comm.* **2011**, 47, 4403.
- [85] J. Y. Zheng, Z. Haider, T. K. Van, A. U. Pawar, M. J. Kang, C. W. Kim, Y. S. Kang, *CrystEngComm* **2015**, 17, 6070.
- [86] S. B. Lee, J. H. Beak, B. H. Kang, K.-Y. Dong, Y.-Y. Yu, Y. D. Lee, B.-K. Ju, *Sol. Energy Mater. Sol. Cells* **2013**, 117, 203.
- [87] W. J. Stepniowski, W. Z. Misiolek, *Nanomaterials* **2018**, 8, 379.
- [88] R. A. Evarestov, V. A. Veryazov, *Phys. Status Solidi B* **1990**, 158, 201.
- [89] J. Ghijsen, L. H. Tjeng, J. van Elp, H. Eskes, J. Westerink, G. A. Sawatzky, M. T. Czyzyk, *Phys. Rev. B* **1988**, 38, 11322.
- [90] R. Paulose, R. Mohan, V. Parihar, *Nano-Struct. Nano-Object.* **2017**, 11, 102.

- [91] N. Tsuda, K. Nasu, A. Fujimori, K. Siraatori, *Electronic Conduction in Oxides*, Vol. XI, Springer-Verlag, Berlin Heidelberg, p. 372.
- [92] Y. Wang, J. Zhu, X. Yang, L. Lu, X. Wang, *Thermochim. Acta* **2005**, 437, 106.
- [93] S. Casassa, A. M. Ferrari, M. Busso, C. Pisani, *J. Phys. Chem. B* **2002**, 106, 12978.
- [94] X. Yin, Y. Guo, H. Xie, W. Que, L. B. Kong, *Sol. RRL* **2019**, 3, 1900001.
- [95] K. O. Okoba, A. C. Eloka-Eboka, F. L. Inambao, *Renew. Sustainable Energy Rev.* **2018**, 82, 2900.
- [96] A. Venter, J. Botha, *South Afr. J. Sci.* **2011**, 107, 1.
- [97] M. D. Irwin, D. Bruce Buchholz, A. W. Hains, R. P. H. Chang, T. J. Marks, *Proc. Natl. Acad. Sci.* **2008**, 105, 2783.
- [98] E. L. Ratcliff, J. Meyer, K. X. Steirer, N. R. Armstrong, D. Olson, A. Kahn, *Org. Electron.* **2012**, 13, 744.
- [99] W.-L. Jang, Y.-M. Lu, W.-S. Hwang, T.-L. Hsiung, H. P. Wang, *Appl. Phys. Lett.* **2009**, 94, 062103.
- [100] C. M. Osburn, R. W. Vest, *J. Phys. Chem. Solids* **1971**, 32, 1331.
- [101] W. J. Moore, *Seven Solid States: An Introduction to the Chemistry and Physics of Solids*, W. A. Benjamin, Inc., Menlo Park, CA **1967**.
- [102] P. Dubey, N. Kaurav, R. S. Devan, G. S. Okram, Y. K. Kuod, *RSC Adv.* **2018**, 8, 5882.
- [103] L. Ai, G. Fang, L. Yuan, N. Liu, M. Wang, C. Li, Q. Zhang, J. Li, X. Zhao, *Appl. Surf. Sci.* **2008**, 254, 2401.
- [104] M. T. Greiner, M. G. Helander, Z.-B. Wang, W.-M. Tang, Z.-H. Lu, *J. Phys. Chem. C* **2010**, 114, 19777.
- [105] J. You, L. Meng, T.-B. Song, T.-F. Guo, Y. M. Yang, W.-H. Chang, Z. Hong, H. Chen, H. Zhou, Q. Chen, Y. Liu, N. De Marco, Y. Yang, *Nat. Nanotechnol.* **2016**, 11, 75.
- [106] Y. Bai, H. Yu, Z. Zhu, K. Jiang, T. Zhang, N. Zhao, S. Yang, H. Yan, *J. Mater. Chem. A* **2015**, 3, 9098.
- [107] S. T. Aruna, A. S. Mukasyan, *Curr. Opin. Solid State Mater. Sci.* **2008**, 12, 44.
- [108] Z. Liu, J. Chang, Z. Lin, L. Zhou, Z. Yang, D. Chen, C. Zhang, S. F. Liu, Y. Hao, *Adv. Energy Mater.* **2018**, 8, 1703432.
- [109] M. Najafi, F. Di Giacomo, D. Zhang, S. Shanmugam, A. Senes, W. Verhees, A. Hadjipour, Y. Galagan, T. Aernouts, S. Veenstra, R. Andriessen, *Small* **2018**, 14, 1702775.
- [110] H. Zhang, J. Cheng, F. Lin, H. He, J. Mao, K. S. Wong, A. K. Jen, W. C. Choy, *ACS Nano* **2016**, 10, 1503.
- [111] J. Zheng, L. Hu, J. S. Yun, M. Zhang, C. F. J. Lau, J. Bing, X. Deng, Q. Ma, Y. Cho, W. Fu, C. Chen, M. A. Green, S. Huang, A. W. Y. Ho-Baillie, *ACS Appl. Energy Mater.* **2018**, 1, 561.
- [112] W. Chen, L. Xu, X. Feng, J. Jie, Z. He, *Adv. Mater.* **2017**, 29, 1603923.
- [113] K. C. Icli, M. Ozenbas, *Electrochimica Acta* **2018**, 263, 338.
- [114] J. Tirado, M. Vázquez-Montoya, C. Roldán-Carmona, M. Ralaiaisoa, N. Koch, M. K. Nazeeruddin, F. Jaramillo, *ACS Appl. Energy Mater.* **2019**, 2, 4890.
- [115] Z. Liu, A. Zhu, F. Cai, L. Tao, Y. Zhou, Z. Zhao, Q. Chen, Y. B. Cheng, H. Zhou, *J. Mater. Chem. A* **2017**, 5, 6597.
- [116] D. Di Girolamo, F. Matteocci, M. Piccinini, A. Di Carlo, D. Dini, *Sol. Energy Mater. Sol. Cells* **2020**, 205, 110288.
- [117] I. J. Park, G. Kang, M. A. Park, J. S. Kim, S. W. Seo, D. H. Kim, K. Zhu, T. Park, J. Y. Kim, *ChemSusChem* **2017**, 10, 2660.
- [118] J. Sun, J. Lu, B. Li, L. Jiang, A. S. R. Chesman, A. D. Scully, T. R. Gengenbach, Y.-B. Cheng, J. J. Jasieniak, *Nano Energy* **2018**, 49, 163.
- [119] S. Wu, R. Chen, S. Zhang, B. H. Babu, Y. Yue, H. Zhu, Z. Yang, C. Chen, W. Chen, Y. Huang, S. Fang, T. Liu, L. Han, W. Chen, *Nat. Commun.* **2019**, 10, 1161.
- [120] J. H. Park, J. Seo, S. Park, S. S. Shin, Y. C. Kim, N. J. Jeon, H.-W. Shin, T. K. Ahn, J. H. Noh, S. C. Yoon, C. S. Hwang, S. I. Seok, *Adv. Mater.* **2015**, 27, 4013.
- [121] T. Abzieher, S. Moghadamzadeh, F. Schackmar, H. Eggers, F. Sutterlüt, A. Farooq, D. Kojda, K. Habicht, R. Schmager, A. Mertens, R. Azmi, L. Kloth, J. A. Schwenzer, M. Hetterich, U. Lemmer, B. S. Richards, M. Powalla, U. W. Paetzold, *Adv. Energy Mater.* **2019**, 9, 1802995.
- [122] S. Cong, G. Zou, Y. Lou, H. Yang, Y. Su, J. Zhao, C. Zhang, P. Ma, Z. Lu, H. Fan, Z. Huang, *Nano Lett.* **2019**, 19, 3676.
- [123] B. Zhao, L. C. Lee, L. Yang, A. J. Pearson, H. Lu, X. J. She, L. Cui, K. H. L. Zhang, R. L. Z. Hye, A. Karani, P. Xu, A. Sadhanala, N. C. Greenham, R. H. Friend, J. L. MacManus-Driscoll, D. Di, *ACS Appl. Mater. Interfaces* **2018**, 10, 41849.
- [124] D. Koushik, M. Jošt, A. Dučinskis, C. Burgess, V. Zardetto, C. Weijters, M. A. Verheijen, W. M. M. Kessels, S. Albrechtbe, M. Creatore, *J. Mater. Chem. C* **2019**, 7, 12532.
- [125] E. Aydin, J. Troughton, M. De Bastiani, E. Ugur, M. Sajjad, A. Alzahrani, M. Neophytou, U. Schwingenschlogl, F. Laquai, D. Baran, S. De Wolf, *ACS Appl. Energy Mater.* **2018**, 1, 6227.
- [126] H. Lee, Y.-T. Huang, M. W. Horn, S.-P. Feng, *Sci. Rep.* **2018**, 8, 5590.
- [127] S. Pang, C. Zhang, H. Dong, D. Chen, W. Zhu, H. Xi, J. Chang, Z. Lin, J. Zhang, Y. Hao, *ACS Appl. Energy Mater.* **2019**, 2, 4700.
- [128] J. Y. Jeng, K.-C. Chen, T.-Y. Chiang, P.-Y. Lin, T.-D. Tsai, Y.-C. Chang, T.-F. Guo, P. Chen, T.-C. Wen, Y.-J. Hsu, *Adv. Mater.* **2014**, 26, 4107.
- [129] K.-C. Wang, P.-S. Shen, M.-H. Li, S. Chen, M.-W. Lin, P. Chen, T.-F. Guo, *ACS Appl. Mater. Interfaces* **2014**, 6, 11851.
- [130] G. Niu, S. Wang, J. Li, W. Li, L. Wang, *J. Mater. Chem. A* **2018**, 6, 4721.
- [131] H. J. Jung, S. Kim, V. P. Dravid, H. J. Jung, V. P. Dravid, H. J. Jung, S. Kim, D. Kim, B. Shin, J. Park, *Adv. Mater.* **2018**, 30, 1802769.
- [132] B. Roose, R. H. Friend, *Adv. Mater. Interfaces* **2019**, 6, 1801788.
- [133] J. Desilvestro, *J. Electrochem. Soc.* **1988**, 135, 885.
- [134] J. H. Kim, P.-W. Liang, S. T. Williams, N. Cho, C.-C. Chueh, M. S. Glaz, D. S. Ginger, A. K.-Y. Jen, *Adv. Mater.* **2015**, 27, 695.
- [135] J. W. Jung, C.-C. Chueh, A. K.-Y. Jen, *Adv. Mater.* **2015**, 27, 7874.
- [136] K. Yao, F. Li, Q. He, X. Wang, Y. Jiang, H. Huang, A. K.-Y. Jen, *Nano Energy* **2017**, 40, 155.
- [137] W. Chen, Y. Wu, J. Fan, A. B. Djurišić, F. Liu, H. W. Tam, A. Ng, C. Surya, W. K. Chan, D. Wang, Z.-B. He, *Adv. Energy Mater.* **2018**, 8, 1703519.
- [138] Y. Wei, K. Yao, X. Wang, Y. Jiang, X. Liu, N. Zhou, F. Li, *Appl. Surf. Sci.* **2018**, 427, 782.
- [139] J. H. Lee, Y. W. Noh, I. S. Jin, S. H. Park, J. W. Jung, *J. Power Sources* **2019**, 412, 425.
- [140] Z. Hu, D. Chen, P. Yang, L. Yang, L. Qin, Y. Huang, X. Zhao, *Appl. Surf. Sci.* **2018**, 441, 258.
- [141] X. Wan, Y. Jiang, Z. Qiu, H. Zhang, X. Zhu, I. Sikandar, B. Cao, X. Liu, X. Chen, B. Cao, *ACS Appl. Energy Mater.* **2018**, 1, 3947.
- [142] A. B. Huang, J. T. Zhu, Y. Yu, Y. Liu, S. H. Bao, L. Lei, P. Jin, A. B. Huang, J. T. Zhu, Y. Yu, J. Y. Zheng, S. W. Yang, P. Jin, *J. Mater. Chem. C* **2016**, 4, 10839.
- [143] R. Kaneko, T. H. Chowdhury, G. Wu, M. E. Kayesh, S. Kazaoui, K. Sugawa, J.-J. Lee, T. Noda, A. Islam, J. Otsuki, *Sol. Energy* **2019**, 181, 243.
- [144] Y. Xie, K. Lu, J. Duan, Y. Jiang, L. Hu, T. Liu, Y. Zhou, B. Hu, *ACS Appl. Mater. Interfaces* **2018**, 10, 14153.
- [145] Y. Hou, L. J. Tang, H. W. Qiao, Z. R. Zhou, Y. L. Zhong, L. R. Zheng, M. J. Chen, S. Yang, H. G. Yang, *J. Mater. Chem. A* **2019**, 7, 20905.
- [146] X. Xia, Y. Jiang, X. Wang, L. Wang, F. Li, Q. Wan, *ACS Appl. Mater. Interfaces* **2018**, 10, 44501.
- [147] S. Wang, B. Zhang, D. Feng, Z. Lin, J. Zhang, Y. Hao, X. Fan, J. Chang, *J. Mater. Chem. C* **2019**, 7, 9270.
- [148] P. S. Chandrasekhar, Y.-H. Seo, Y.-J. Noh, S.-I. Na, *Appl. Surf. Sci.* **2019**, 481, 588.
- [149] B. Ge, H. W. Qiao, Z. Q. Lin, Z. R. Zhou, A. P. Chen, S. Yang, Y. Hou, H. G. Yang, *Sol. RRL* **2019**, 3, 1900192.

- [150] G. Li, Y. Jiang, S. Deng, A. Tam, P. Xu, M. Wong, H. S. Kwok, *Adv. Sci.* **2017**, *4*, 1700463.
- [151] W. Chen, Y. Wu, Y. Yue, J. Liu, W. Zhang, X. Yang, H. Chen, E. Bi, I. Ashraful, M. Gratzel, L. Han, *Science* **2015**, *350*, 944.
- [152] W. Chia-Ching, Y. Cheng-Fu, *Nanoscale Res. Lett.* **2013**, *8*, 33.
- [153] Z. Qiu, H. Gong, G. Zheng, S. Yuan, H. Zhang, X. Zhu, H. Zhou, B. Cao, *J. Mater. Chem. C* **2017**, *5*, 7084.
- [154] W. Nie, H. Tsai, J.-C. Blancon, F. Liu, C. C. Stoumpos, B. Traore, M. Kepenekian, O. Durand, C. Katan, S. Tretiak, J. Crochet, P. M. Ajayan, M. G. Kanatzidis, J. Even, A. D. Mohite, *Adv. Mater.* **2018**, *30*, 1703879.
- [155] D. Di Girolamo, N. Phung, M. Jošt, A. Al-Ashouri, G. Chistiakova, J. Li, J. A. Márquez, T. Unold, L. Korte, S. Albrecht, A. Di Carlo, D. Dini, A. Abate, *Adv. Mater. Interfaces* **2019**, *6*, 1900789.
- [156] P.-C. Chen, S.-H. Yang, *ACS Appl. Energy Mater.* **2019**, *2*, 6705.
- [157] Q. Fu, S. Xiao, X. Tang, T. Hu, *Org. Electron.* **2019**, *69*, 34.
- [158] H.-S. Kim, A. Hagfeldt, J.-Y. Seo, S. M. Zakeeruddin, M. Gratzel, H. Xie, M. Lira-Cantu, *ACS Omega* **2017**, *2*, 9074.
- [159] W. Chen, F.-Z. Liu, X.-Y. Feng, A. B. Djurišić, W. K. Chan, Z.-B. He, *Adv. Energy Mater.* **2017**, *7*, 1700722.
- [160] B. Ingham, S. C. Hendy, S. V. Chong, J. L. Tallon, *Phys. Rev. B* **2005**, *72*, 075109.
- [161] F. Xie, W. C. H. Choy, C. Wang, X. Li, S. Zhang, J. Hou, *Adv. Mater.* **2013**, *25*, 2051.
- [162] C. N. R. Rao, *Annu. Rev. Phys. Chem.* **1989**, *40*, 291.
- [163] S. Lany, *J. Phys.: Condens. Matter* **2015**, *27*, 283203.
- [164] I. T. Sachs-Quintana, W. R. Mateker, D. E. Orozco, R. Cheacharoen, S. Sweetnam, M. D. McGehee, T. Heumuller, C. J. Brabec, C. J. Brabec, *Adv. Funct. Mater.* **2014**, *24*, 3978.
- [165] K. E. Lee, L. Liu, T. L. Kelly, *J. Phys. Chem. C* **2014**, *118*, 27735.
- [166] M. Vasilopoulou, A. M. Douvas, D. G. Georgiadou, L. C. Palilis, S. Kennou, L. Sygellou, A. Soultati, I. Kostis, G. Papadimitropoulos, D. Davazoglou, P. Argitis, *J. Am. Chem. Soc.* **2012**, *134*, 16178.
- [167] S. Park, J. Jeong, G. Hyun, M. Kim, H. Lee, Y. Yi, *Sci. Rep.* **2016**, *6*, 35262.
- [168] H. C. Weerasinghe, S. E. Watkins, N. Duffy, D. J. Jones, A. D. Scully, *Sol. Energy Mater. Sol. Cells* **2015**, *132*, 485.
- [169] E. Voroshazi, G. Uytterhoeven, K. Cnops, T. Conard, P. Favia, H. Bender, R. Muller, D. Cheyins, *ACS Appl. Mater. Interfaces* **2015**, *7*, 618.
- [170] X. Li, F. Xie, S. Zhang, J. Hou, W. C. H. Choy, *Light: Sci. Appl.* **2015**, *4*, e273.
- [171] V. D. Mihailitchi, P. W. M. Blom, J. C. Hummelen, M. T. Rispens, *J. Appl. Phys.* **2003**, *94*, 6849.
- [172] M. T. Greiner, L. Chai, M. G. Helander, W.-M. Tang, Z.-H. Lu, *Adv. Funct. Mater.* **2012**, *22*, 4557.
- [173] C.-M. Chen, Z.-K. Lin, W.-J. Huang, S.-H. Yang, *Nanoscale Res. Lett.* **2016**, *11*, 464.
- [174] M. Vasilopoulou, A. Soultati, D. G. Georgiadou, T. Stergiopoulos, L. C. Palilis, S. Kennou, N. A. Stathopoulos, D. Davazoglou, P. Argitis, *J. Mater. Chem. A* **2014**, *2*, 1738.
- [175] C.-M. Wu, S. Naseem, M.-H. Chou, J.-H. Wang, Y.-Q. Jian, *Front. Mater.* **2019**, *6*, 49.
- [176] B. Bhuyan, B. Paul, S. S. Dhar, S. Vadivel, *Mater. Chem. Phys.* **2017**, *188*, 1.
- [177] M. Usta, S. Kahraman, F. Bayansal, H. A. Cetinkara, *Superlattices Microstruct.* **2012**, *52*, 326.
- [178] G. R. Jafari, A. A. Saberi, R. Azimrad, A. Z. Moshfegh, S. Rouhani, *J. Statist. Mech.: Theory Exp.* **2006**, *2006*, P09017.
- [179] X. Bulliard, S.-G. Ihn, S. Yun, Y. Kim, D. Choi, J.-Y. Choi, M. Kim, M. Sim, J.-H. Park, W. Choi, K. Cho, *Adv. Func. Mater.* **2010**, *20*, 4381.
- [180] S. K. Hau, H.-L. Yip, O. Acton, N. S. Baek, H. Ma, A. K.-Y. Jen, *J. Mater. Chem.* **2008**, *18*, 5113.
- [181] C. C. Mardare, A. W. Hassel, *Phys. Status Solidi A* **2019**, *216*, 1900047.
- [182] Y. Jiang, S. Xiao, B. Xu, C. Zhan, L. Mai, X. Lu, W. You, *ACS Appl. Mater. Interfaces* **2016**, *8*, 11658.
- [183] S. Jin, B. J. Jung, C. K. Song, J. Kwak, *Curr. Appl. Phys.* **2014**, *14*, 1809.
- [184] Q. Wei, J. Liu, W. Feng, J. Sheng, X. Tian, L. He, Q. An, L. Mai, *J. Mater. Chem. A* **2015**, *3*, 8070.
- [185] A. Alsulami, J. Griffin, R. Alqurashi, D. Lidzey, A. Buckley, H. Yi, A. Iraqi, *Materials* **2016**, *9*, 235.
- [186] I. Hancox, L. A. Rochford, D. Clare, M. Walker, J. J. Mudd, P. Sullivan, S. Schumann, C. F. McConville, T. S. Jones, *J. Phys. Chem. C* **2013**, *117*, 49.
- [187] C.-C. Hsu, H. W. Su, C. H. Hou, J. J. Shyue, F. Y. Tsai, *Nanotechnology* **2015**, *26*, 385201.
- [188] K. X. Steirer, E. L. Ratcliff, N. R. Armstrong, N. E. Widjonarko, J. Meyer, A. Kahn, P. F. Ndione, M. T. Lloyd, C. J. Curtis, D. S. Ginley, J. J. Berry, D. C. Olson, *Adv. Energy Mater.* **2011**, *1*, 813.
- [189] J. Jung, D. L. Kim, S. H. Oh, H. J. Kim, *Sol. Energy Mater. Sol. Cells* **2012**, *102*, 103.
- [190] Z. Yi Wang, S. H. Lee, D. H. Kim, J. H. Kim, J. G. Park, *Sol. Energy Mater. Sol. Cells* **2010**, *94*, 1591.
- [191] K. X. Steirer, J. P. Chesin, N. E. Widjonarko, J. J. Berry, A. Miedaner, D. S. Ginley, D. C. Olson, *Org. Electron.* **2010**, *11*, 1414.
- [192] M. D. Irwin, D. Bruce Buchholz, A. W. Hains, R. P. H. Chang, T. J. Marks, *Proc. Natl. Acad. Sci.* **2008**, *105*, 2783.
- [193] A. Garcia, G. C. Welch, E. L. Ratcliff, D. S. Ginley, G. C. Bazan, D. C. Olson, *Adv. Mater.* **2012**, *24*, 5368.
- [194] M. D. Irwin, J. D. Servaites, D. B. Buchholz, B. J. Leever, J. Liu, J. D. Emery, M. Zhang, J.-H. Song, M. F. Durstock, A. J. Freeman, M. J. Bedzyk, M. C. Hersam, R. P. H. Chang, M. A. Ratner, T. J. Marks, *Chem. Mater.* **2011**, *23*, 2218.
- [195] X. Fan, G. Fang, F. Cheng, P. Qin, H. Huang, Y. Li, *J. Phys. D: Appl. Phys.* **2013**, *46*, 305106.
- [196] J. R. Manders, S.-W. Tsang, M. J. Hartel, T.-H. Lai, S. Chen, C. M. Amb, J. R. Reynolds, F. So, *Adv. Funct. Mater.* **2013**, *23*, 2993.
- [197] S. Bai, M. Cao, Y. Jin, X. Dai, X. Liang, Z. Ye, M. Li, J. Cheng, X. Xiao, Y. Jin, Z. Ye, Y. Jin, Z. Wu, Z. Xia, B. Sun, E. Wang, Y. Mo, F. Gao, F. Zhang, *Adv. Energy Mater.* **2014**, *4*, 1301460.
- [198] M.-Y. Lin, C.-Y. Lee, S.-C. Shiu, I.-J. Wang, J.-Y. Sun, W.-H. Wu, Y.-H. Lin, J.-S. Huang, C.-F. Lin, *Org. Electron.* **2010**, *11*, 1828.
- [199] H.-T. Lien, D. P. Wong, N. H. Tsao, C. I. Huang, C. Su, K. H. Chen, L. C. Chen, *ACS Appl. Mater. Interfaces* **2014**, *6*, 22445.
- [200] Q. Xu, F. Wang, Z. Tan, L. Li, S. Li, X. Hou, G. Sun, X. Tu, J. Hou, Y. Li, *ACS Appl. Mater. Interfaces* **2013**, *5*, 10658.
- [201] W. Shen, C. Yang, X. Bao, L. Sun, N. Wang, J. Tang, W. Chen, R. Yang, *Mater. Sci. Eng. B* **2015**, *200*, 1.
- [202] Y.-Y. Yu, W.-C. Chien, Y.-J. Wang, *Thin Solid Films* **2016**, *618*, 134.
- [203] J. Zhang, J. Wang, Y. Fu, B. Zhang, Z. Xie, *RSC Adv.* **2015**, *5*, 28786.
- [204] Z. Yu, W. Liu, W. Fu, Z. Zhang, W. Yang, S. Wang, H. Li, M. Xu, H. Chen, *J. Mater. Chem. A* **2016**, *4*, 5130.
- [205] Y. Guo, H. Lei, L. Xiong, B. Li, Z. Chen, J. Wen, G. Yang, G. Li, G. Fang, *J. Mater. Chem. A* **2017**, *5*, 11055.
- [206] A. Soultati, A. M. Douvas, D. G. Georgiadou, L. C. Palilis, T. Bein, J. M. Feckl, S. Gardelis, M. Fakis, S. Kennou, P. Falaras, T. Stergiopoulos, N. A. Stathopoulos, D. Davazoglou, P. Argitis, M. Vasilopoulou, *Adv. Energy Materials* **2014**, *4*, 1300896.
- [207] Y. Zhao, A. M. Nardes, K. Zhu, *Appl. Phys. Lett.* **2014**, *104*, 213906.
- [208] J. Meyer, S. Hamwi, M. Kröger, W. Kowalsky, T. Riedl, A. Kahn, *Adv. Mater.* **2012**, *24*, 5408.

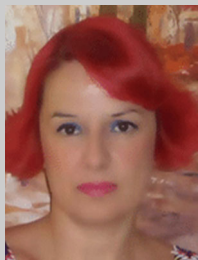
- [209] E. Della Gaspera, Y. Peng, Q. Hou, L. Spiccia, U. Bach, J. J. Jasieniak, Y.-B. Cheng, *Nano Energy* **2015**, 13, 249.
- [210] E. M. Sanehira, B. J. Tremolet De Villers, P. Schulz, M. O. Reese, S. Ferrere, K. Zhu, J. J. Berry, J. M. Luther, E. M. Sanehira, L. Y. Lin, *ACS Energy Lett.* **2016**, 1, 38.
- [211] S. Olthof, K. Meerholz, *Sci. Rep.* **2017**, 7, 40267.
- [212] P. Schulz, J. O. Tiepelt, J. A. Christians, I. Levine, E. Edri, E. M. Sanehira, G. Hodes, D. Cahen, A. Kahn, *ACS Appl. Mater. Interfaces* **2016**, 8, 31491.
- [213] P. Schulz, L. L. Whittaker-Brooks, B. A. MacLeod, D. C. Olson, Y.-L. Loo, A. Kahn, *Adv. Mater. Interfaces* **2015**, 2, 1400532.
- [214] F. Hou, Z. Su, F. Jin, X. Yan, L. Wang, H. Zhao, J. Zhu, B. Chu, W. Li, *Nanoscale* **2015**, 7, 9427.
- [215] P. Liu, X. Liu, L. Lyu, H. Xie, H. Zhang, D. Niu, H. Huang, C. Bi, Z. Xiao, J. Huang, Y. Gao, *Appl. Phys. Lett.* **2015**, 106, 193903.
- [216] L. Chen, B. Zhu, L. Chen, Q. Xie, L. Wan, W. Zhang, S. Fu, H. Zhang, L. Miao, C. Shen, X. Li, W. Zhang, H.-Q. Wang, H.-Q. Wang, X. Ling, J. Yuan, *ACS Appl. Energy Mater.* **2019**, 2, 5862.
- [217] X. Hu, L. Chen, Y. Chen, *J. Phys. Chem. C* **2014**, 118, 9930.
- [218] L. Lin, C. Gu, J. Zhu, Q. Ye, E. Jiang, W. Wang, M. Liao, Z. Yang, Y. Zeng, J. Sheng, W. Guo, B. Yan, P. Gao, J. Ye, Y. Zhu, *J. Mater. Sci.* **2019**, 54, 7789.
- [219] D. Pérez-del-Rey, K. P. S. Zanoni, C. Dreessen, M. Sessolo, P. P. Boix, H. J. Bolink, L. Gil-Escrig, *Chem. Mater.* **2019**, 31, 6945.
- [220] C. G. Granqvist, *Sol. Energy Mater. Sol. Cells* **2000**, 60, 201.
- [221] M. Gillet, K. Aguir, C. Lemire, E. Gillet, K. Schierbaum, *Thin Solid Films* **2004**, 467, 239.
- [222] J. M. Berak, M. J. Sienko, *J. Solid State Chem.* **1970**, 2, 109.
- [223] Y. You, W. Tian, L. Min, F. Cao, K. Deng, L. Li, *Adv. Mater. Interfaces* **2020**, 7, 1901406.
- [224] K. Wang, Y. Shi, Q. Dong, Y. Li, S. Wang, X. Yu, M. Wu, T. Ma, *J. Phys. Chem. Lett.* **2015**, 6, 755.
- [225] S. Masi, R. Mastria, R. Scarfiello, S. Carallo, C. Nobile, S. Gambino, T. Sibillano, C. Giannini, S. Colella, A. Listorti, P. D. Cozzoli, A. Rizzo, *Phys. Chem. Chem. Phys.* **2018**, 20, 11396.
- [226] F. Ali, N. D. Pham, L. Fan, V. Tiong, K. Ostrikov, J. M. Bell, H. Wang, T. Tesfamichael, *ACS Appl. Energy Mater.* **2019**, 2, 5456.
- [227] A. Gheno, T. T. T. Pham, C. Di Bin, J. Bouclé, B. Ratier, S. Vedraïne, *Sol. Energy Mater. Sol. Cells* **2017**, 161, 347.
- [228] H. Yi, D. Wang, L. Duan, F. Haque, C. Xu, Y. Zhang, G. Conibeer, A. Uddin, *Electrochim. Acta* **2019**, 319, 349.
- [229] Z. Li, *Chem. Lett.* **2015**, 44, 1140.
- [230] A. D. Rata, A. R. Chezan, C. N. Presura, T. Hibma, *Surf. Sci.* **2003**, 532–535, 341.
- [231] X. Liu, C. Täschner, A. Leonhardt, M. H. Rummeli, T. Pichler, T. Gemming, B. Büchner, M. Knupfer, *Phys. Rev. B* **2005**, 72, 115407.
- [232] S. Chu, R. Liu, H. Zhou, R. Zhao, Y. Gao, X. Wang, C. Liu, J. Chen, *Semicond. Sci. Technol.* **2018**, 33, 115016.
- [233] X. Yao, J. Qi, W. Xu, X. Jiang, X. Gong, Y. Cao, *ACS Omega* **2018**, 3, 1117.
- [234] L. Xu, M. Qian, Q. Lu, H. Zhang, W. Huang, *Mater. Lett.* **2019**, 236, 16.
- [235] D. Wang, N. K. Elumalai, M. A. Mahmud, M. Wright, M. B. Upama, K. H. Chan, C. Xu, F. Haque, G. Conibeer, A. Uddin, *Org. Electron.* **2018**, 53, 66.
- [236] A. Bagri, C. Mattevi, M. Acik, Y. J. Chabal, M. Chhowalla, V. B. Shenoy, *Nat. Chem.* **2010**, 2, 581.
- [237] L. D'Amario, R. Jiang, U. B. Cappel, E. A. Gibson, G. Boschloo, H. Rensmo, L. Sun, L. Hammarström, H. Tian, *ACS Appl. Mater. Interfaces* **2017**, 9, 33470.
- [238] A. Fakhruddin, M. Seybold, A. Agresti, S. Pescetelli, F. Matteocci, M. I. Haider, S. T. Birkhold, H. Hu, R. Giridharagopal, M. Sultan, I. Mora-Seró, A. Di Carlo, L. Schmidt-Mende, *ACS Appl. Mater. Interface* **2018**, 10, 42542.
- [239] A. G. Marrani, V. Novelli, S. Sheehan, D. P. Dowling, D. Dini, *ACS Appl. Mater. Interfaces* **2014**, 6, 143.
- [240] R. J. O. Mossane, I. Preda, M. Abbate, J. Rubio-Zuazo, G. R. Castro, A. Vollmer, A. Gutiérrez, L. Soriano, *Chem. Phys. Lett.* **2011**, 501, 437.
- [241] Y. Guo, X. Yin, J. Liu, Y. Yang, W. Chen, M. Que, W. Que, B. Gao, *Electrochim. Acta* **2018**, 282, 81.
- [242] F. Ullrich, S. Hillebrandt, S. Hietzschold, V. Rohnacher, T. Marszalek, W. Kowalsky, R. Lovrincic, S. Beck, E. Mankel, A. Pucci, *ACS Appl. Energy Mater.* **2018**, 1, 3113.
- [243] E. L. Ratcliff, J. Meyer, K. X. Steirer, A. Garcia, J. J. Berry, D. S. Ginley, D. C. Olson, A. Kahn, N. R. Armstrong, *Chem. Mater.* **2011**, 23, 4988.
- [244] C. J. Flynn, S. M. McCullough, L. Li, Carrie L. Donley, Y. Kanai, J. F. Cahoon, *J. Phys. Chem. C* **2016**, 120, 16568.
- [245] B. Shan, B. D. Sherman, C. M. Klug, A. Nayak, S. L. Marquard, Q. Liu, R. M. Bullock, T. J. Meyer, *J. Phys. Chem. Lett.* **2017**, 8, 4374.
- [246] Y. Bai, H. Chen, S. Xiao, Q. Xue, T. Zhang, Z. Zhu, Q. Li, C. Hu, Y. Yang, Z. Hu, F. Huang, K. S. Wong, H.-L. Yip, S. Yang, *Adv. Funct. Mater.* **2016**, 26, 2950.
- [247] A. Vilan, D. Cahen, *Chem. Rev.* **2017**, 117, 4624.
- [248] Q. Wang, C.-C. Chueh, T. Zhao, J. Cheng, M. Eslamian, W. C. H. Choy, A. K.-Y. Jen, *ChemSusChem* **2017**, 10, 3794.
- [249] H. Cheng, Y. Li, G. Zhao, K. Zhao, Z.-S. Wang, *ACS Appl. Mater. Interfaces* **2019**, 11, 28960.
- [250] W. Chen, Y. Zhou, L. Wang, Y. Wu, B. Tu, B. Yu, F. Liu, H.-W. Tam, G. Wang, A. B. Djurišić, L. Huang, Z. He, *Adv. Mater.* **2018**, 30, 1800515.
- [251] J. Zhao, R. Tavakoli, M. M. Tavakoli, *Chem. Commun.* **2019**, 55, 9196.
- [252] J. H. Lee, Y. W. Noh, I. S. Jin, S. H. Park, J. W. Jung, *ACS Sustainable Chem. Eng.* **2019**, 7, 15495.
- [253] D. Głowienka, D. Zhang, F. D. Giacomo, M. Najafi, S. Veenstra, J. Szymkowski, Y. Galagan, *Nano Energy* **2020**, 67, 104186.
- [254] H. Tsai, R. Asadpour, J.-C. Blancon, C. C. Stoumpos, O. Durand, J. W. Strzalka, B. Chen, R. Verduzco, P. M. Ajayan, S. Tretiak, J. Even, M. A. Alam, M. G. Kanatzidis, W. Nie, A. D. Mohite, *Science* **2018**, 360, 67.
- [255] M.-W. Lin, K.-C. Wang, J.-H. Wang, M.-H. Li, Y.-L. Lai, T. Ohgashi, N. Kosugi, P. Chen, D.-H. Wei, T.-F. Guo, Y.-J. Hsu, *Adv. Mater. Interfaces* **2016**, 3, 1600135.
- [256] J. C. Yu, J. A. Hong, E. D. Jung, D. B. Kim, S.-M. Baek, S. Lee, S. Cho, S. S. Park, K. J. Choi, M. H. Song, *Sci. Rep.* **2018**, 8, 1070.
- [257] Y. Cheng, M. Li, X. Liu, S. H. Cheung, Chandran Hrisheekesh Thachoth, Li Ho-Wa, Xu Xiuwen, Xie Yue-Min, So Shu Kong, Yip Hin-Lap, Tsang Sai-Wing, *Nano Energy* **2019**, 61, 496.
- [258] D. Di Girolamo, F. Matteocci, F. U. Kosasih, G. Chistiakova, W. Zuo, G. Divitini, L. Korte, C. Ducati, A. Di Carlo, D. Dini, A. Abate, *Adv. Energy Mater.* **2019**, 9, 1901642.
- [259] G. F. Samu, Á. Balog, F. De Angelis, D. Meggiolaro, P. V. Kamat, C. Janáky, *J. Am. Chem. Soc.* **2019**, 141, 10812.
- [260] C. Li, A. Guerrero, Y. Zhong, A. Gräser, C. A. M. Luna, J. Köhler, J. Bisquert, R. Hildner, S. Huettnner, *Small* **2017**, 13, 1701711.
- [261] Y. Zhang, S. Zhang, S. Wu, C. Chen, H. Zhu, Z. Xiong, W. Chen, R. Chen, S. Fang, W. Chen, *Adv. Mater. Interfaces* **2018**, 5, 1800645.
- [262] Q. He, K. Yao, X. Wang, X. Xia, S. Leng, F. Li, *ACS Appl. Mater. Interfaces* **2017**, 9, 41887.
- [263] J. Zhang, W. Mao, X. Hou, J. Duan, J. Zhou, S. Huang, W. Ou-Yang, X. Zhang, Z. Sun, X. Chen, *Sol. Energy* **2018**, 174, 1133.
- [264] Y. Wang, Z. Xia, J. Liang, X. Wang, Y. Liu, C. Liu, S. Zhang, H. Zhou, *Semicond. Sci. Technol.* **2015**, 30, 054004.

- [265] M. I. Hossain, F. H. Alharbi, N. Tabet, *Sol. Energy* **2015**, 120, 370.
- [266] C. Zuo, L. Ding, *Small* **2015**, 11, 5528.
- [267] S. Chatterjee, A. J. Pal, *J. Phys. Chem. C* **2016**, 120, 1428.
- [268] B. A. Nejand, V. Ahmadi, S. Gharibzadeh, H. R. Shahverdi, *ChemSusChem* **2016**, 9, 302.
- [269] L. Liu, Q. Xi, G. Gao, W. Yang, H. Zhou, Y. Zhao, C. Wu, L. Wang, J. Xu, *Solar Energy Mater. Sol. Cells* **2016**, 157, 937.
- [270] W. Sun, Y. Li, S. Ye, H. Rao, W. Yan, H. Peng, Y. Li, Z. Liu, S. Wang, Z. Chen, L. Xiao, Z. Bian, C. Huang, *Nanoscale* **2016**, 8, 10806.
- [271] H. Rao, S. Ye, W. Sun, W. Yan, Y. Li, H. Peng, Z. Liu, Z. Bian, Y. Li, C. Huang, *Nano Energy* **2016**, 27, 51.
- [272] Z.-K. Yu, W.-F. Fu, W.-Q. Liu, Z.-Q. Zhang, Y.-J. Liu, J.-L. Yan, T. Ye, W.-T. Yang, H.-Y. Li, H.-Z. Chen, *Chin. Chem. Lett.* **2017**, 28, 13.
- [273] Y. Guo, H. Lei, L. Xiong, B. Li, G. Fang, *J. Mater. Chem. A* **2018**, 6, 2157.
- [274] P. Sun, Y. Wang, H. Liu, K. Wang, D. Wu, Z. Xu, H. Zhu, *Plos One* **2014**, 9, e111908.
- [275] K. P. Loh, Q. Bao, G. Eda, M. Chhowalla, *Nat. Chem.* **2010**, 2, 1015.
- [276] P. Feicht, S. Eigler, *ChemNanoMat* **2018**, 4, 244.
- [277] J. Sturla, J. Luxa, M. Pumera, Z. Sofer, *Chem. – Eur. J.* **2018**, 24, 5992.
- [278] H. Raza, *Graphene Nanoelectronics. Metrology, Synthesis, Properties and Applications*, Springer, Berlin Heidelberg **2012**.
- [279] D. Chen, H. Feng, J. Li, *Chem. Rev.* **2012**, 112, 6027.
- [280] G. Eda, Y.-Y. Lin, C. Mattevi, H. Yamaguchi, H.-A. Chen, I.-S. Chen, C.-W. Chen, M. Chhowalla, *Adv. Mater.* **2010**, 22, 505.
- [281] Z. Liu, K. Nørgaard, M. H. Overgaard, M. Ceccato, D. M. A. Mackenzie, N. Stenger, S. L.S. Stipp, T. Hassenkam, *Carbon* **2018**, 127, 141.
- [282] S. H. Dave, C. Gong, A. W. Robertson, J. H. Warner, J. C. Grossman, *ACS Nano* **2016**, 10, 7515.
- [283] P. V. Kumar, N. M. Bardhan, S. Tongay, J. Wu, A. M. Belcher, J. C. Grossman, *Nat. Chem.* **2014**, 6, 151.
- [284] W. Gao, L. B. Alemany, L. Ci, P. M. Ajayan, *Nat. Chem.* **2009**, 1, 403.
- [285] H. F. Liang, C. T. G. Smith, C. A. Mills, S. R. P. Silva, *J. Mater. Chem. C* **2015**, 3, 12484.
- [286] K. I. Bolotin, K. J. Sikes, Z. Jiang, M. Klima, G. Fudenberg, J. Hone, P. Kim, H. L. Stormer, *Solid State Commun.* **2008**, 146, 351.
- [287] C. Lee, X. Wei, J. W. Kysar, J. Hone, *Science* **2008**, 321, 385.
- [288] B. R. Lee, J.-W. Kim, D. Kang, D. W. Lee, S.-J. Ko, H. J. Lee, C.-L. Lee, J. Y. Kim, H. S. Shin, M. H. Song, *ACS Nano* **2012**, 6, 2984.
- [289] W. A. de Heer, C. Berger, X. Wu, P. N. First, E. H. Conrad, X. Li, T. Li, M. Sprinkle, J. Hass, M. L. Sadowski, M. Potemski, G. Martinez, *Solid State Commun.* **2007**, 143, 92.
- [290] T. Mahmoudi, Y. Wang, Y.-B. Hahn, *Nano Energy* **2018**, 47, 51.
- [291] T. A. Amollo, G. T. Mola, V. O. Nyamori, *Sol. Energy* **2018**, 171, 83.
- [292] X. Chen, Q. Liu, M. Zhang, H. Ju, J. Zhu, Q. Qiao, M. Wang, S. Yang, *Nanoscale* **2018**, 10, 14840.
- [293] B. Sun, D. Zhou, C. Wang, P. Liu, Y. Hao, D. Han, L. Feng, Y. Zhou, *Org. Electron.* **2017**, 44, 176.
- [294] S. Chen, X. Yu, M. Zhang, J. Cao, Y. Li, L. Ding, G. Shi, *J. Mater. Chem. A* **2015**, 3, 18380.
- [295] X. Cheng, J. Long, R. Wu, L. Huang, L. Tan, L. Chen, Y. Chen, *ACS Omega* **2017**, 2, 2010.
- [296] J. Cheng, H. Zhang, Y. Zhao, J. Mao, C. Li, S. Zhang, K. S. Wong, J. Hou, W. C. H. Choy, *Adv. Funct. Mater.* **2018**, 28, 1706403.
- [297] E. Jokar, Z. Y. Huang, S. Narra, C.-Y. Wang, V. Kattoor, C.-C. Chung, E. W.-G. Diau, *Adv. Energy Mater.* **2018**, 8, 1701640.
- [298] H. Guo, X. Huang, B. Pu, J. Yang, H. Chen, Y. Zhou, J. Yang, Y. Li, Z. Wang, X. Niu, *RSC Adv.* **2017**, 7, 50410.
- [299] H. Luo, Lin Xuanhuai, Hou Xian, Pan Likun, Huang Sumei, Chen Xiaohong, *Nano-Micro Letters* **2017**, 9, 39.
- [300] S. S. Bhosale, E. Jokar, A. Fathi, C.-M. Tsai, C.-Y. Wang, E. Wei-Guang Diau, *Adv. Funct. Mater.* **2018**, 28, 1803200.
- [301] Q.-D. Yang, J. Li, Y. Cheng, H.-W. Li, Z. Guan, B. Yu, S.-W. Tsang, *J. Mater. Chem. A* **2017**, 5, 9852.
- [302] X. Yin, Y. Zhou, J. Han, H. Nan, M. Tai, Y. Gu, J. Li, H. Lin, *J. Mater. Chem. A* **2018**, 6, 20702.
- [303] Y. Peng, N. Yaacobi-Gross, A. Perumal, H. Faber, G. Vourlias, P. Patsalas, D. D. C. Bradley, Z. He, T. Anthopoulos, *Appl. Phys. Lett.* **2015**, 106, 243302.
- [304] S. A. Mohamed, J. Gasiorowski, K. Hingerl, D. R. T. Zahn, M. C. Scharber, S. S. A. Obayya, M. K. El-Mansy, N. S. Sariciftci, D.A.M. Egbe, P. Stadler, *Sol. Energy Mater. Sol. Cells* **2015**, 143, 369.
- [305] N. D. Treat, N. Yaacobi-Gross, H. Faber, A. K. Perumal, D. D. C. Bradley, N. Stingelin, T. D. Anthopoulos, *Appl. Phys. Lett.* **2015**, 107, 013301.
- [306] N. Yaacobi-Gross, N. D. Treat, P. Pattanasattayavong, H. Faber, A. K. Perumal, N. Stingelin, D. D. C. Bradley, P. N. Stavrinou, M. Heeney, T. D. Anthopoulos, *Adv. Energy Mater.* **2015**, 5, 1401529.
- [307] N. Wijeyasinghe, A. Regoutz, F. Eisner, T. Du, L. Tsetseris, Y.-H. Lin, H. Faber, P. Pattanasattayavong, J. Li, F. Yan, M. A. McLachlan, D. J. Payne, M. Heeney, T. D. Anthopoulos, *Adv. Funct. Mater.* **2017**, 27, 1701818.
- [308] N. Wijeyasinghe, F. Eisner, L. Tsetseris, Y.-H. Lin, A. Seikhan, J. Li, F. Yan, O. Solomeshch, N. Tessler, P. Patsalas, T. D. Anthopoulos, *Adv. Funct. Mater.* **2018**, 28, 1802055.
- [309] I. S. Jin, J. H. Lee, Y. W. Noh, S. H. Park, J. W. Jung, *Inorg. Chem. Front.* **2019**, 6, 2158.
- [310] S. J. Kim, K. Choi, B. Lee, Y. Kim, B. H. Hong, *Annu. Rev. Mater. Res.* **2015**, 45, 63.
- [311] Y. L. Huang, Y. J. Zheng, Z. Song, D. Chi, A. T. S. Wee, S. Y. Quek, *Chem. Soc. Rev.* **2018**, 47, 3241.
- [312] C. M. Went, J. Wong, P. R. Jahelka, M. Kelzenberg, S. Biswas, M. S. Hunt, A. Carbone, H. A. Atwater, *Sci. Adv.* **2019**, 5, eaax6061.
- [313] N. Balis, E. Stratakis, E. Kymakis, *Mater. Today* **2016**, 19, 580.
- [314] Y. Kim, B. Heyne, A. Abouserie, C. Pries, C. Ippen, C. Günter, A. Taubert, A. Wedel, *J. Chem. Phys.* **2018**, 148, 193818.
- [315] Y. Lin, B. Adilbekova, Y. Firdaus, E. Yengel, H. Faber, M. Sajjad, X. Zheng, E. Yarali, A. Seikhan, O. M. Bakr, A. El-Labban, U. Schwingenschlögl, V. Tung, I. McCulloch, F. Laquai, T. D. Anthopoulos, *Adv. Mater.* **2019**, 31, 1902965.
- [316] E. Singh, K. S. Kim, G. Y. Yeom, H. S. Nalwa, *ACS Appl. Mater. Interfaces* **2017**, 9, 3223.
- [317] R. Singh, P. K. Singh, B. Bhattacharya, H.-W. Rhee, *Appl. Mater. Today* **2019**, 14, 175.
- [318] J. Chen, N.-G. Park, *J. Phys. Chem. C* **2018**, 122, 14039.
- [319] X. Li, J. Yang, Q. Jiang, W. Chu, D. Zhang, Z. Zhou, J. Xin, *ACS Appl. Mater. Interfaces* **2017**, 9, 41354.
- [320] D. Saranin, P. Gostischev, D. Tatarinov, I. Ermanova, V. Mazov, D. Muratov, A. Tameev, D. Kuznetsov, S. Didenko, A. Di Carlo, *Materials* **2019**, 12, 1406.
- [321] H. Wang, Z. Yu, X. Jiang, J. Li, B. Cai, X. Yang, L. Sun, *Energy Technology* **2017**, 5, 1836.
- [322] W.-D. Hu, C. Dall'Agnese, X.-F. Wang, G. Chen, M.-Z. Li, J.-X. Song, Y.-J. Wei, T. Miyasaka, *J. Photochem. Photobiol. A* **2018**, 357, 36.
- [323] P. Huang, Z. Wang, Y. Liu, K. Zhang, L. Yuan, Y. Zhou, B. Song, Y. Li, *ACS Appl. Mater. Interfaces* **2017**, 9, 25323.
- [324] A. Capasso, F. Matteocci, L. Najafi, M. Prato, J. Buha, L. Cinà, V. Pellegrini, A. Di Carlo, F. Bonaccorso, *Adv. Energy Mater.* **2016**, 6, 1600920.
- [325] S. Uthayaraj, D. G. B. C. Karunarathne, G. R. A. Kumara, M. Thanishaichelvan, S. Rasalingam, R. M. G. Rajapakse, P. Ravirajan, D. Velauthapillai, *Materials* **2019**, 12, 2037.

- [326] W. Y. Chen, L.-L. Deng, S.-M. Dai, X. Wang, C.-B. Tian, X.-X. Zhan, S.-Y. Xie, R.-B. Huang, L.-S. Zheng, *J. Mater. Chem. A* **2015**, 3, 19353.
- [327] N. Arora, M. Ibrahim Dar, A. Hinderhofer, N. Pellet, F. Schreiber, S. M. Zakeeruddin, M. Grätzel, *Science* **2017**, 358, 768.
- [328] Y. G. Kim, K. C. Kwon, Q. Van Le, K. Hong, H. W. Jang, S. Y. Kim, *J. Power Sources* **2016**, 319, 1.
- [329] G. Kakavelakis, I. Paradisanos, B. Paci, A. Generosi, *Adv. Energy Mater.* **2018**, 8, 1702287.
- [330] S. Kohnepoushi, P. Nazari, B. A. Nejand, M. Eskandari, *Nanotechnology* **2018**, 29, 205201.
- [331] U. Dasgupta, S. Chatterjee, A. J. Pal, *Sol. Energy Mater. Sol. Cells* **2017**, 172, 353.
- [332] B. Peng, G. Yu, Y. Zhao, Q. Xu, G. Xing, X. Liu, D. Fu, B. Liu, J. Rong, S. Tan, W. Tang, H. Lu, J. Xie, L. Deng, T. C. Sum, K. P. Loh, *ACS Nano* **2016**, 10, 6383.
- [333] D. Wang, N. K. Elumalai, A. Mahmud, H. Yi, M. B. Upama, R. A. L. Chin, G. Conibeer, C. Xu, F. Haque, L. Duan, A. Uddin, *Synth. Metals* **2018**, 246, 195.
- [334] F. Hermerschmidt, A. Savva, E. Georgiou, S. M. Tuladhar, J. R. Durrant, I. McCulloch, D. D. C. Bradley, C. J. Brabec, J. Nelson, S. A. Choulis, *ACS Appl. Mater. Interfaces* **2017**, 9, 14136.
- [335] M. O. Reese, S. A. Gevorgyan, M. Jørgensen, E. Bundgaard, S. R. Kurtz, D. S. Ginley, D. C. Olson, M. T. Lloyd, P. Morvillo, E. A. Katz, A. Elschner, O. Haillant, T. R. Currier, V. Shrotriya, M. Hermenau, M. Riede, K. R. Kirov, G. Trimmel, F. C. Krebs, *Sol. Energy Mater. Sol. Cells* **2011**, 95, 1253.
- [336] S. Y. Park, B. J. Kim, K. Kim, M. S. Kang, *Adv. Mater.* **2012**, 24, 834.
- [337] J. Liu, S. Shao, G. Fang, B. Meng, Z. Xie, L. Wang, *Adv. Mater.* **2012**, 24, 2774.
- [338] G. B. Murdoch, S. Hinds, E. H. Sargent, S. W. Tsang, L. Mordoukhovski, Z. H. Lu, *Appl. Phys. Lett.* **2009**, 94, 213301.
- [339] H. Pan, L. Zuo, W. Fu, C. Fan, B. Andreasen, X. Jiang, K. Norrman, F. C. Krebs, H. Chen, *Org. Electron.* **2013**, 14, 797.
- [340] C. Girotto, E. Voroshazi, D. Cheyns, P. Heremans, B. P. Rand, *ACS Appl. Mater. Interfaces* **2011**, 3, 3244.
- [341] G. Cao, L. Li, M. Guan, J. Zhao, Y. Li, Y. Zeng, *Appl. Surf. Sci.* **2011**, 257, 9382.
- [342] F. Guillain, L. Li, M. Guan, J. Zhao, Y. Li, Y. Zeng, *Sol. Energy Mater. Sol. Cells* **2014**, 122, 251.
- [343] T. Stubhan, N. Li, N. A. Luechinger, S. C. Halim, G. J. Matt, C. J. Brabec, *Adv. Energy Mater.* **2012**, 2, 1433.
- [344] J. H. Kim, S. B. Kang, J. H. Lee, Y. H. Shin, H. S. Shin, D. G. Kwon, T. Y. Seong, Y. Park, S. I. Na, H. K. Kim, *Org. Electron.* **2013**, 14, 1305.
- [345] S.-Y. Park, H.-R. Kim, Y.-J. Kang, D.-H. Kim, J.-W. Kang, *Sol. Energy Mater. Sol. Cells* **2010**, 94, 2332.
- [346] K. H. Wong, K. Ananthanarayanan, M. D. Heinemann, J. Luther, P. Balaya, *Sol. Energy* **2012**, 86, 3190.
- [347] G. Terán-Escobar, J. Pampel, J. Caicedo, M. Lira-Cantu, *Energy Environ. Sci.* **2013**, 6, 3088.
- [348] J.-M. Yun, J.-S. Yeo, J. Kim, H.-G. Jeong, D.-Y. Kim, Y.-J. Noh, S.-S. Kim, B.-C. Ku, S. In, *Adv. Mater.* **2011**, 23, 4923.
- [349] N. Chaudhary, R. Chaudhary, J. P. Kesari, A. Patra, S. Chand, *J. Mater. Chem. C* **2015**, 3, 11886.
- [350] P. Cheng, X. Zhan, *Chem. Soc. Rev.* **2016**, 45, 2544.
- [351] M. A. Green, S. P. Bremner, *Nat. Mater.* **2017**, 16, 23.
- [352] A. Fakharuddin, R. Jose, T. M. Brown, F. Fabregat-Santiago, J. Bisquert, *Energy Environ. Sci.* **2014**, 7, 3952.
- [353] S. Rafique, S. M. Abdullah, K. Sulaiman, M. Iwamoto, *Renew. Sustainable Energy Rev.* **2018**, 84, 43.
- [354] A. Fakharuddin, F. Di Giacomo, A. L. Palma, F. Matteocci, I. Ahmed, S. Razza, A. D'Epifanio, S. Licoccia, J. Ismail, A. Di Carlo, T. M. Brown, R. Jose, *ACS Nano* **2015**, 9, 8420.
- [355] T. Leijtens, G. E. Eperon, N. K. Noel, S. N. Habisreutinger, A. Petrozza, H. J. Snaith, *Adv. Energy Mater.* **2015**, 5, 1500963.
- [356] D. Wang, M. Wright, N. K. Elumalai, A. Uddin, *Sol. Energy Mater. Sol. Cells* **2016**, 147, 255.
- [357] J. Zhang, H. Luo, W. Xie, X. Lin, X. Hou, J. Zhou, S. Huang, W. Ou-Yang, Z. Sun, X. Chen, *Nanoscale* **2018**, 10, 5617.
- [358] W. Chen, Y. Zhou, G. Chen, Y. Wu, B. Tu, F.-Z. Liu, L. Huang, A. M. C. Ng, A. B. Djurišić, Z. He, *Adv. Energy Mater.* **2019**, 9, 1803872.
- [359] M. Saliba, T. Matsui, K. Domanski, J.-Y. Seo, A. Ummadisingu, S. M. Zakeeruddin, J.-P. Correa-Baena, W. R. Tress, A. Abate, A. Hagfeldt, M. Grätzel, *Science* **2016**, 354, 206.
- [360] Z. Zhou, X. Li, M. Cai, F. Xie, Y. Wu, Z. Lan, X. Yang, Y. Qiang, A. Islam, L. Han, *Adv. Energy Mater.* **2017**, 7, 1700763.
- [361] Y. Wang, S. Wang, X. Chen, Z. Li, J. Wang, T. Li, X. Deng, *J. Mater. Chem. A* **2018**, 6, 4860.
- [362] T. Mahmoudi, Y. Wang, Y.-B. Hahn, *ACS Energy Lett.* **2019**, 4, 235.
- [363] Y. Wang, T. Wu, J. Barbaud, W. Kong, D. Cui, H. Chen, X. Yang, L. Han, *Science* **2019**, 365, 687.
- [364] J. Carrillo, A. Guerrero, S. Rahimnejad, O. Almora, I. Zarazua, E. Mas-Marza, J. Bisquert, G. Garcia-Belmonte, *Adv. Energy Mater.* **2016**, 6, 1502246.
- [365] T. Li, Z. Chen, Y. Wang, J. Tu, X. Deng, Q. Li, Z. Li, *ACS Appl. Mater. Interfaces* **2020**, 12, 3301.
- [366] M. Breedon, P. Spizzirri, M. Taylor, J. D. Plessis, D. McCulloch, J. Zhu, L. Yu, Z. Hu, C. Rix, W. Wlodarski, *Cryst. Growth Des.* **2010**, 10, 430.
- [367] J. A. Raiford, R. A. Belisle, K. A. Bush, R. Prasanna, A. F. Palmstrom, M. D. McGehee, S. F. Bent, *Sustainable Energy Fuels* **2019**, 3, 1517.
- [368] T. H. Chowdhury, M. Akhtaruzzaman, M. E. Kayesh, K. Ryuji, T. Noda, J.-J. Lee, A. Islam, *Sol. Energy* **2018**, 171, 652.
- [369] U. Kim, K. H. Park, J. Lee, Y. Choi, J. Seo, N. K. Oh, S. Jung, C. Yang, H. Park, K. Choi, H. Yang, J. H. Lee, *ChemNanoMat* **2019**, 5, 776.
- [370] X. Hu, L. Chen, L. Tan, Y. Zhang, L. Hu, B. Xie, Y. Chen, *Sci. Rep.* **2015**, 5, 12161.



Azhar Fakharuddin obtained a Ph.D. in Advanced Materials from University Malaysia Pahang where he worked on improving charge collection efficiency in dye-sensitized solar cells. He then joined the University of Konstanz, Germany, as an Alexander von Humboldt research fellow to work on interfaces and processes in perovskite/organic solar cells. He subsequently moved to imec, Belgium, to work on perovskite light-emitting diodes. Now at University of Konstanz, his current research focuses on novel materials and processes for high-efficiency optoelectronic devices, mainly, solar cells and light-emitting diodes and their related device physics.



Maria Vasilopoulou received her degree in Physics from the University of Athens and Ph.D. in Functional Materials for Nanolithography from the Chemical Engineering Department of the National Technical University of Athens. Then she worked as a postdoctoral researcher at the National Center for Scientific Research Demokritos (NCSR), where she developed organic and inorganic materials for organic solar cells and light-emitting diodes. She is currently a senior researcher at the Institute of Nanoscience and Nanotechnology of NCSR. Her research activity focuses on the area of the organic and halide perovskite optoelectronic devices and mainly on organic/organic and organic/inorganic interface characterization.



Mohammad K. Nazeeruddin's received his Ph.D. degree in Inorganic Chemistry from Osmania University Hyderabad, India. Currently, he is a professor of Chemistry at the Swiss Federal Institute of Technology, Lausanne, and his research focuses on perovskite and dye-sensitized solar cells and light-emitting diodes. His group is involved in developing stable perovskite solar cells by compositional and interface engineering. He was appointed as World Class University (WCU) professor at Korea University and Adjunct Professor at King Abdulaziz University, Jeddah.